

AD-A262 857



MASSACHUSETTS INSTITUTE OF TECHNOLOGY  
LINCOLN LABORATORY

SWAT SYSTEM PERFORMANCE PREDICTIONS

R.R. PARENTI  
R.J. SASIELA  
Group 54

DTIC QUALITY INSPECTED

PROJECT REPORT SWP-8  
Revision 1

10 MARCH 1993

Accession For	
NTIS	CRABI <input checked="" type="checkbox"/>
DTIC	TAB <input checked="" type="checkbox"/>
Unannounced	<input type="checkbox"/>
Justification	
By .....	
Distribution /	
Availability Codes	
Dist	Avail and/or Special
A-1	

Approved for public release; distribution is unlimited.

93-07584



10302

LEXINGTON

93412018

MASSACHUSETTS

This report is based on studies performed at Lincoln Laboratory, a center for research operated by Massachusetts Institute of Technology. The work was sponsored by the Air Force Phillips Laboratory under Air Force Contract F19628-90-C-0002.

This report may be reproduced to satisfy needs of U.S. Government agencies.

The ESC Public Affairs Office has reviewed this report, and it is releasable to the National Technical Information Service, where it will be available to the general public, including foreign nationals.

This technical report has been reviewed and is approved for publication.

FOR THE COMMANDER

  
Gary Tutungian  
Administrative Contracting Officer  
Directorate of Contracted Support Management

Not-Lincoln Recipients

PLEASE DO NOT RETURN

Permission is given to destroy this document  
when it is no longer needed.

MASSACHUSETTS INSTITUTE OF TECHNOLOGY  
LINCOLN LABORATORY

SWAT SYSTEM PERFORMANCE PREDICTIONS

R.R. PARENTI  
R.J. SASIELA  
Group 54

DTIC QUALITY INSPECTION

PROJECT REPORT SWP-8  
Revision 1

10 MARCH 1993

Account For	
NBS	X
DTIC	
U	
Jan	
By	
Date	
Approved /	
Dist	Account For
A-1	

Approved for public release; distribution is unlimited.

## ABSTRACT

In the next phase of Lincoln Laboratory's SWAT (Short-Wavelength Adaptive Techniques) program, the performance of a 241-actuator adaptive-optics system will be measured using a variety of synthetic-beacon geometries. As an aid in this experimental investigation, a detailed set of theoretical predictions has also been assembled. The computational tools that have been applied in this study include a numerical approach in which Monte-Carlo ray-trace simulations of accumulated phase error are developed, and an analytical analysis of the expected system behavior.

This report describes the basis of these two computational techniques and compares their estimates of overall system performance. Although their regions of applicability tend to be complementary rather than redundant, good agreement is usually obtained when both sets of results can be derived for the same engagement scenario.

## PREFACE

From 1982 to 1991 Lincoln Laboratory was supported by the Defense Department to develop the technology of uncooperative-target adaptive optics. A principal feature of this program was the development of synthetic beacons as the reference source for the adaptive-optics wavefront sensor. This technique overcame problems associated with point-ahead and target brightness.

In the late 1980's it became clear that synthetic-beacon technology could be of great value to the astronomical community, who routinely deal with dim objects. Moreover the basic concept had been reinvented by the astronomers with, apparently, no input from the US Defense community. The civilian community seemed on the verge of embarking on a major development program duplicating work the US Government had already paid for.

It seemed incumbent therefore on the DoD to provide to the astronomers the wealth of information that had been developed over the past decade. So, in May 1991 the US Air Force released virtually all of the development work and associated documentation. The immediate impact was that Defense workers began to present their material in open publication. We are now moving to republish a number of documents that seem of greatest import. To some extent these documents are dated as far as military work is concerned, but they are likely to be of great value to the astronomers. At a minimum they are of historical and archival significance.

The report that follows is one of many documents we are in the process of releasing. The original report numbered SWP-8 ("SWAT System Performance Predictions," dated 1 January 1990) is now updated. If you possess the original, it should be destroyed in accordance with current document-control procedures. We are providing a copy of this report to the Defense Technical Information Center (DTIC) so that users may request it. There are intended to be no distribution limitations on this document.

## ACKNOWLEDGMENT

The authors wish to thank Susanne LePage, who wrote the ray-trace simulation code referenced in this report and generated all of the numerical performance results for the figures in Section 5.

## TABLE OF CONTENTS

Abstract	<i>iii</i>
Preface	<i>v</i>
Acknowledgment	<i>vii</i>
List of Illustrations	<i>x</i>
List of Tables	<i>xiii</i>
1. INTRODUCTION	<i>1</i>
2. FOCUSED-BEACON CONCEPTS AND THEIR IMPLEMENTATION IN THE SWAT EXPERIMENTAL PROGRAM	 <i>3</i>
2.1 The SWAT Beacon Geometries	<i>3</i>
2.2 Multiple-Beacon Phase Reconstruction	<i>9</i>
3. NUMERICAL EVALUATION OF SWAT PERFORMANCE USING RAY-TRACE TECHNIQUES	 <i>13</i>
3.1 Numerical Code Structure	<i>13</i>
3.2 Introductory System-Performance Observations	<i>22</i>
4. ANALYTIC EVALUATION OF SWAT PERFORMANCE USING MELLIN TRANSFORM TECHNIQUES	 <i>31</i>
4.1 Computational Model	<i>31</i>
4.2 Focal Anisoplanatism	<i>33</i>
4.3 Beacon Position Measurement Error	<i>38</i>
4.4 Correlation Function of the Tilt Component of Focal Anisoplanatism	<i>40</i>
4.5 Stitching Model and Results	<i>41</i>
5. SWAT PERFORMANCE PREDICTIONS	<i>47</i>
5.1 Single-Beacon Performance Estimates	<i>48</i>
5.2 Performance Estimates for Four Beacons	<i>52</i>
5.3 Dual-Altitude Geometries	<i>55</i>
5.4 Performance Comparisons for the Principal Beacon Geometries	<i>59</i>

## TABLE OF CONTENTS (Continued)

6. SUMMARY	65
REFERENCES	67
APPENDIX A: FOCAL ANISOPLANATISM	69
A.1 Theory	69
A.2 Summary	71
APPENDIX B: FOCAL ANISOPLANATIC TILT	73
B.1 Introduction	73
B.2 Theory	73
B.3 Summary	76
APPENDIX C: CORRELATION FUNCTIONS OF TILT AND OF THE TILT AND PISTON COMPONENTS OF FOCAL ANISOPLANATISM	77
C.1 Introduction	77
C.2 Correlation Function for a Centered Point Source	77
C.3 Evaluation of Correlation Coefficients	81
APPENDIX D: FAR-FIELD IMAGE ANALYSIS	89
D.1 Baseline Correction	90
D.2 Peak Irradiance Estimation	92
APPENDIX E: TURBULENCE MODEL PROFILES	95

## LIST OF ILLUSTRATIONS

2-1 "A" Method beacon geometry.	4
2-2 SWAT beacon geometries.	6
2-3 Multiple-beacon compensation experiment.	8
2-4 Treatment of the multiple-beacon sampling problem.	10
3-1 Simulation flowchart for propagation code ELVIRA.	14
3-2 Ray-trace geometry.	18
3-3 Gradient sampling of the high-resolution grid.	19
3-4 Influence functions used in the numerical ray-trace simulation.	21
3-5 Numerical simulation sample output.	23
3-6 Fitting error results as a function of aperture mask diameter.	25
3-7 Comparison of numerical results for focal anisoplanatic error and total system error.	26
3-8 Comparison of far-field Strehl measurement with the extended Maréchal approximation applied to the near-field phase error.	28
3-9 Correlation of Strehl estimate with $r_o$ and $\theta_o$ for 10 turbulence realizations.	29
4-1 Contributions to the phase variance.	32
4-2 Predicted SWAT phase variance as a function of beacon altitude for a single-beacon system with HV-21 turbulence.	36
4-3 Predicted SWAT phase variance over a single section for a system with four synthetic beacons and HV-21 turbulence.	37
4-4 Phase variance of the jitter due to focal anisoplanatism and beacon-position measurement error for the SWAT system with HV-21 turbulence.	39
4-5 Stitching difference between correlated and uncorrelated tilts.	40
4-6 Correlation function for tilt on two apertures versus their separation distance and direction of separation relative to the tilt direction.	41
4-7 Correlation function for perpendicular components of tilt on an aperture versus the aperture separation in a direction 45 degrees to each tilt.	42
4-8 Aperture model for section stitching for a four-beacon system.	43
4-9 Predicted SWAT performance with four synthetic beacons as a function of beacon altitude and zenith angle for the HV-21 model.	46

## LIST OF ILLUSTRATIONS (Continued)

5-1	Single-beacon performance as a function of beacon altitude.	49
5-2	Single-beacon performance as a function of zenith angle for a beacon range of 5 km.	50
5-3	Single-beacon performance as a function of source displacement.	51
5-4	Single-beacon performance as a function of beacon diameter.	53
5-5	Four-beacon performance as a function of beacon altitude.	54
5-6	Performance of a four-beacon system with one beacon displaced from the center of its section.	56
5-7	Analysis of a hybrid-beacon geometry in which the high-spatial-frequency information is derived from a single beacon placed at the specified altitude and tilt correction is subsequently applied to aperture quadrants based on returns from a 90-km source.	57
5-8	Analysis of a hybrid-beacon geometry in which the high-spatial-frequency information is derived from a set of four beacons placed at the specified altitude and tilt correction is subsequently applied to the four aperture quadrants based on returns from a 90-km source.	58
5-9	Comparison of far-field performance for the four major beacon geometries scheduled for test by the SWAT experimental system as a function of the position of the low-altitude beacon array.	60
5-10	Comparison of far-field performance for the four major beacon geometries scheduled for test by the SWAT experimental system as a function of zenith angle.	61
5-11	Far-field performance as a function of zenith angle for a single sodium beacon.	63
B-1	Focal anisoplanatic geometry.	73
C-1	Correlation function for the piston component of focal anisoplanatism.	84
C-2	Correlation function for tilt.	87
C-3	Correlation function of perpendicular components of tilt with the displacement 45 degrees to the tilt.	88
D-1	Typical histogram plot of uncorrected irradiance near null.	91
D-2	Energy distribution functions for diffraction-limited and aberrated beams.	94

## LIST OF TABLES

2-1	Wavefront-Control System Characteristics	7
3-1	Phase Screen Altitudes and Weights for Ray-Trace Simulation	15
3-2	Turbulence Parameters for Simulation Test Ensemble	16
5-1	Baseline Simulation Parameters	47

## 1. INTRODUCTION

The investigation of novel beam-control methods for non-cooperative targets has been a Lincoln Laboratory effort since 1983, when the first phase of the the SWAT (Short-Wavelength Adaptive Techniques) program was initiated by the Laboratory's High-Energy Laser Beam-Control and Propagation Group. The second phase of that program is now underway at the Group's 60-cm adaptive-optics facility operated at the Air Force Maui Optical Station (AMOS) at Maui.<sup>1,2</sup> These experiments have been generating beam-compensation data since August, 1988.

The purpose of the current SWAT experiments is to validate the concept of creating synthetic turbulence probes by exploiting low-altitude Rayleigh backscatter or resonance backscatter from the sodium layer at 90 km. Several beacon methods have been proposed, most of which involve either the placement of beams in the target's point-ahead direction, either focused beams (the so-called "A" method approach) or laterally-sheared collimated beams ("S" method). Lincoln Laboratory has chosen to concentrate on the former approach and to perform parametric studies of effects such as beacon altitude, beacon size, placement geometry, and reconstruction algorithm.

Associated with the SWAT experimental program is an active theoretical effort to simulate and compare the performance of a wide range of synthetic-beacon constructs. These studies have taken several forms but have recently evolved along two principal paths -- Monte-Carlo ray-trace simulations of accumulated phase error and analytical descriptions of expected ensemble behavior. Both methods are suitable for the sampling geometries of immediate interest, and their domains of applicability tend to be complementary. For those beacon scenarios to which both techniques have been applied, the resulting predictions are found to be in excellent agreement.

This document is an interim report presenting the more important aspects of these on-going investigations. A brief overview of the beacon constructs that will be tested by the SWAT system is given in the next section, along with a description of the baseline data-processing approach. In Sections 2 and 3 the essential characteristics of the performance models are outlined; additional information on both analysis methods can be found in the Appendices.

The main body of this report is contained in Section 5, where a series of parametric performance studies are presented. Included are comparisons as a function of source altitude, number of beacons, and beacon extent. To expedite precise correlation with field data, most of the predictions are given in terms of both wavefront-control figure-error and tilt-removed far-field Strehl.

Although all the present results are specific to the SWAT beam-control system, in a subsequent report these analyses will be generalized to include aperture dimensions appropriate for operational high-energy laser systems.

## 2. FOCUSED-BEACON SAMPLING CONCEPTS AND THEIR IMPLEMENTATION IN THE SWAT EXPERIMENTAL PROGRAM

The earliest proposals incorporating synthetic-beacons as a means of sampling atmospheric turbulence suggested the use of a single pulsed laser to place a focused beam at a nominal altitude of 10 km; at this range the Rayleigh backscatter from a 5-joule laser is sufficient to drive a photon-noise-limited wavefront sensor operating at visible wavelengths. It was soon apparent, however, that this simple construct contains several fundamental defects, the most obvious of which is the lack of good tracking information along the point-ahead path. A second concern is the large sampling error that arises when a low-altitude source is used to replace a physical beacon attached to the target. This source of error, referred to as focal anisoplanatism, places a restriction on the aperture size that can be corrected by a single source at a specified altitude. Figure 2-1 illustrates the relevant geometry and shows the two primary sources of anisoplanatic error -- the unsampled atmosphere above the beacon and the incorrectly sampled atmosphere below the beacon.

Working under the assumption that the problems just described are not insurmountable, the adaptive-optics community has developed a number of alternative sampling approaches with a view toward obtaining better tracking information and improving the figure (tilt-removed) compensation for large apertures. The SWAT program incorporates an experimental investigation of both the tracking and figure components, with particular emphasis on the latter.<sup>1</sup> This report deals strictly with the focal anisoplanatic effects associated with single-beacon and multiple-beacon deployment strategies.

### 2.1 THE SWAT BEACON GEOMETRIES

In Section 4.2 it is shown that the error variance associated with focal anisoplanatism for a single artificial source can be expressed by the relationship

$$\sigma_{focal}^2 \propto (D/H)^{5/3} \quad (2-1)$$

where  $D$  is the aperture diameter and  $H$  is the beacon altitude. Although one could, in principle, achieve an arbitrarily small error by making  $H$  sufficiently large, in practice it is likely to be extremely difficult to obtain adequate signal from a Rayleigh beacon above 20 km. An alternative method is to reduce the effective transmitter diameter by increasing the number of synthetic sources, each of which is used to drive an aperture section. The process of combining gradient measurements from several beacons (often referred to as "stitching") has received considerable attention in recent years.

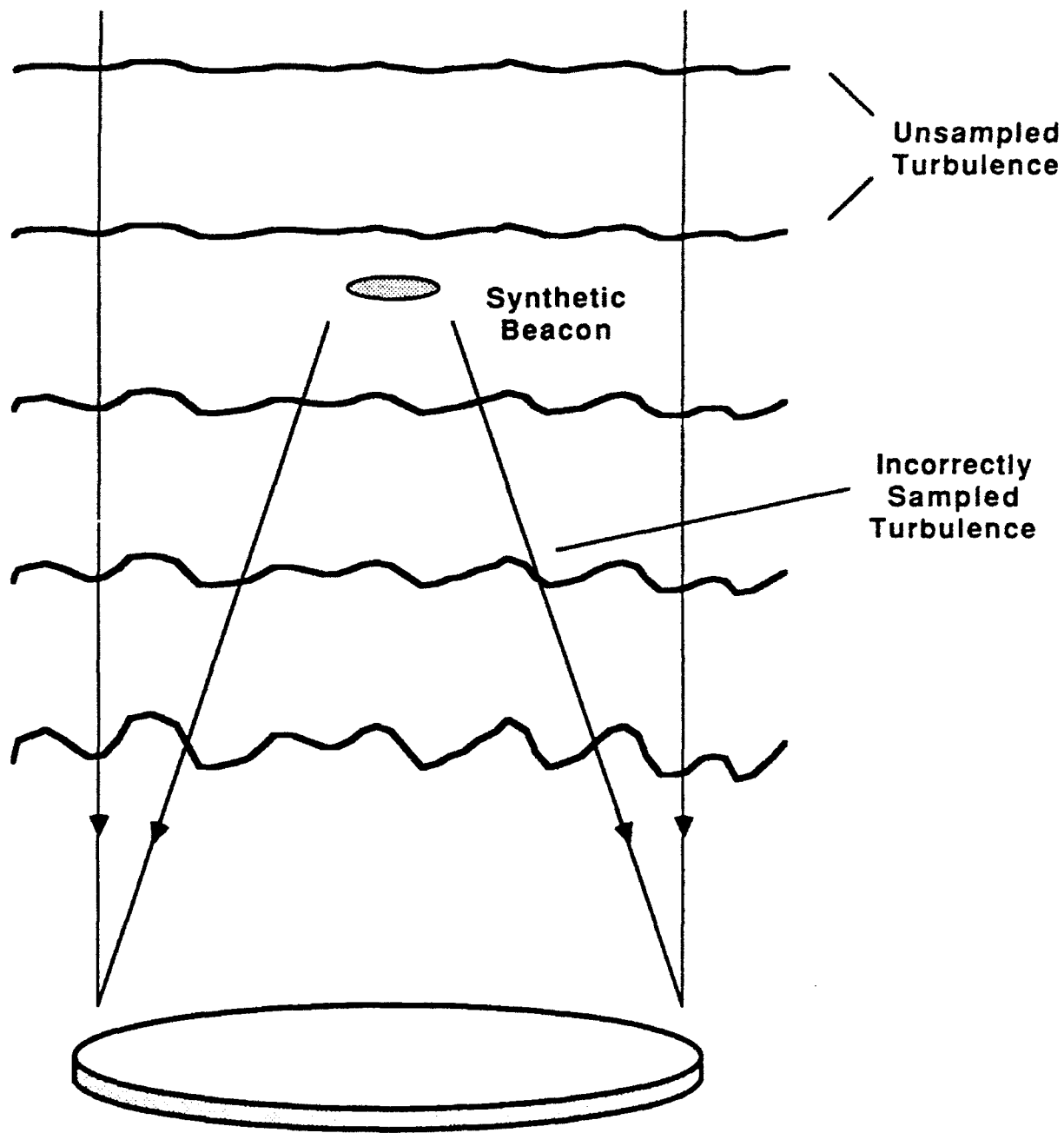


Figure 2-1. "A" method beacon geometry.

The SWAT program represents the community's first attempt to experimentally verify the practical utility of the synthetic-beacon concept and the feasibility of multiple-source stitching as a means of correcting arbitrarily large apertures. The system's 60-cm telescope is small enough to permit a good correction to be made with a single source, yet large enough to show a measurable performance difference between competing multiple-beacon methods. The baseline test sequence will include the following four configurations, each of which is studied in detail later in this report. The associated beacon geometries are depicted in Figure 2-2.

*Single Beacon.* The baseline experiment exploits low-altitude Rayleigh scattering to generate a single artificial source. Using a laser capable of generating a pulse energy of the order of 5 Joules, a beacon having a 1-km depth can be placed at altitudes as high as 10 km. The return radiation is sensed by a gated wavefront sensor that produces gradient data, which is subsequently processed to form a phase-front estimate through the use of conventional Gauss reconstruction techniques.

*Four Beacons.* In order to reduce the effects of focal anisoplanatism, the aperture is divided into four sections that are each driven by a separate source. In the SWAT system, the Rayleigh beacons are placed by sequential pulses so that each subaperture is able to obtain a gradient measurement from each beacon. This arrangement allows the greatest flexibility in data processing.

*Single Beacon — Dual Altitude.* Low spatial-frequency anisoplanatic errors arising from the use of a single low-altitude source can be measured and corrected in a second mirror update by adding a high-altitude source that is measured by large subapertures. By combining gradient outputs to produce four large subapertures in this second iteration, the signal-to-noise improvement makes section-tilt measurements from Rayleigh beacons above 15 km feasible, and resonant returns from the sodium layer at 90 km can also be exploited. In addition to the six dye lasers, the SWAT system may also incorporate a 500-mJ sum-frequency Nd:YAG laser for the purpose of generating resonant sodium returns.<sup>3</sup> Work is also progressing on a 7 J laser sodium laser that would provide single-beacon data from 90 km.

*Four Beacons — Dual Altitude.* In this scenario multiple low-altitude beacons are combined with a single high-altitude source for optimal correction of both low and high spatial-frequency wavefront errors.

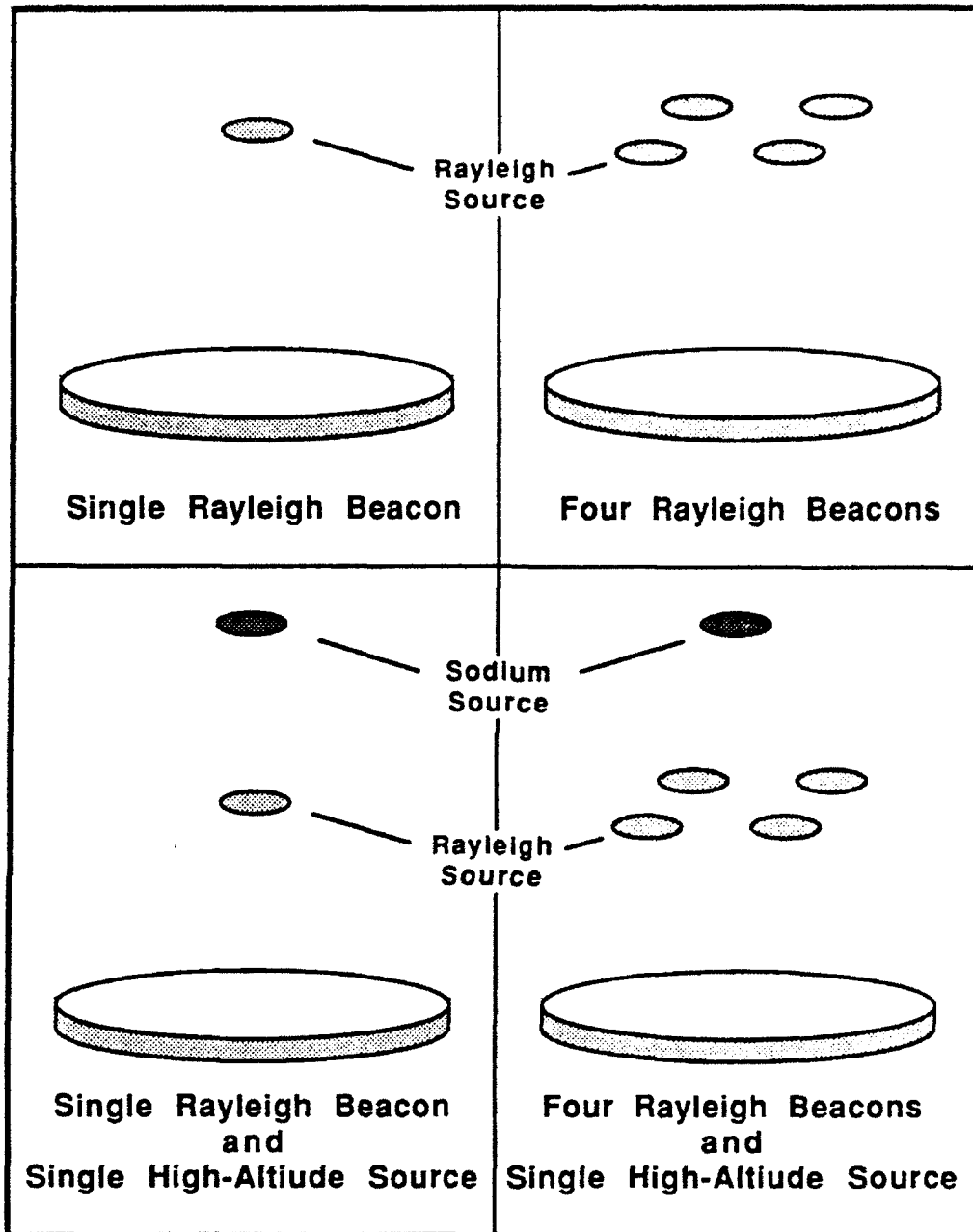


*Figure 2-2. SWAT beacon geometries.*

Parametric investigations of such effects as beacon altitude, radial extent, axial extent, and lateral displacement will also be included in this experimental sequence.

The SWAT system has been designed to test a diverse set of phase sampling and compensation methods and will eventually include a bank of six dye lasers operating at 508 nm and a Nd:YAG laser capable of exciting sodium-resonance backscatter from 90 km. Figure 2-3 shows the major optical elements of this system and illustrates the placement of the fast switching mirrors used to sequentially inject beacons into the outgoing beam path. In the first set of measurements, far-field scoring will be performed by recording star images obtained just before and after the application of a pulsed correction. A summary description of the key wavefront control components is provided in Table 2-1.

**TABLE 2-1**  
**Wavefront-Control System Characteristics**

<p><b>Telescope</b></p> <ul style="list-style-type: none"> <li>• 60-cm Cassegrain</li> <li>• 18-cm central obscuration</li> </ul> <p><b>Wavefront Sensor</b></p> <ul style="list-style-type: none"> <li>• 16x16 modified Hartmann array</li> <li>• 256 x and y gradients/sample</li> <li>• 240-<math>\mu</math>sec readout delay</li> <li>• 100-<math>\mu</math>sec reconstruction delay</li> <li>• <math>\lambda/15</math> performance with 5,000 photons</li> </ul> <p><b>Deformable Mirror</b></p> <ul style="list-style-type: none"> <li>• 17x17 edge-clipped array</li> <li>• 241 active actuators</li> <li>• 3.5-cm actuator spacing</li> <li>• 300-<math>\mu</math>sec response time</li> </ul>	<p><b>Digital Reconstructor</b></p> <ul style="list-style-type: none"> <li>• 241 parallel channels</li> <li>• <math>10^7</math> multiply and add operations/sec</li> </ul> <p><b>Precision Tracking Laser</b></p> <ul style="list-style-type: none"> <li>• 7-watt argon-ion laser</li> <li>• <math>\lambda = 488</math> nm</li> </ul> <p><b>Beacon Lasers (6)</b></p> <ul style="list-style-type: none"> <li>• 5-Joule/pulse dye laser</li> <li>• <math>\lambda = 508</math> nm</li> <li>• Beam quality = <math>20 \lambda/D</math></li> </ul> <p><b>Beacon Laser (1)</b></p> <ul style="list-style-type: none"> <li>• 500-mJ/pulse Nd:YAG sum-frequency laser</li> <li>• <math>\lambda = 589</math> nm</li> </ul>
--	--

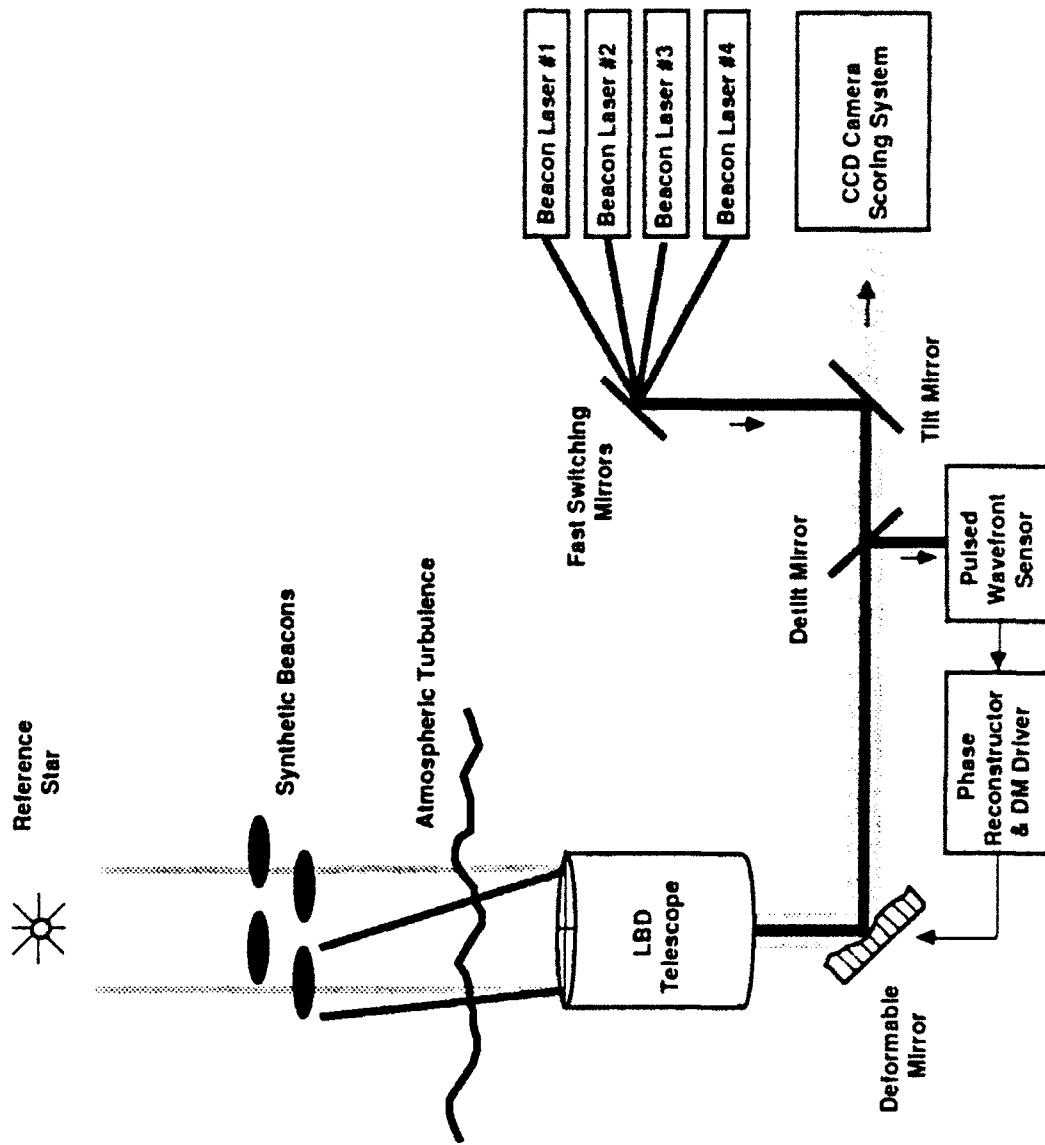


Figure 2-3. Multiple-beacon compensation experiment.

## 2.2 MULTIPLE-BEACON PHASE RECONSTRUCTION

The reconstruction of an optical wavefront from a set of local phase gradient measurements has received extensive treatment in the literature.<sup>4</sup> The standard derivation begins with a model in which the gradient measurements form a grid connecting phase points situated at the nodes of the grid. The matrix representation of this model has the form

$$g = A\varphi \quad , \quad (2-2)$$

where  $g$  is a vector comprising the  $x$  and  $y$ -phase gradients, and  $\varphi$  is the phase vector. The  $A$  matrix describes the physical relationship between pairs of phase points and their connecting gradients. The inverse of Equation (2-2) provides a means of obtaining a best estimate of the phase ensemble from a set of noisy (and therefore inconsistent) measurements of the local phase difference

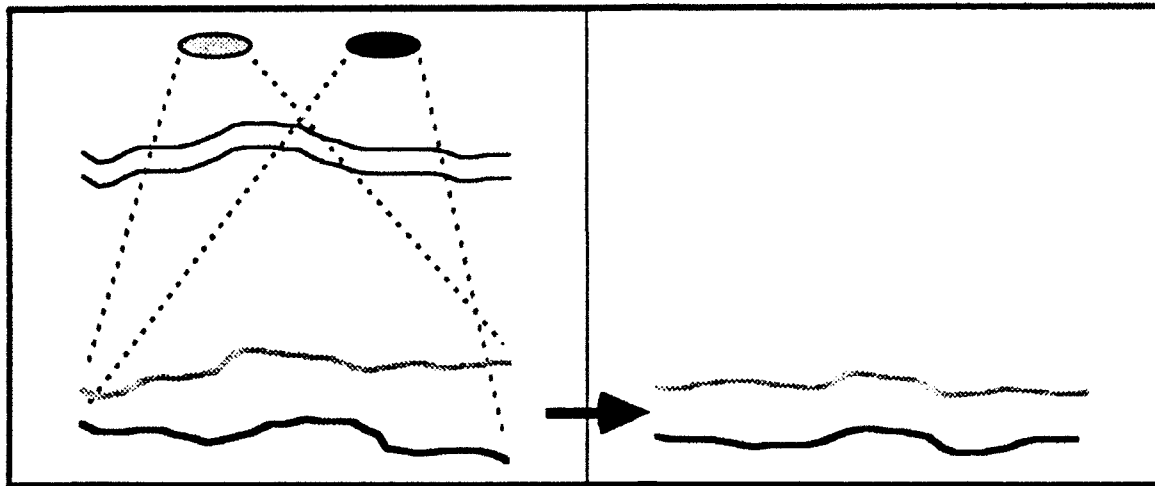
$$\varphi = \{(A^t A)^{-1} A^t\} g = Bg \quad . \quad (2-3)$$

It can be shown that the  $B$  matrix is the optimal estimator if the gradient noise is random and uncorrelated.

There are two major complications to be addressed in dealing with multiple sources; these arise from the manner in which the beacons are projected onto the scattering layer and the variation of the quality of the gradient measurements as a function of aperture position. Both of these complications, and a brief description of the proposed solutions, are illustrated in Figure 2-4.

In order to project an array of sources that are properly positioned over their respective aperture sections, each laser beam must be introduced into the beam train, tilted by the correct angle prior to transmission, and the return beam must be detilted by the same angle before introduction into the wavefront sensor. Due to up-leg anisoplanatic effects, there is no beacon-projection method that will allow the beam positions to be precisely controlled. Furthermore, any mistake made in the process of determining relative source location will contribute to a net "section-stitching" error. The best method of removing this beacon-position sensitivity is to subtract the aperture-average tilt component from each gradient ensemble. The net error associated with this estimation process is quantified in Section 4.3

At this point in the data processing, each subaperture has one gradient sample associated with each synthetic source. In a statistical sense, the quality of these measurements will be related to the inverse of their radial distance from the section centers. These data can be combined through a

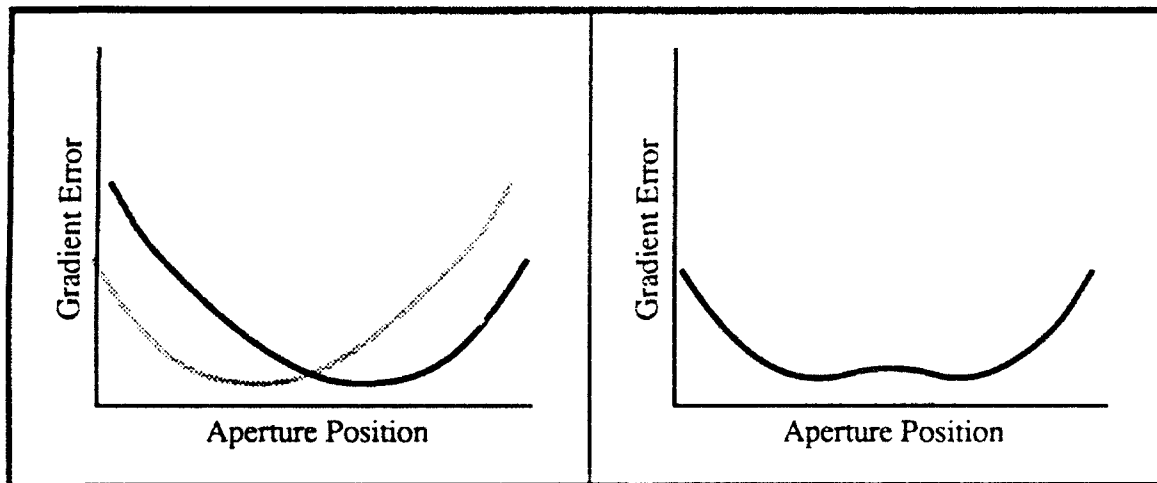


Problem #1

Solution

Differential Tilts are Introduced by Beacon Misposition Errors

Modify the Data to Remove the Full-Aperture Tilt Component



Problem #2

Solution

Duplicate Measurements are Available and Gradient Errors Vary as a Function of Aperture Position

Use Linear Estimation Techniques to Develop a Single Gradient Array with Least-Square Error Characteristics

Figure 2-4. Treatment of the multiple-beacon sampling problem.

linear estimation process defined in the following manner

$$\hat{g} = \mathbf{W}\gamma \quad , \quad (2-4)$$

where  $\hat{g}$  is the best estimate of the gradient array,  $\gamma$  represents the complete set of tilt-corrected gradient measurements, and  $\mathbf{W}$  is the optimal weight matrix. The optimal  $\mathbf{W}$  matrix can be derived from Gauss-Markov estimation theory.<sup>5</sup> The solution for the general case is

$$\mathbf{W} = (\mathbf{U}^T \mathbf{C}_n^{-1} \mathbf{U})^{-1} \mathbf{U}^T \mathbf{C}_n^{-1} \quad , \quad (2-5)$$

where  $\mathbf{C}_n$  is the gradient-noise covariance matrix and  $\mathbf{U}$  is the vector

$$\mathbf{U} = \begin{bmatrix} 1 \\ 1 \\ 1 \\ \vdots \end{bmatrix} \quad .$$

If the covariance matrix is diagonal (i.e. the gradient noise is uncorrelated), the linear weights are found to be inversely proportional to the gradient variances,  $\sigma_i^2$

$$w_i = \frac{(\sigma_i^2)^{-1}}{\sum_i (\sigma_i^2)^{-1}} \quad . \quad (2-6)$$

In the final computational step, a best estimate of the phase matrix,  $\hat{\phi}$ , is obtained from  $\hat{g}$  through the operation described in Equation (2-3).

### 3. NUMERICAL EVALUATION OF SWAT PERFORMANCE USING RAY-TRACE TECHNIQUES

Monte Carlo simulations incorporating ray-trace techniques have frequently been used in the study of turbulence-induced phase distortion processes. Although this method has been criticized as being inelegant, it can accommodate virtually any effect that is relevant to the performance of an adaptive phase-correction system. In addition, estimates of Strehl can be obtained directly from far-field beam profiles derived from the Fourier transform of the near-field phase.

The accuracy of the output generated by a numerical simulation is strongly dependent upon the programmer's ability to properly incorporate all important physical effects, to create a model with sufficient sampling resolution, and to establish a large enough ensemble to provide statistically meaningful results. All these requirements must be weighed against the attendant costs of computational memory and execution time. The programming approach described in this section was structured to satisfy all these constraints.

#### 3.1 NUMERICAL CODE STRUCTURE

##### 3.1.1 Source Construction and Turbulence Profile

The structure of the propagation code ELVIRA used in this study of the SWAT experimental system is outlined in Figure 3-1. The logical flow begins with an atmospheric model represented by a series of 20 phase screens, appropriately weighted and positioned between ground level and 20 km. In order to bracket the expected performance over a reasonably wide range of turbulence conditions, both the HV-21 and SLC-Day models are incorporated in the code; these turbulence profiles are defined in Appendix E, and the associated screen weights and altitudes are listed in Table 3-1.

Each of the screens is represented by a high-resolution phase-distortion array covering a 76 x 76 grid with 0.875-cm spacing. This allows the subapertures, which are assumed to have a 3.5-cm spacing, to be represented by a 4 x 4 subarray. It is the incorporation of this fine structure in the simulation that permits gradient-sampling and influence-function effects to be investigated. Ten turbulence realizations are applied to each sampling scenario; the associated coherence length ( $r_o$ ) and isoplanatic angle ( $\theta_o$ ) parameters are listed in Table 3-2. In all cases the ensemble average is within 5% of the expected value for the specified turbulence profile.

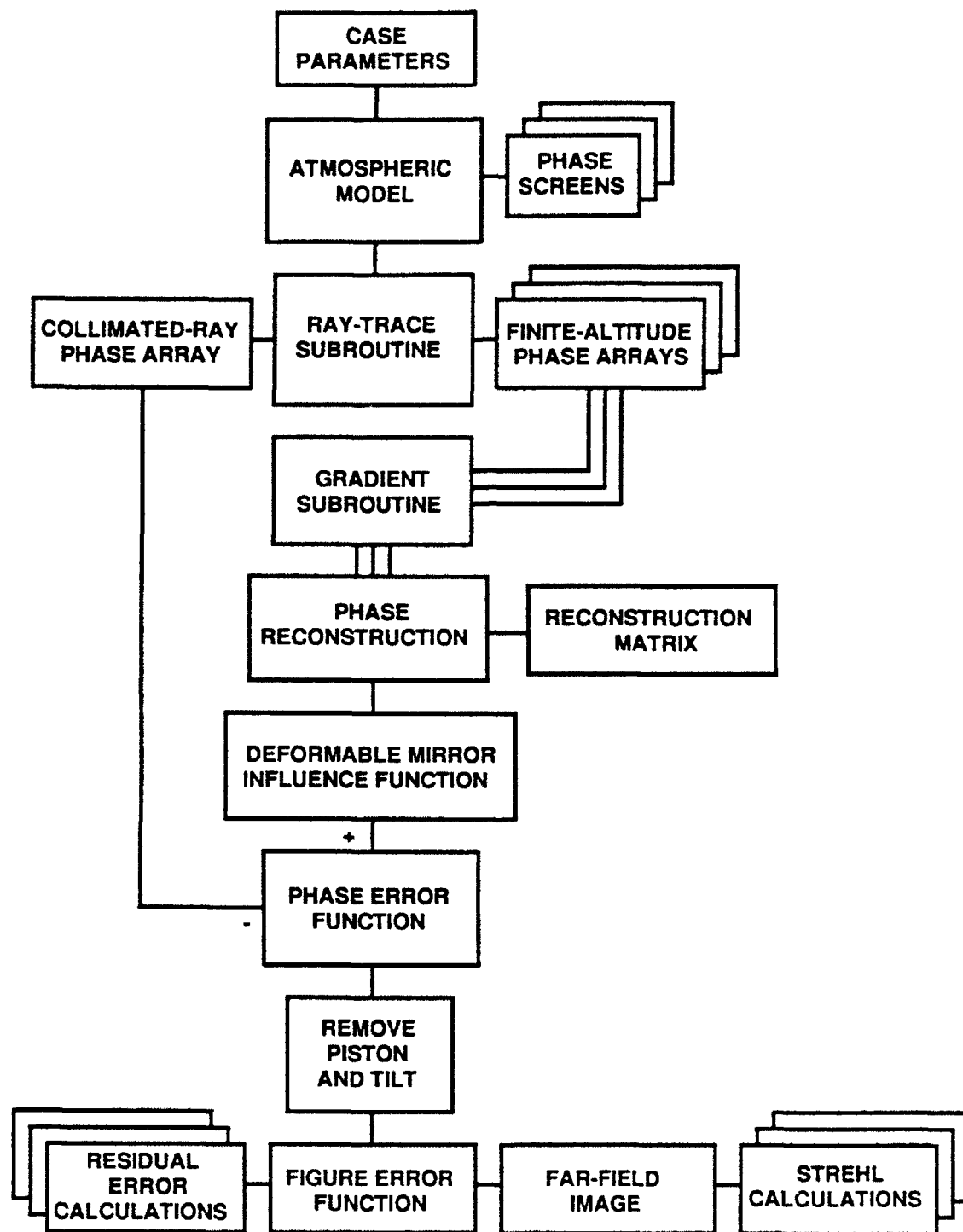


Figure 3-1. Simulation flowchart for propagation code ELVIRA.

**TABLE 3-1**  
**Phase Screen Altitudes and Weights for Ray-Trace Simulation**

Screen Altitude (km)	HV-21 Phase Screen Weights ( $m^{1/3}$ )	SLC-Day Phase Screen Weights ( $m^{1/3}$ )
0.125	$1.623 \times 10^{-12}$	$8.236 \times 10^{-13}$
0.375	$1.807 \times 10^{-13}$	$3.250 \times 10^{-13}$
0.625	$5.506 \times 10^{-14}$	$3.250 \times 10^{-13}$
0.875	$3.857 \times 10^{-14}$	$2.838 \times 10^{-13}$
1.250	$5.902 \times 10^{-14}$	$2.245 \times 10^{-13}$
1.750	$4.224 \times 10^{-14}$	$7.954 \times 10^{-14}$
2.250	$3.027 \times 10^{-14}$	$3.714 \times 10^{-14}$
2.750	$2.171 \times 10^{-14}$	$2.032 \times 10^{-14}$
3.250	$1.563 \times 10^{-14}$	$1.232 \times 10^{-14}$
3.750	$1.137 \times 10^{-14}$	$8.037 \times 10^{-15}$
4.250	$8.485 \times 10^{-15}$	$5.534 \times 10^{-15}$
4.750	$6.648 \times 10^{-15}$	$3.973 \times 10^{-15}$
5.250	$5.629 \times 10^{-15}$	$2.950 \times 10^{-15}$
5.750	$5.240 \times 10^{-15}$	$2.251 \times 10^{-15}$
6.250	$5.317 \times 10^{-15}$	$1.757 \times 10^{-15}$
6.750	$5.712 \times 10^{-15}$	$1.397 \times 10^{-15}$
7.250	$6.288 \times 10^{-15}$	$1.223 \times 10^{-15}$
7.750	$6.926 \times 10^{-15}$	$1.173 \times 10^{-15}$
9.000	$3.235 \times 10^{-14}$	$4.284 \times 10^{-15}$
15.000	$7.647 \times 10^{-14}$	$1.586 \times 10^{-14}$

**TABLE 3-2**  
**Turbulence Parameters for Simulation Test Ensemble**

Run Number	HV-21 Model		SLC-Day Model	
	$r_0$ (cm)	$\theta_0$ ( $\mu$ rad)	$r_0$ (cm)	$\theta_0$ ( $\mu$ rad)
1	4.2	7.8	4.4	12.8
2	6.3	6.5	5.8	12.5
3	4.8	7.0	4.9	12.5
4	4.6	6.2	5.2	12.7
5	4.4	5.2	4.8	10.8
6	5.1	5.2	5.2	11.1
7	4.6	6.6	4.6	12.5
8	4.8	8.8	5.1	14.9
9	6.1	9.4	5.4	15.2
10	5.3	5.3	5.7	11.1
Average	5.0	6.8	5.1	12.6

### 3.1.2 Ray-Trace Procedure

As indicated in Figure 3-2, two sets of ray-trace calculations are performed through the phase-screen ensemble. The reference or "truth" wavefront is generated by summing the array points along collimated ray paths. In a similar fashion, the wavefronts associated with the low-altitude sources are obtained by adding the encountered phase points (with appropriate interpolation) along the slanted rays connecting the source and the measurement point at the collection aperture. Separate high-resolution wavefront fields are produced for each of the synthetic beacons used in a given sampling scenario.

### 3.1.3 Derivation of Phase Gradients

Once all of the phase arrays have been defined in the plane of the receiver aperture, a measurement model can be applied to extract simulated gradient data. The SWAT sensor incorporates a "toe-to-tail" sampling arrangement that requires separate x and y cameras. The spatial relationship between the actuator position and the gradient sampling regions is described in Figure 3-3. Individual subaperture tilts over the enclosed 4 x 4 subarrays are determined by fitting a least-square plane to the included phase points. The gradient output array is formed from those measurements that fall within the 60-cm SWAT aperture.

### 3.1.4 Phase Reconstruction

The general approach for obtaining a best estimate of the wavefront error was presented earlier in Section 2.2. Both the ray-trace and analytical analyses described in this report use a somewhat simplified approach for combining data from multiple synthetic sources, in which the final gradient matrix is constructed from measurements generated by the nearest beacon. Specifically, the reconstructed phase is represented by the matrix operation

$$\varphi = \mathbf{B} \mathbf{S} \mathbf{T} \mathbf{g}' \quad , \quad (3-1)$$

where  $\mathbf{g}'$  is a gradient vector made up of measurements from all available sources,  $\mathbf{T}$  is the matrix that removes overall tilt from each of the sections, and  $\mathbf{S}$  is the operation of selecting the most accurate gradient sample from the available data. (The  $\mathbf{B}$  matrix is the same one used previously for single-source reconstruction.) Direct comparisons of single and multiple-beacon configurations can be performed on the same set of turbulence realizations, and competing stitching algorithms can be readily evaluated. At this point in the analysis, an estimate of the anisoplanatic error associated with the beacon geometry can be made by comparing the collimated phase at the actuator points with the reconstructed phase array.

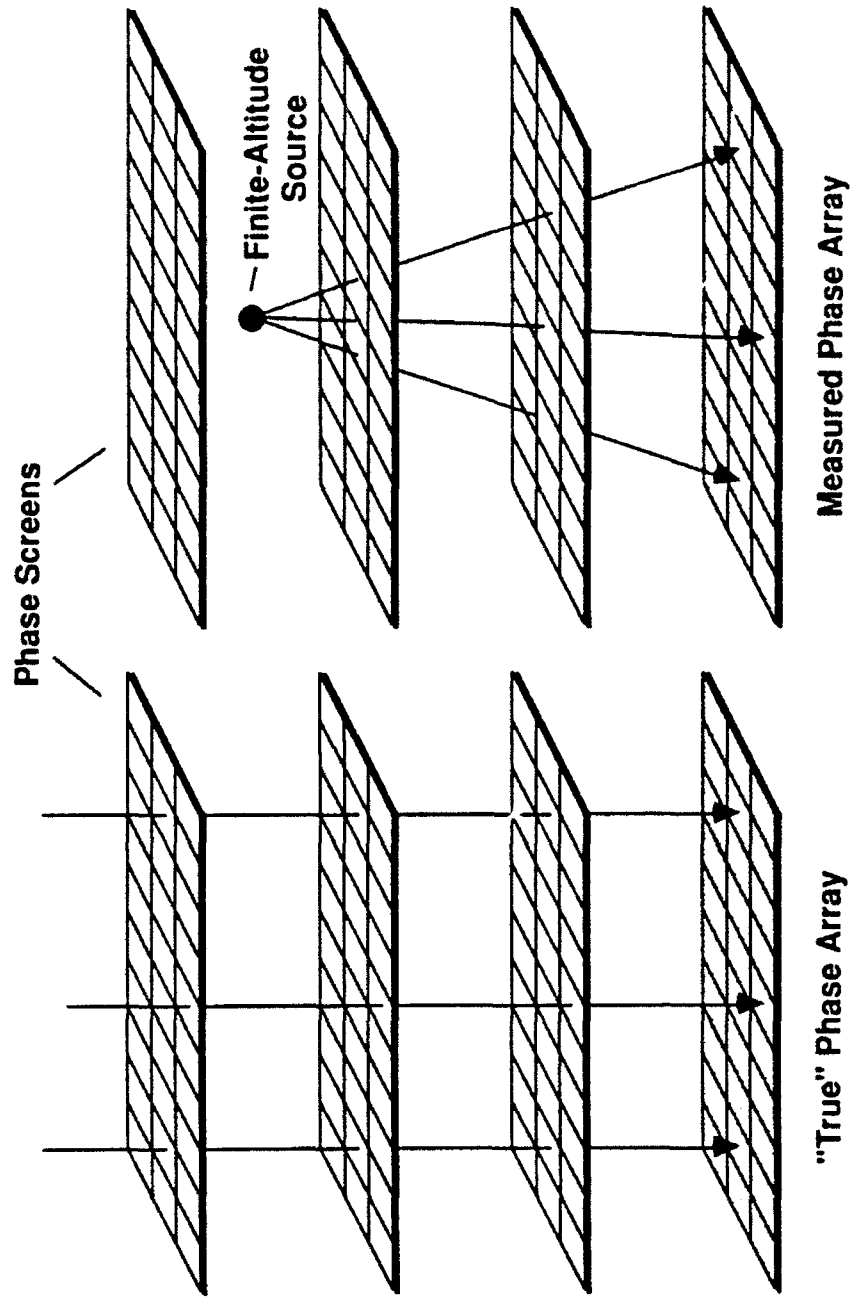
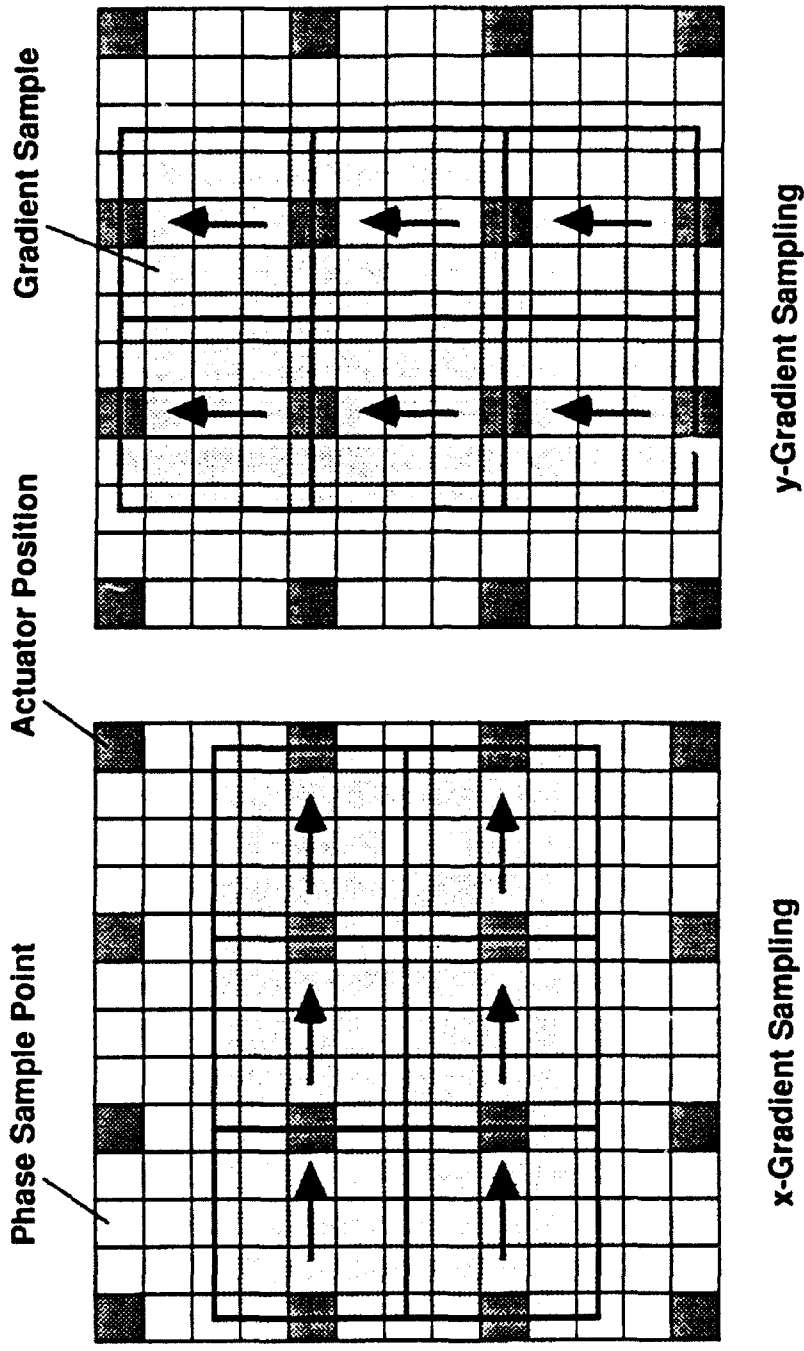


Figure 3-2. Ray-trace geometry.



x-Gradient Sampling

y-Gradient Sampling

Figure 3-3. Gradient sampling of the high-resolution grid.

### 3.1.5 Deformable Mirror Influence Function Effects

The final step in the simulation of phase compensation occurs when an influence function is applied to the actuator-drive positions to create a high-resolution figure over the mirror surface. This process can be represented as a convolution process having the form

$$M(i, j) = F(i, j) \otimes \delta(i - 4n, j - 4m) , \quad (3-2)$$

where  $F(i, j)$  is the mirror influence function, and  $\delta(i - 4n, j - 4m)$  places a delta function at every actuator position. For convenience, the actuators are assumed to be infinitely rigid so that  $F(i, j)$  is zero when  $\{i = 4n, n \neq 0\}$  and  $\{j = 4m, m \neq 0\}$ .

Figure 3-4 illustrates the two influence functions that have been used in this study, each of which has the characteristic of correctly replicating pure tilt and piston. The function labeled "SWAT mirror" has been derived from measurements of the faceplate's response to the motion of a single actuator, but the attendant fitting error differs little from the standard trapezoidal form defined below

$$\begin{aligned} F(i, j) &= \frac{|i-4||j-4|}{16} && : \text{for } |i| < 4 \text{ and } |j| < 4 , \text{ and} \\ &= 0 && : \text{elsewhere} . \end{aligned} \quad (3-3)$$

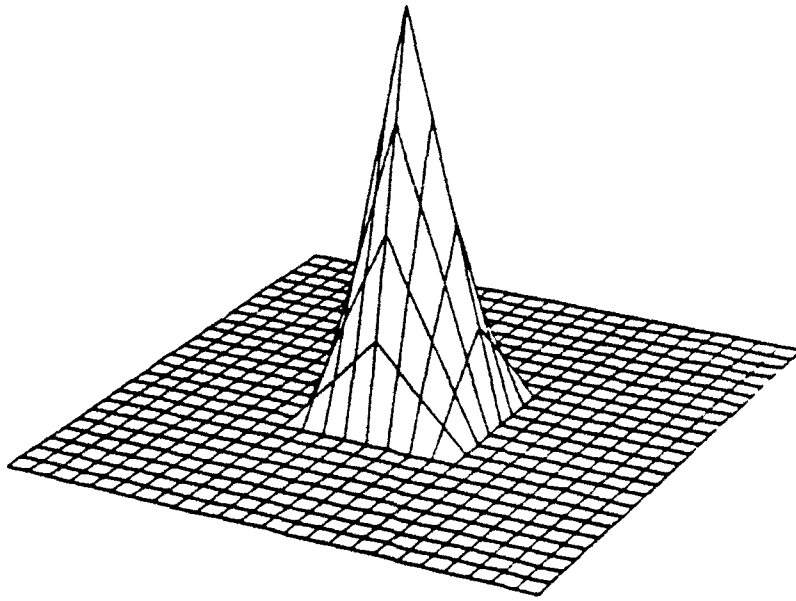
For simplicity, the trapezoidal function has been applied in most of the cases described in this report. The standard simulation also ignores the central obscuration present in the SWAT mirror and derives the phase error function from just the inner 55 cm of the mirror's diameter in order to eliminate anomalous edge effects.

### 3.1.6 Performance Evaluation

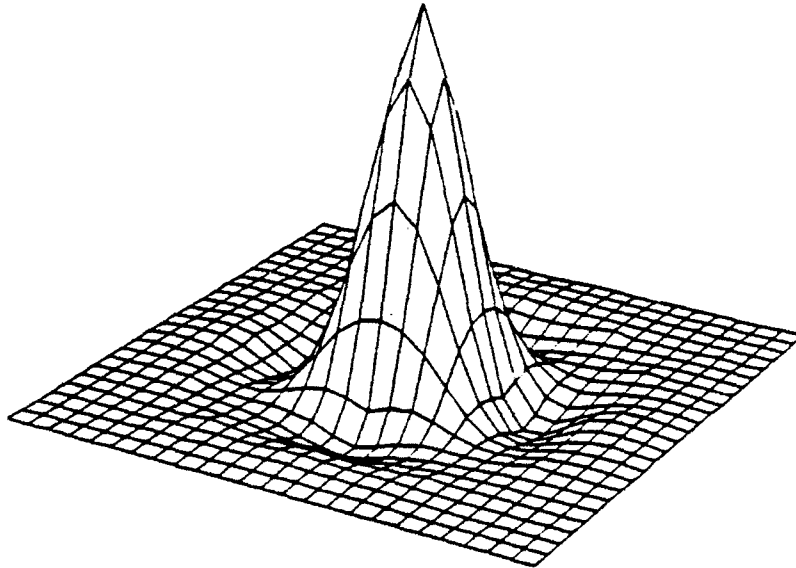
Once the mirror surface figure has been generated in the manner just described, an error function representing the difference between the collimated-source phase and the mirror phase is established. The overall piston term is then removed from this result, and the aperture tilt and figure components are separated by removing overall tilt from the difference function. For figure values smaller than about  $1.5 \text{ rad}^2$ , a reasonably accurate estimate of the tilt-removed Strehl can be obtained from the extended Maréchal approximation

$$\text{Strehl} = \exp(-\sigma^2) . \quad (3-4)$$

Alternatively, the Strehl ratio can be computed directly from the far-field image derived from the Fourier transform of the figure error function. To avoid aliasing errors the code embeds the



Trapezoidal Influence Function



Best Estimate of the SWAT II Mirror Influence Function

*Figure 3-4. Influence functions used in the numerical ray-trace simulation.*

aperture function in a 512 x 512 field of zeros prior to computing the Fourier transform. Figure 3-5 shows an example of a near-field phase error function and its associated far-field image computed in this manner. Obtaining accurate Strehl ratios for highly scintillated beams is a non-trivial exercise; the process incorporated both in this study and the analysis of field data is described in Appendix D. Final performance values are quoted on the basis of average phase variance or average Strehl over the sample ensemble of 10 turbulence realizations.

## 3.2 INTRODUCTORY SYSTEM-PERFORMANCE OBSERVATIONS

A number of general statements can be made regarding the interaction of certain types of system-induced errors and the relationship between tilt-removed error variance and Strehl. These observations appear to be valid for a wide range of data-collection scenarios.

### 3.2.1 Gradient Sampling and Mirror Fitting Effects

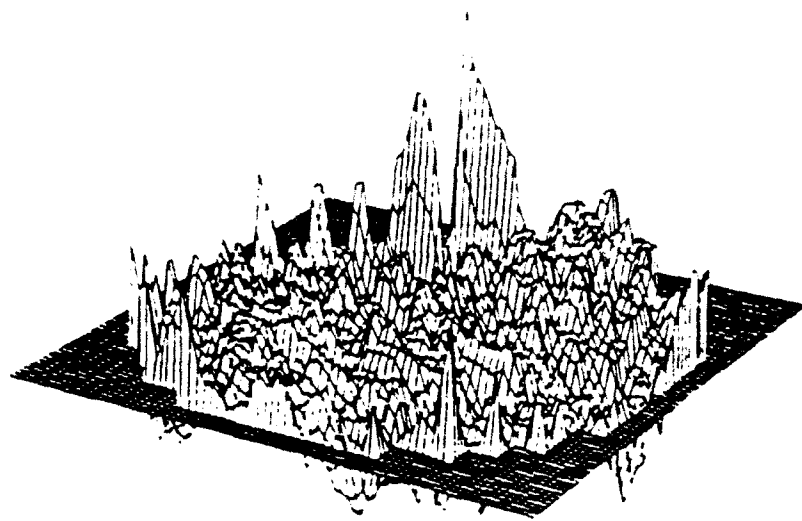
The numerical code has been designed to include a number of important hardware-related effects that are not easily modeled analytically. In particular, the spatial sampling characteristics of the wavefront sensor and the fitting error introduced by the deformable mirror are explicitly included in the model.

Reconstruction techniques that produce phase estimates from gradient data usually include the implicit assumption that each measured gradient is equivalent to a phase difference between adjacent actuator locations. As shown earlier, in Figure 3-3, this assumption is only approximately valid, since each measurement is made over a finite spatial region. By comparing the reference wavefront sampled at actuator grid points with the reconstructed phase values for an ensemble of turbulence realizations, it was determined that the average variance associated with the sampling geometry is  $0.09 \text{ rad}^2$ . This value is small compared to most other sources of error encountered in these simulations and also appears to be highly correlated with other high spatial-frequency effects.

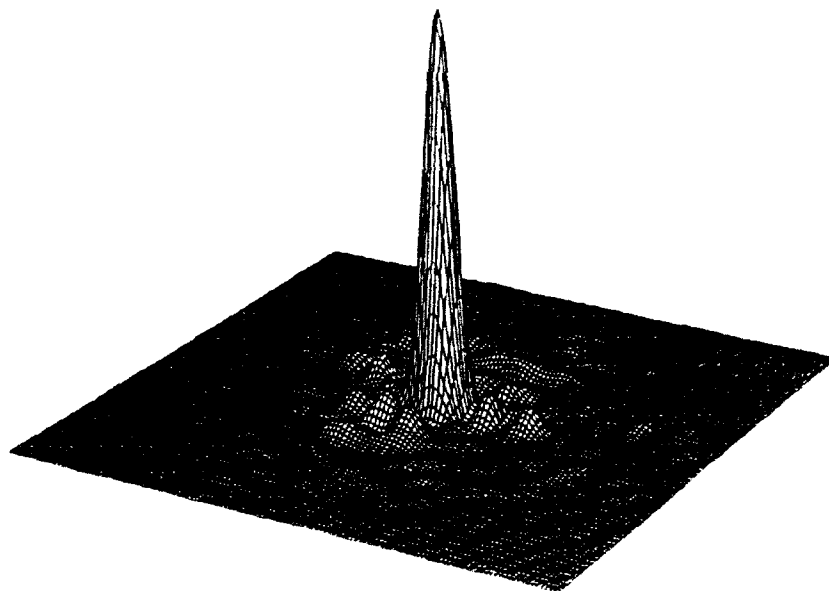
Fitting error refers to a deformable mirror's ability to correctly reproduce the high spatial frequencies associated with Kolmogorov turbulence. For an aperture of infinite extent, the fitting error is predicted to have the approximate form<sup>6</sup>

$$\sigma_{fitting}^2 = 0.32(d_{sub} / r_o)^{5/3} , \quad (3-5)$$

where  $d_{sub}$  is the subaperture diameter. For the nominal SWAT test conditions  $r_o = 5 \text{ cm}$  and  $d_{sub} = 3.5 \text{ cm}$ , which yields a fitting error prediction of  $0.18 \text{ rad}^2$ .



Near-Field Figure Error



Far-Field Strehl

*Figure 3-5. Numerical simulation sample output.*

The SWAT deformable mirror contains a total of 341 active actuators, of which 241 fall within the nominal 60-cm aperture diameter. The remaining actuators form a guard ring that can be held at the average drive voltage as a means of isolating the active section from the face-sheet support structure. Using the HV-21 turbulence model to generate an ensemble of input wavefronts, fitting error effects were measured over concentric mirror regions between 40 and 60 cm. As shown in Figure 3-6, the tilt-removed variances for both the trapezoidal and SWAT influence functions are in accordance with the predicted value out to 55 cm.

### **3.2.2 Comparison of Anisoplanatic Error and Total Near-Field Error Variance**

The validity of error estimates obtained by summing variances from multiple error sources has frequently been questioned in adaptive-optics problems, particularly when the noise mechanism is associated with uncorrected high-spatial-frequency turbulence components. This situation is illustrated in Figure 3-7, which compares the total phase error predicted by the code for a single-beacon geometry at a range of altitudes with the error from focal anisoplanatic effects. At low altitudes, where focal anisoplanatic effects are most significant, the two values are nearly identical. The fitting error component of  $0.2 \text{ rad}^2$  only appears when the anisoplanatic error approaches zero. Over the region of greatest interest, where the error variance is between  $0.5$  and  $1.5 \text{ rad}^2$ , system effects generally add no more than  $0.1 \text{ rad}^2$  ( $\lambda/20$ ) to the anisoplanatic error. This observation will make it easier to relate the analytical results described in the next section to overall system performance

### **3.2.3 Comparison of Error Variance and Far-Field Strehl**

The normal treatment of system performance will present data in terms of error variance. One assumes that this information can be translated in some quantity that relates to the far-field beam, and the extended Maréchal approximation is generally applied to provide this comparison. For the results of interest in this report, the values are most often quoted for tilt-removed calculations, and the applicability of the extended Maréchal approximation for this case is not immediately obvious.

It has been understood for some time that small phase fluctuations in the aperture plane due to poor phase compensation produce a far-field beam with a nearly diffraction-limited central lobe but with a reduced peak intensity. The lost energy is typically due to high spatial frequencies that broadly distribute energy in the far field. As the phase is further corrupted, the beam profile becomes more irregular, making a determination of Strehl much more difficult. Appendix D describes an analysis technique that was developed in the course of studying SWAT data that makes extensive use of histogram transformations to perform background normalization and

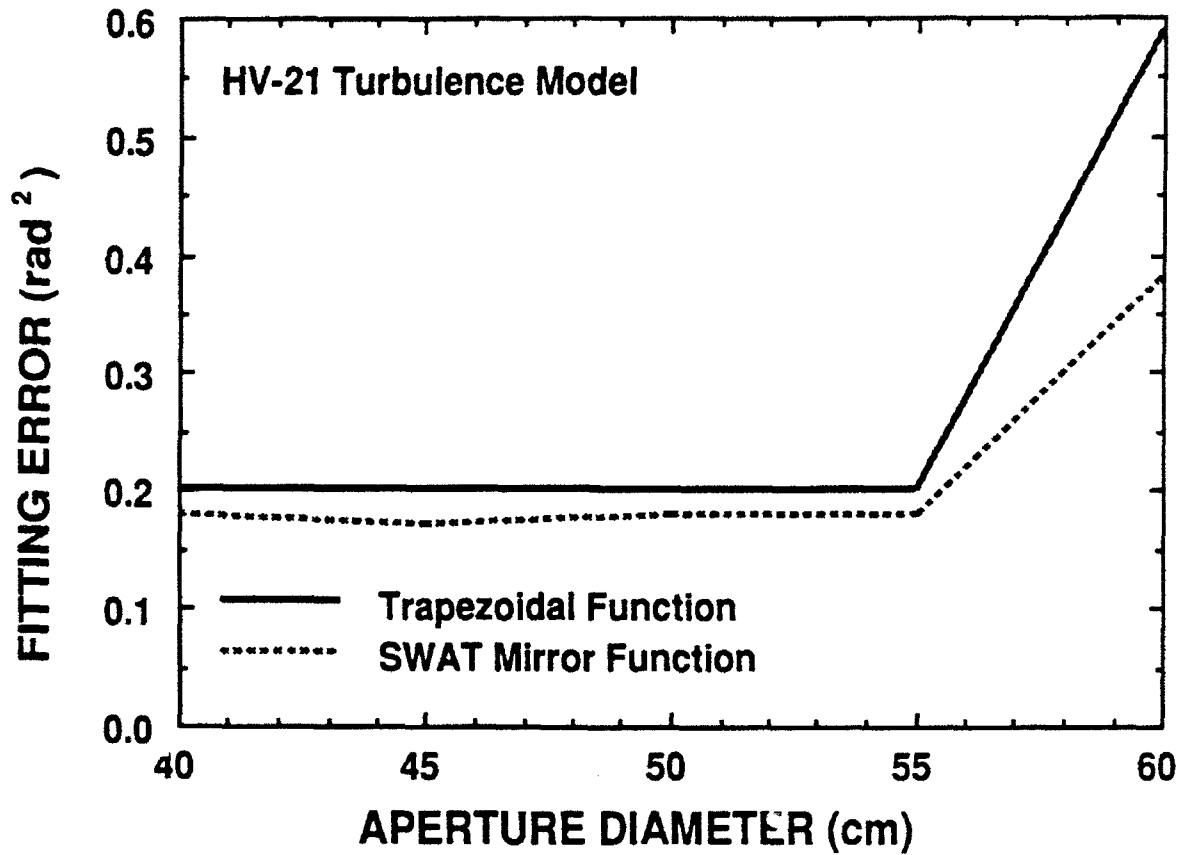


Figure 3-6. Fitting error results as a function of aperture mask diameter. The edge of the 60-cm mask lies just beyond the last ring of active actuators.

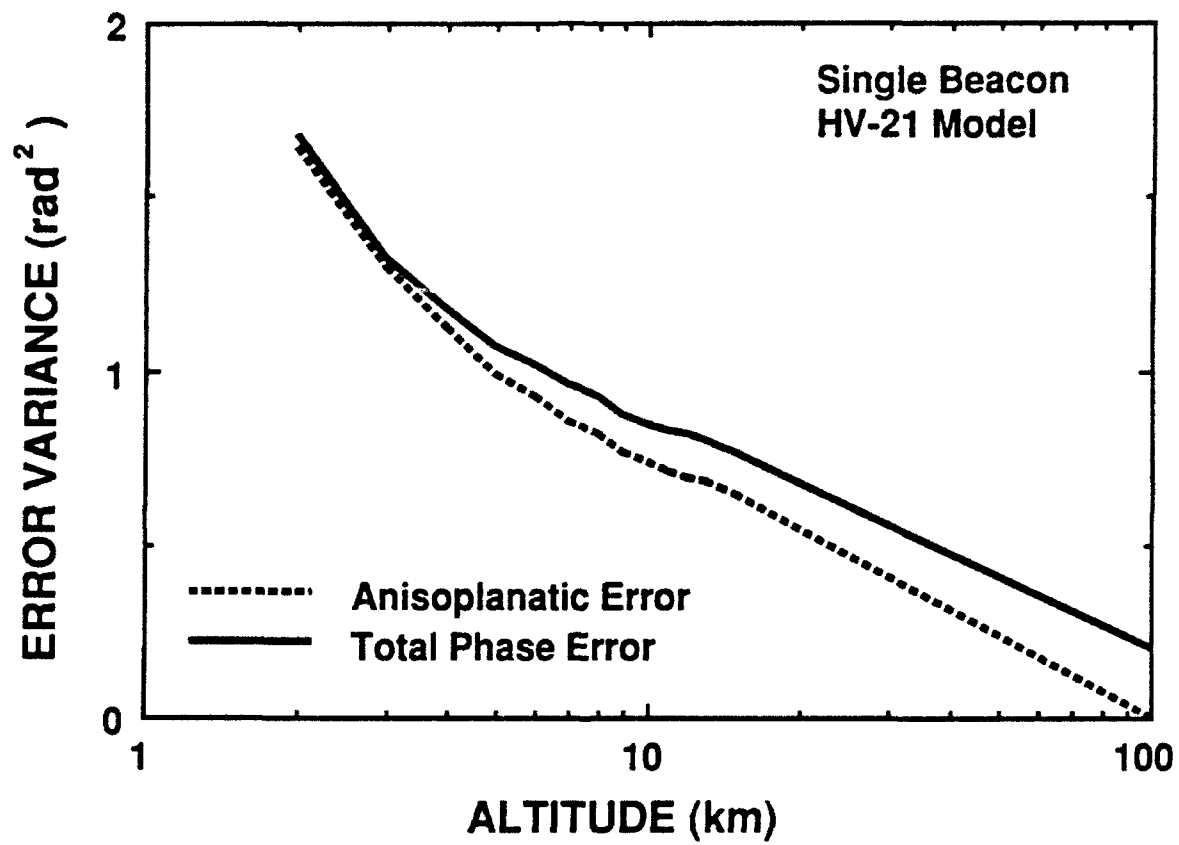


Figure 3-7. Comparison of numerical results for focal anisoplanatic error and total system error.

specify Strehl. To a good approximation, the Strehl value obtained in this manner is the ratio of the peak pixel intensity to the expected peak intensity for a diffraction-limited beam having the same total energy.

ELVIRA uses this same approach in obtaining Strehl from the simulated far-field data. The algorithm removes overall tilt by definition and therefore is appropriate for this study. Figure 3-8 provides a comparison of Strehl with the near-field error variance for two types of noise, the circles relate to focal anisoplanatic error introduced by placing a single beacon at a variety of altitudes; the crosses represent random Gaussian phase error. The extended Maréchal approximation is seen to be valid for both types of data for figure errors less than  $1.5 \text{ rad}^2$  (corresponding to a Strehl of about 0.22). For larger phase distortions the far-field performance will be underestimated by the Maréchal formula, and a better fit to the code output can be obtained from the empirical expression

$$\text{Strehl} = \begin{cases} \exp(-\sigma^2) & : \sigma^2 \leq 1.5 \\ 0.5 \exp(-0.538 \sigma^2) & : \sigma^2 \geq 1.5 \end{cases}, \quad (3-6)$$

which yields reasonable estimates for figure errors as large as  $5 \text{ rad}^2$ .

#### 3.2.4 Correlation of Strehl With $r_o$ and $\theta_o$

Figure errors from focal anisoplanatic effects are not simple functions of low-order turbulence moments but are, instead, expressed as infinite Taylor series of fractional moments (moments calculated from ground level to the beacon altitude). In analyzing future field data, it will be important to understand the pulse-to-pulse performance variation that is to be expected for a given atmospheric model and to establish the correlation (if any) between compensation performance and measurable turbulence parameters.

Figure 3-9 plots Strehl as a function of  $r_o$  and  $\theta_o$  for ten HV-21 and SLC-Day profile realizations using a 5-km single-beacon geometry. Both sets of realizations show a scatter of about a factor of 2 in the estimated correct Strehl and yield correlations that are model specific and relatively weak. (When the two turbulence profiles ensembles were separately processed, a correlation coefficient of about 0.5 was obtained for each parameter.) Note that the expected  $\theta_o$  means of 7 and  $12 \mu\text{rad}$  were obtained for the HV-21 and SLC-Day models respectively, but that each produced the same average Strehl.

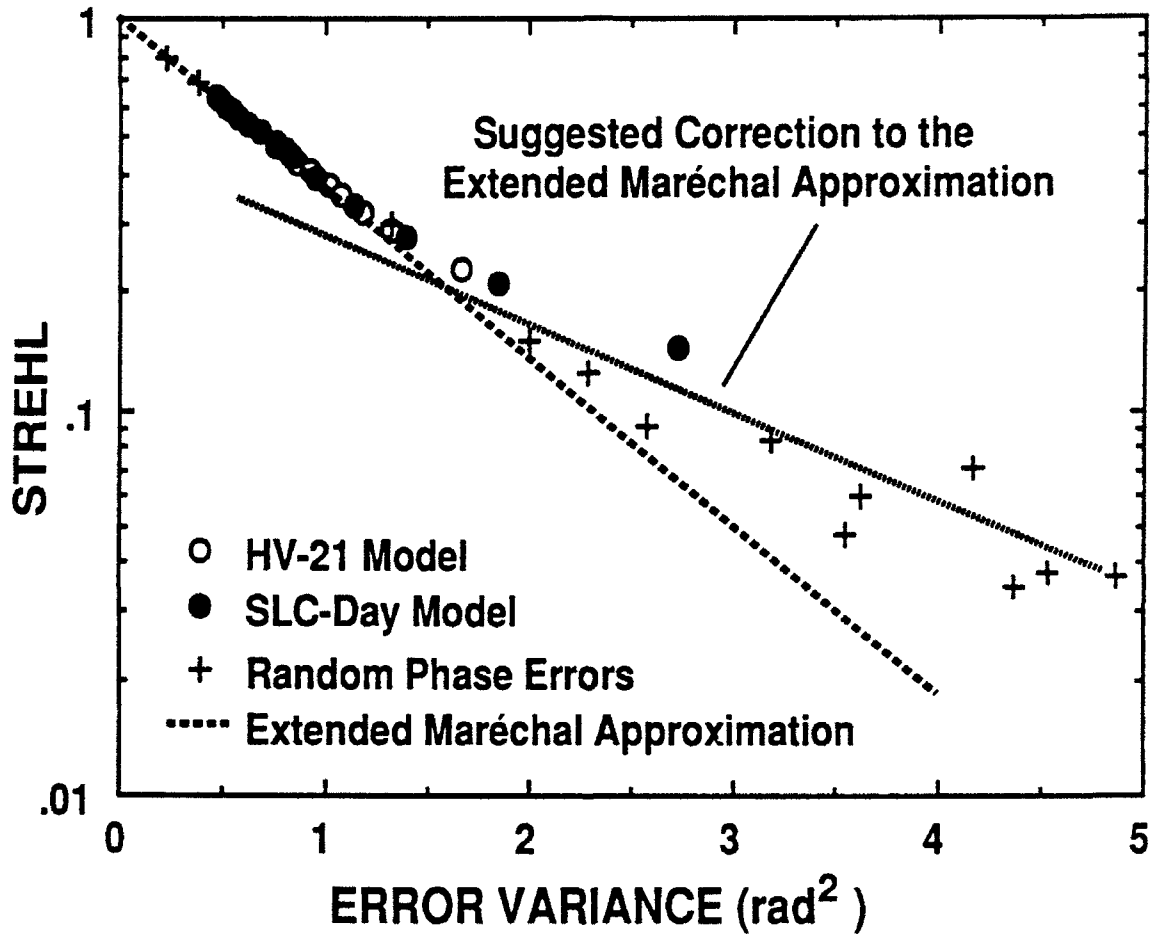


Figure 3-8. Comparison of far-field Strehl measurement with the extended Maréchal approximation applied to the near-field phase error. The circles indicate a range of source placement scenarios that introduce focal anisoplanatic error, and the crosses relate to calculations in which random phase errors have been imposed.

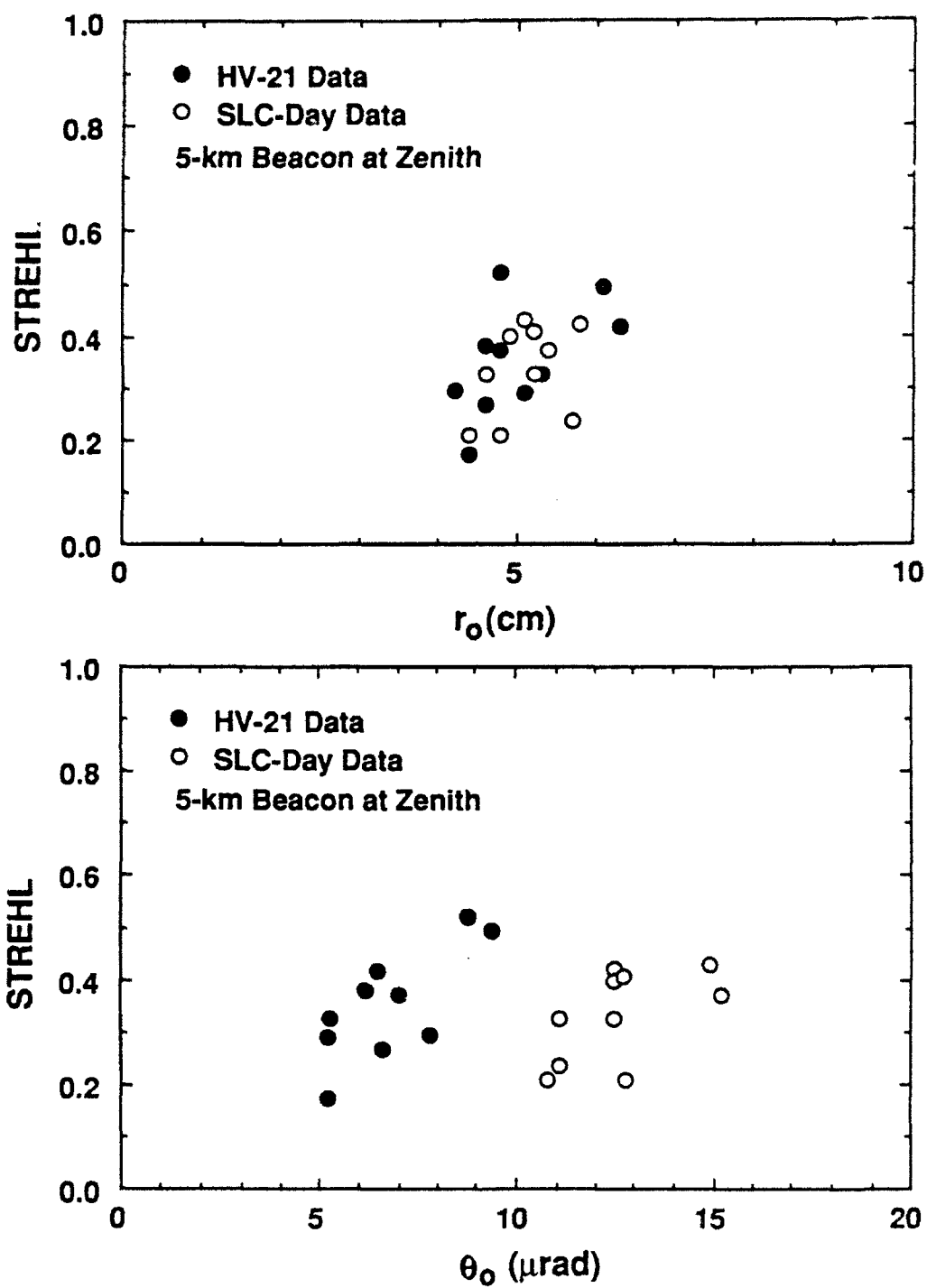


Figure 3-9. Correlation of Strehl estimate with  $r_0$  and  $\theta_0$  values for 10 turbulence realizations.

This simulation shows that overall performance is not well correlated with either  $r_o$  or  $\theta_o$ , and that neither of these parameters is likely to be a good predictor of the achievable far-field Strehl for an individual synthetic-beacon experiment. This is not to imply that these quantities are unimportant in the subsequent data analysis, but rather that the error sources associated with finite-altitude beacon arrays are too complex to be characterized by a single turbulence moment. Methods for obtaining adequate turbulence-profile information are actively sought, but in the interim the performance curves given in this report are likely to serve as the most reliable guide for the SWAT experiments.

## 4. ANALYTIC EVALUATION OF SWAT PERFORMANCE USING MELLIN TRANSFORM TECHNIQUES

In Section 3 of this report, a method was described that has been used to evaluate the performance of the SWAT system through the application of conventional ray-trace techniques. The analysis of much larger systems can present severe computational difficulties, however, and for this reason useful scaling laws for aperture diameter effects are not easily derived in this manner.

In this section a different and more general approach to the system-analysis problem is presented. This method is computationally efficient and, for small systems, has provided results that are close to those obtained with the ray-trace code. The technique can be extended to larger systems with no difficulty, and because the technique breaks the problem down into various components one can readily identify the major sources of system degradation.

### 4.1 COMPUTATIONAL MODEL

The model used to calculate the phase variance assumes the variance is composed of two major parts, as shown in Figure 4-1. The first part is the focal anisoplanatic error, which of itself has the phase variance from the unsensed turbulence above the beacons plus the error made in sensing the turbulence below the beacons. If there were only one beacon, the sum of these two errors with piston and tilt removed would give the total figure variance. For the case of more than one beacon there is a tilt error made in measuring the turbulence below the beacons; this error can be different for each section. In the stitching operation of putting together the phases of each section these tilt errors combine to increase the total error. The tilt error is composed of two parts: the first is from the tilt difference between the collimated beam and the focused beacon beam; the second is from the misplacement of the beacons above the center of each section. It will be assumed that the relative beacon positions are measured with the full aperture of the receiver. Because the ray paths through the atmosphere are different for the various beacons there will be a measurement error associated with the evaluation of the relative beacon positions. To obtain the composite phase profile, the tilt jitters for all sections are stitched together. The correlation of the tilts affects the phase variance averaged over the entire aperture when the full-aperture tilt is removed.

Zernike components other than tilt are also correlated between sections. This correlation is neglected with little resultant error, since these terms represent less than 15% of the total variance and fall off faster than tilt as a function of separation.

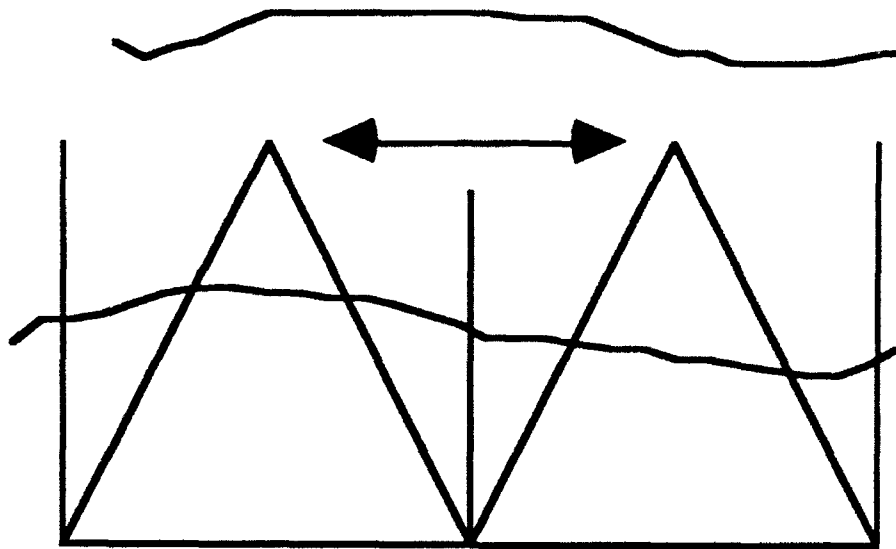


*Figure 4-1. Contributions to the phase variance.*

Each of the components mentioned above will be evaluated separately by using Mellin transform techniques combined with the use of the appropriate filter functions. Analytic expressions will first be found for the components of the focal anisoplanatism with piston and tilt removed above and below the beacon altitude. The tilt component below the beacon will also be found and used in the stitching analysis. It will be assumed in this analysis that the sections are circular in shape in order to get analytic expressions for the results. In actuality the butted sections are square. The error resulting from this assumption should be small.

To stitch the individual sections together a least-squares estimation procedure is used. This approach is similar to that of stitching together the tilt errors measured in a wavefront sensor in an adaptive-optics system to obtain the phase profile.<sup>4</sup> The difference in this case is that the tilt errors can be correlated; this modifies the formula for the error propagator. Because the correlation of the tilts can greatly affect the answer it is necessary to derive expressions for the correlation coefficients of the focal anisoplanatic tilts. From these correlation coefficients the error propagator for stitching of the tilts is found. The error propagator multiplied by the tilt phase variance is the

stitching component of the phase variance. It is added to the tilt-removed phase variance of a single section to obtain the total phase variance.

Finally, the phase variance from focal anisoplanatism and stitching are added together to get the total phase variance. This computation is performed for various altitudes.

## 4.2 FOCAL ANISOPLANATISM

In a previous report (TR-807)<sup>7</sup> a technique was developed in which the phase variance could be written down by inserting a filter function appropriate to a given problem into a general expression for the phase variance. Assuming that inner and outer scale effects of turbulence are negligible, the expression for the phase variance from TR-807 is

$$\sigma^2 = 0.2073 k_0^2 \int_0^L dz C_n^2(z) \int d\bar{\kappa} \kappa^{-11/3} F(\bar{\kappa}, z), \quad (4-1)$$

where  $C_n^2(z)$  is the turbulence strength,  $k_0 = 2\pi/\lambda$ ,  $\lambda$  is the wavelength of the propagating beam, and  $L$  is the range to the beacon. The filter function for the total focal anisoplanatism below the beacon is given in Equation (3.4.49) of TR-807 as

$$F(\bar{\kappa}, z) = 2 \left[ 1 - \frac{2J_1\left(\frac{\kappa D_s z}{2L}\right)}{\frac{\kappa D_s z}{2L}} \right], \quad (4-2)$$

where  $D_s$  is the section diameter.

The filter function for the tilt is the square of the difference between the complex, tilt filter functions of a collimated and focused beam, which is

$$F(\bar{\kappa}, z) = \left[ \frac{4J_2(\kappa D_s / 2)}{\kappa D_s / 2} - \frac{4J_2(\kappa D_s (1 - z/L) / 2)}{\kappa D_s (1 - z/L) / 2} \right]^2. \quad (4-3)$$

In Appendix A the variance due to these components is found. If the beacon is below the top of the turbulence, the partial moment of the turbulence must be used instead of the full moment. The full moment is defined as

$$\mu_n = \sec^{n+1}(\xi) \int_0^\infty dz C_n^2(z) z^n. \quad (4-4)$$

Notice that the zenith angle dependence is contained in the turbulence moment; many authors do not include the zenith dependence in this definition. The upper moment is defined as

$$\mu_n^h(L) = \sec^{n+1}(\xi) \int_H^\infty dz C_n^2(z) z^n, \quad (4-5)$$

where  $H = L/\sec(\xi)$  is the beacon altitude. The lower moment is defined as

$$\mu_n^l(L) = \sec^{n+1}(\xi) \int_0^H dz C_n^2(z) z^n. \quad (4-6)$$

The effect of zenith angle is also incorporated into the partial turbulence moments.

One finds that the total phase variance due to the turbulence below the beacon is

$$\sigma_t^2 = 0.5 k_0^2 \mu_{5/3}^l \left( \frac{D_s}{H} \right)^{5/3}. \quad (4-7)$$

The variance due to tilt is

$$\sigma_t^2 = D_s^{5/3} k_0^2 \left[ 0.355 \frac{\mu_2^l(L)}{L^2} - 0.484 \frac{\mu_3^l(L)}{L^3} + 1.00 \frac{\mu_4^l(L)}{L^4} - 0.543 \frac{\mu_5^l(L)}{L^5} + 0.116 \frac{\mu_6^l(L)}{L^6} \right]. \quad (4-8)$$

The piston variance is

$$\sigma_p^2 = D_s^{5/3} k_0^2 \left[ 0.0835 \frac{\mu_2^l(L)}{L^2} + 0.01378 \frac{\mu_3^l(L)}{L^3} + 0.00697 \frac{\mu_4^l(L)}{L^4} - 0.0591 \frac{\mu_5^l(L)}{L^5} + 0.045 \frac{\mu_6^l(L)}{L^6} \right]. \quad (4-9)$$

The variance with piston and tilt removed is

$$\begin{aligned} \sigma_{ptRl}^2 = 0.5 D_s^{5/3} k_0^2 & \left[ \frac{\mu_{5/3}^l(L)}{L^{5/3}} - 0.877 \frac{\mu_2^l(L)}{L^2} + 0.94 \frac{\mu_3^l(L)}{L^3} - 2.014 \frac{\mu_4^l(L)}{L^4} \right. \\ & \left. + 1.204 \frac{\mu_5^l(L)}{L^5} - 0.322 \frac{\mu_6^l(L)}{L^6} \right]. \quad (4-10) \end{aligned}$$

For changes in the zenith angle, if the beacon is kept at the same altitude, it is clear from the variation of each of the terms in brackets that the zenith dependence of the variance is simply  $\sec(\xi)$ . To find the effect of the turbulence above the beacon one must use the filter function that removes piston and tilt which is

$$F(\bar{\kappa}, z) = 1 - \left[ \frac{2J_1(\kappa D/2)}{\kappa D/2} \right]^2 - \left[ \frac{4J_2(\kappa D/2)}{\kappa D/2} \right]^2. \quad (4-11)$$

Using Mellin transform techniques one can find the piston and tilt removed variance due to the turbulence above the beacons as

$$\sigma_{ptu}^2 = 0.0569 k_0^2 D^{5/3} \mu_0^h(L). \quad (4-12)$$

In this formula the total aperture diameter must be inserted. The contribution from the unsensed turbulence increases with increasing aperture size, and one finds that the beacon altitude must be increased for the larger diameters in order to keep this component manageable.

In Figure 4-2 the contributions from the turbulence below and above the beacon and their total are plotted for a single beacon operating with a 60-cm diameter aperture with the HV-21 turbulence model. The total variance is the amount that one expects from a single beacon system.

In Figure 4-3 the same results are plotted for the four beacon case. In this case the section diameter has been reduced by a factor of 2, which causes the lower contribution to the variance to be decreased by a factor of 3.17.

The upper contribution is the same in the 2 cases. To find the total variance requires the addition of the stitching error to the focal anisoplanatic contribution.

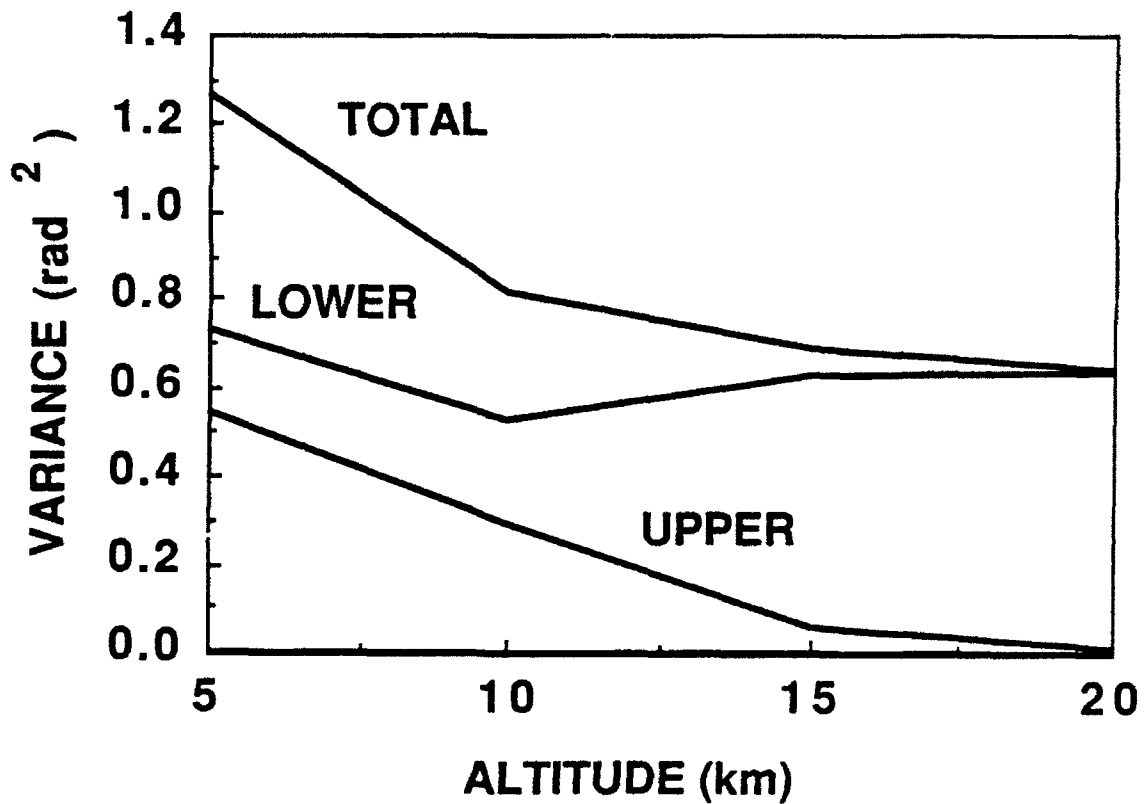


*Figure 4-2. Predicted SWAT phase variance as a function of beacon altitude for a single-beacon system with HV-21 turbulence. The turbulence components below and above the beacon are given, along with the total phase variance.*

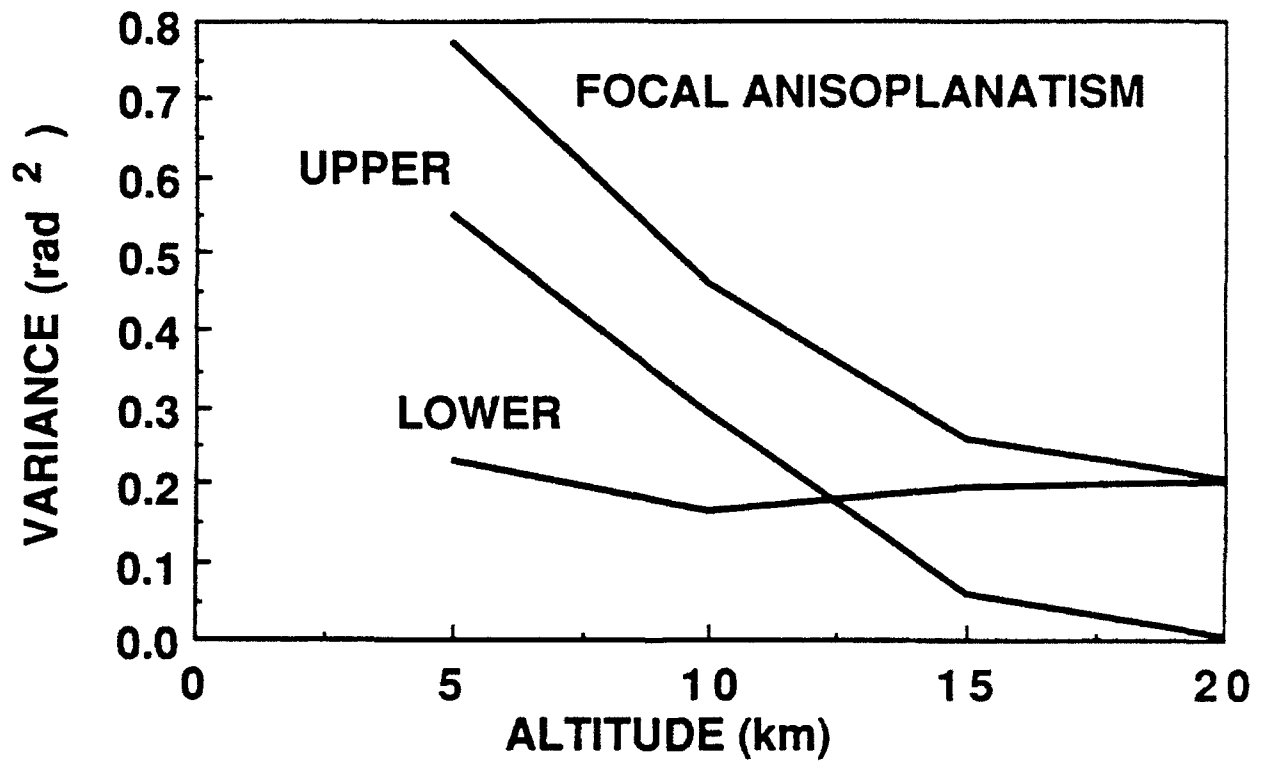


Figure 4-3. Predicted SWAT phase variance over a single section for a system with four synthetic beacons and HV-21 Turbulence. The turbulence components below and above the beacon are given, along with the total phase variance. Stitching effects are not included.

### 4.3 BEACON POSITION MEASUREMENT ERROR

If more than one beacon is used, the tilts of the individual sections must be measured. Errors in the measurements are important because the tilt component of turbulence is 87% of all the turbulence-induced phase variance with piston excluded. There are two errors in measuring the tilt. The first results from the difference in ray paths between a collimated and focused beam. This error was calculated in the last section. The other result from the beacons not being directly over the centers of the sections. Here it will be assumed that the beacons are projected up into the sky by some system and that their relative positions are measured by the full aperture of the system. Because of the difference in paths between the measurement rays through the turbulence, there will be a jitter in the apparent relative position of the beacons. This problem is analyzed in Appendix B. The filter function to find the tilt difference between focused displaced rays that are separated in space is the product of the tilt filter function and the one for anisoplanatism given by

$$F(\vec{\kappa}, z) = \left( \frac{16}{k_0 D} \right)^2 \left( \frac{J_2(\kappa D[1-z/L]/2)}{\kappa D[1-z/L]/2} \right)^2 2 \left[ 1 - \cos\{\vec{\kappa} \cdot \vec{d}(z)\} \right]. \quad (4-13)$$

Using this filter function the tilt variance is found to be

$$\begin{aligned} T_Z^2 = & \frac{10.68}{D^{1/3}} \int_0^{z_r/2} dz C_n^2(z) \left[ \left( \frac{bz}{DL} \right)^2 (1-z/L)^{-1/3} - 2.067 \left( \frac{bz}{DL} \right)^4 (1-z/L)^{-7/3} \right. \\ & \left. - 1.472 \left( \frac{bz}{DL} \right)^{14/3} (1-z/L)^{-3} + 0.339 \left( \frac{bz}{DL} \right)^6 (1-z/L)^{-13/3} + \dots \right] \\ & + \frac{12.16}{D^{1/3}} \int_{z_r/2}^L dz C_n^2(z) \left[ (1-z/L)^{5/3} - 0.6657 \left( \frac{DL}{bz} \right)^{1/3} (1-z/L)^2 - 0.00308 \left( \frac{DL}{bz} \right)^{7/3} (1-z/L)^4 \right. \\ & \left. - 3.06 \times 10^{-6} \left( \frac{DL}{bz} \right)^{13/3} (1-z/L)^6 - 6.15 \times 10^{-6} \left( \frac{DL}{bz} \right)^{19/3} (1-z/L)^8 + \dots \right]. \end{aligned} \quad (4-14)$$

The transition altitude between the low and high altitude solutions is given by

$$z_t = \frac{L}{b/D + 1}. \quad (4-15)$$

In Figure 4-4 both the variance from this tilt and the tilt component of focal anisoplanatism are plotted. The focal-anisoplanatic tilt is considerably larger than that due to misplacement.

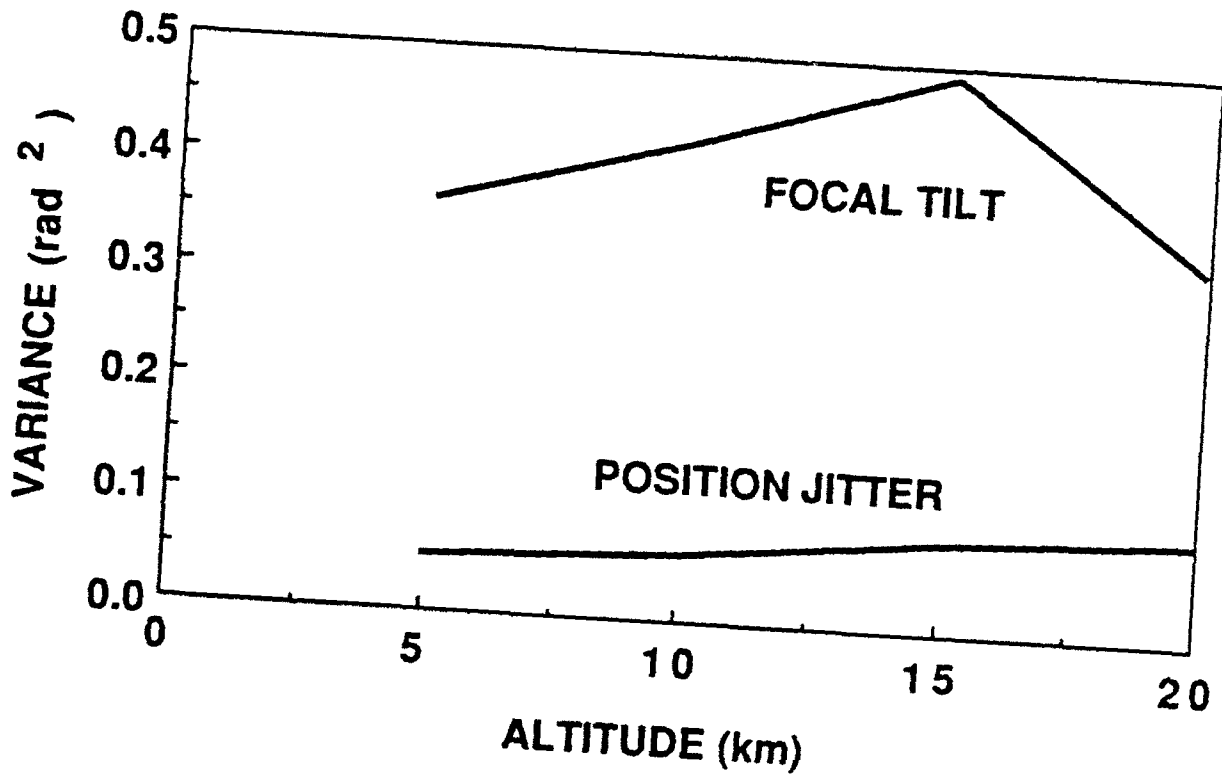
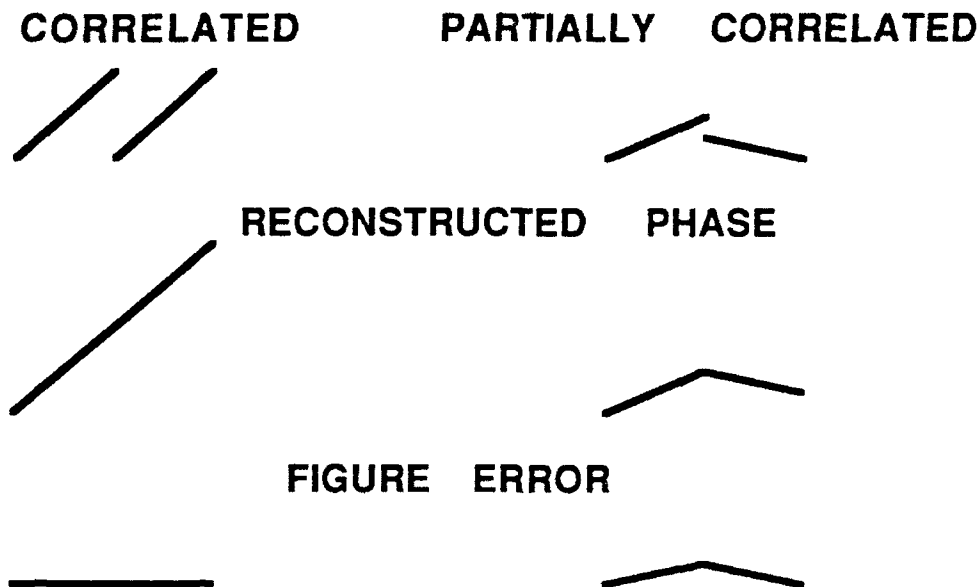


Figure 4-4. Phase variance of the jitter due to focal anisoplanatism and beacon-position measurement error for the SWAT system with HV-21 turbulence.

#### 4.4 CORRELATION FUNCTION OF THE TILT COMPONENT OF FOCAL ANISOPLANATISM

In calculating the error in stitching together the tilt errors of the individual sections, the correlation of the tilt is very important in determining the resulting phase variance with the tilt removed. For instance, in Figure 4-5 are shown the results from stitching together perfectly correlated tilts, and tilts that are partially correlated. In the perfectly correlated case, the resultant phase is composed solely of tilt, and the tilt-removed variance is zero.



*Figure 4-5. Stitching difference between correlated and uncorrelated tilts.*

For turbulence the correlation function of parallel components of tilt is a function of the angle of displacement with respect to the tilt. This correlation function as the angle varies is calculated in Appendix C and plotted in Figure 4-6 for parallel, perpendicular, and 45 degree displacements.

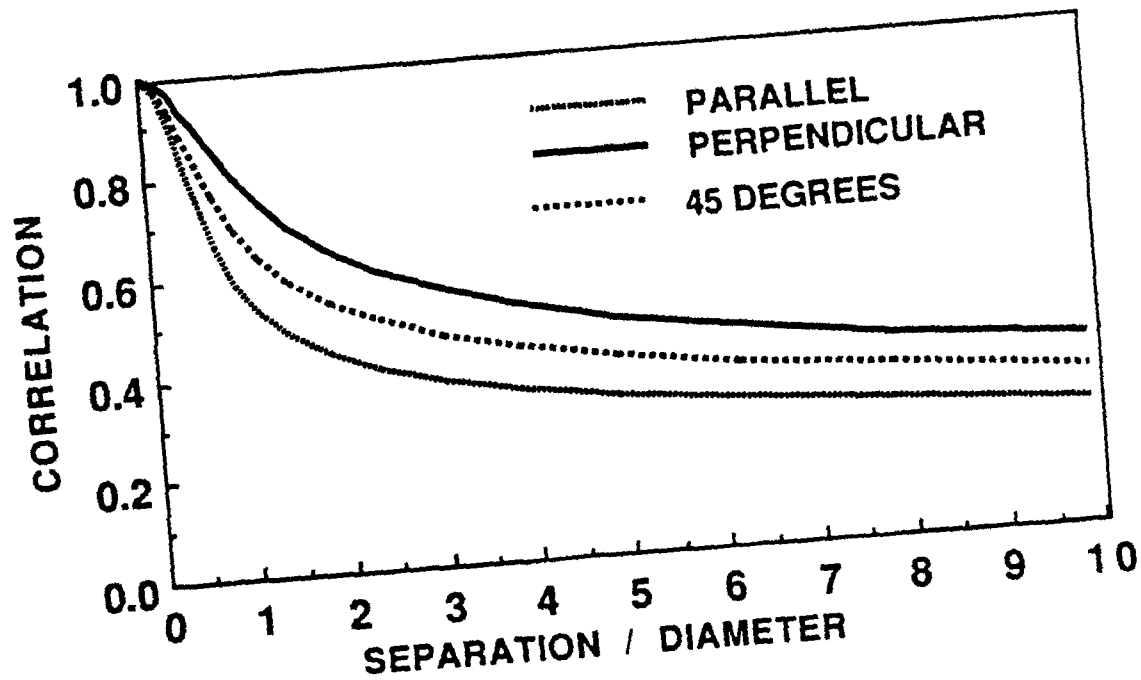


Figure 4-6. Correlation function for tilt on two apertures versus their separation distance and direction of separation relative to the tilt direction.

The perpendicular components of tilt are also correlated in certain directions. There is no correlation if the displacement is parallel to either tilt component. The correlation function for a displacement 45 degrees to the tilt is plotted in Figure 4-7.

#### 4.5 STITCHING MODEL AND RESULTS

Using the correlation function that was found, one can find the error propagator for the tilt stitching process. A model of an aperture with four beacons is given in Figure 4-8. The measurement model assumes that the gradient,  $m$ , is equal to a matrix,  $A$ , multiplying the  $N$  phase points,  $\phi$ , with an added measurement noise in the tilts,  $n_g$ . The gradient is given by

$$m = A\phi + n_g \quad (4-16)$$

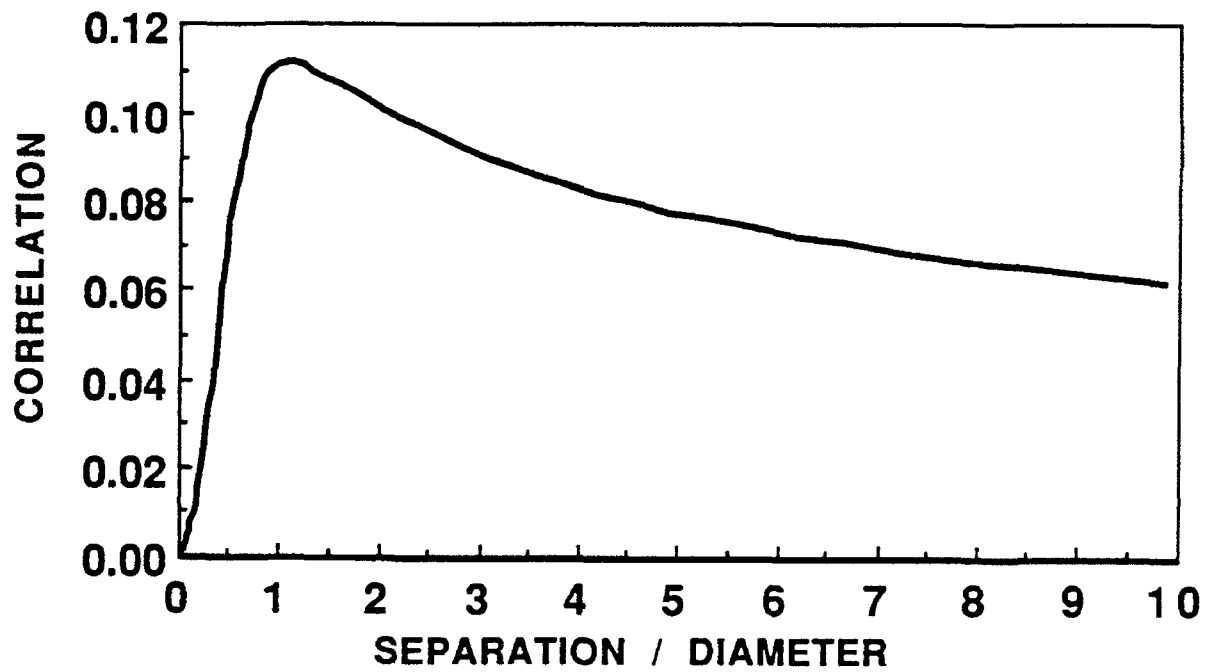


Figure 4-7. Correlation function for perpendicular components of tilt on an aperture versus the aperture separation in a direction 45 degrees to each tilt.

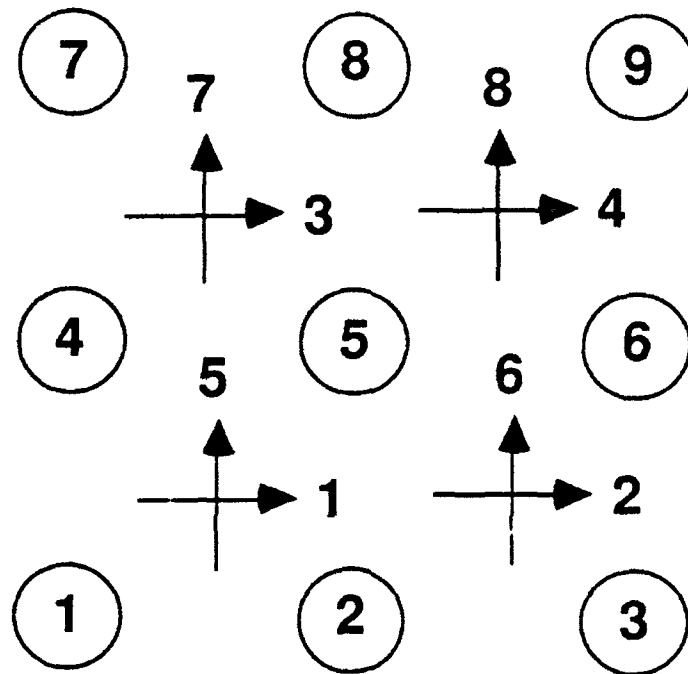


Figure 4-8. Aperture model for section stitching for a four-beacon system.

It is assumed that the signal-to-noise ratio is infinite, and the measurement noise is due to the phase-variance error incurred in propagating through turbulence. Each gradient is the average of the difference of the four phase points around that gradient, and is given by

$$A = 0.5 \begin{bmatrix} -1 & 1 & 0 & -1 & 1 & 0 & 0 & 0 & 0 \\ 0 & -1 & 1 & 0 & -1 & 1 & 0 & 0 & 0 \\ 0 & 0 & 0 & -1 & 1 & 0 & -1 & 1 & 0 \\ 0 & 0 & 0 & 0 & -1 & 1 & 0 & -1 & 1 \\ -1 & -1 & 0 & 1 & 1 & 0 & 0 & 0 & 0 \\ 0 & -1 & -1 & 0 & 1 & 1 & 0 & 0 & 0 \\ 0 & 0 & 0 & -1 & -1 & 0 & 1 & 1 & 0 \\ 0 & 0 & 0 & 0 & -1 & -1 & 0 & 1 & 1 \end{bmatrix} \quad (4-17)$$

The noise correlation matrix of the gradients is

$$C_n = \langle n_g n_g^T \rangle, \quad (4-18)$$

and it is explicitly equal to

$$C_n = \begin{bmatrix} 1 & i & p & q & 0 & 0 & 0 & r \\ i & 1 & q & p & 0 & 0 & r & 0 \\ p & q & 1 & i & 0 & r & 0 & 0 \\ q & p & i & 1 & r & 0 & 0 & 0 \\ 0 & 0 & 0 & r & 1 & i & p & q \\ 0 & 0 & r & 0 & i & 1 & q & p \\ 0 & r & 0 & 0 & p & q & 1 & i \\ r & 0 & 0 & 0 & q & p & i & 1 \end{bmatrix}, \quad (4-19)$$

where  $i = 0.558$ ,  $p = 0.778$ ,  $q = 0.594$ , and  $r = 0.109$ . These values come from the tilt correlation curves given in Figures 4-6 and 4-7.

The least squares solution for the phase is

$$\tilde{\phi} = (A^T C_n^{-1} A)^+ A^T C_n^{-1} m = Lm, \quad (4-20)$$

where the superscript + is the symbol for the generalized inverse that is necessary because the matrix has some singular values.

The tilt and piston removed phase is

$$\tilde{\phi}_{ipR} = \Lambda \left( \mathbf{A}^T \mathbf{C}_n^{-1} \mathbf{A} \right)^+ \mathbf{A}^T \mathbf{C}_n^{-1} m = \Lambda \mathbf{L} m . \quad (4-21)$$

$\mathbf{L}$  is the tilt removal matrix that is a combination of x and y-tilt removal given by

$$\Lambda = 1 - t_x^T t_x - t_y^T t_y , \quad (4-22)$$

where

$$t_x = 0.5[-1 \ 0 \ 1 \ -1 \ 0 \ 1 \ -1 \ 0 \ 1] , \quad (4-23)$$

and

$$t_y = 0.5[-1 \ -1 \ -1 \ 0 \ 0 \ 0 \ 1 \ 1 \ 1] . \quad (4-24)$$

The piston does not have to be explicitly removed since the  $\mathbf{A}$  matrix already has removed it. The error in the estimate can be shown to be

$$\text{Error} = \mathbf{L} \mathbf{C}_n \mathbf{L}^T , \quad (4-25)$$

and the error propagator is

$$\text{Error Propagator} = \frac{1}{N} \text{Trace} \left[ \Lambda \left( \mathbf{A}^T \mathbf{C}_n^{-1} \mathbf{A} \right)^+ \Lambda^T \right] . \quad (4-26)$$

The error propagator for the SWAT system is 0.426, which means that less than half the phase variance due to tilt jitter is effective in causing a figure variance of the stitched beam. With these results the performance of a 4-beacon system at zenith and at 45 degrees off zenith are found and plotted for various altitudes in Figure 4-9.

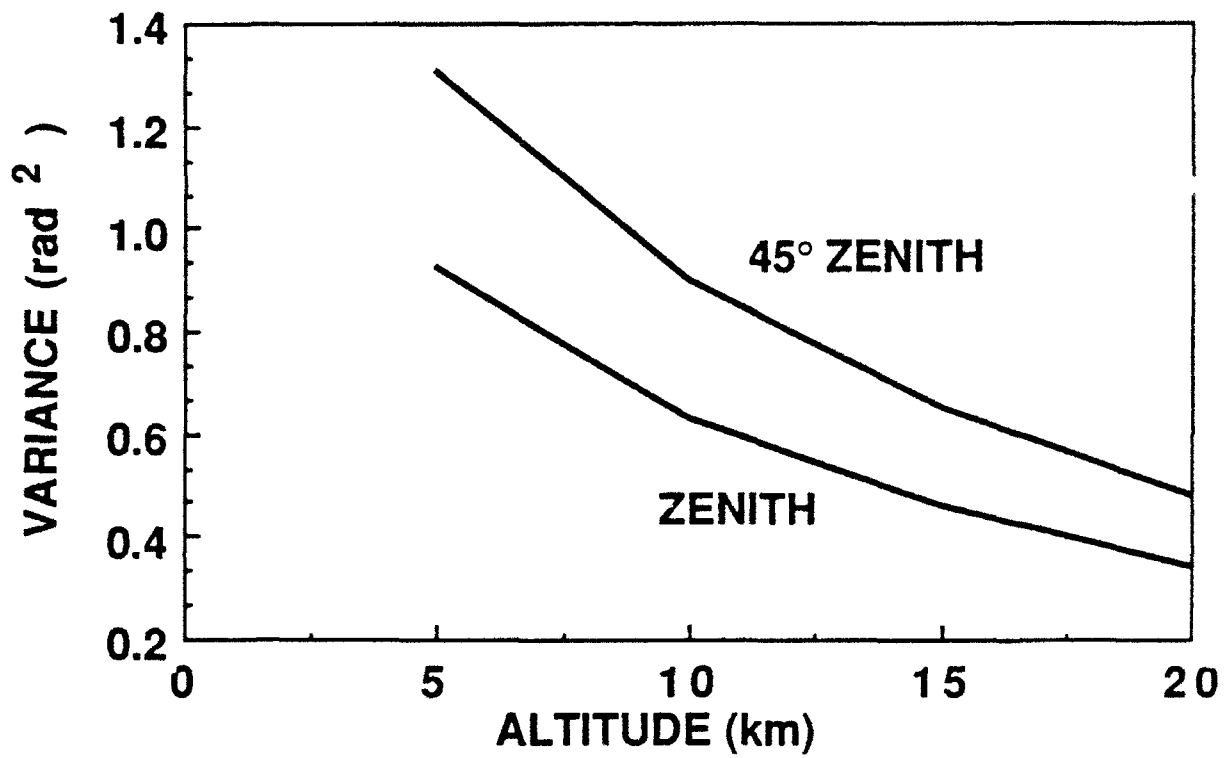


Figure 4-9. Predicted Swat performance with four synthetic beacons as a function of beacon altitude and zenith angle for the HV-21 model. Stitching effects have been included.

## 5. SWAT PERFORMANCE PREDICTIONS

The SWAT experimental hardware has the capability to probe an extensive range of system parameters relevant to both Rayleigh-beacon and sodium-beacon deployment strategies. In this section the more important of these effects are studied using the analytic and numerical simulation approaches previously described. In order to permit these data to be easily accessed, each of the figures provided in this section will have a standard presentation format that includes a chart comparing near-field variance for the HV-21 model using the two analysis procedures and a second graph containing Strehl predictions for the HV-21 and SLC-Day models obtained from the numerical simulation. In all of the cases presented, the agreement between the two analysis procedures is found to be excellent.

Default parameters for the next set of performance curves are summarized in Table 5-1. Unless otherwise indicated, the pertinent analysis inputs are as specified in this list. In all cases it should be assumed that turbulence effects dominate performance .

**TABLE 5-1**  
**Baseline Simulation Parameters**

<b>Atmospheric Model :</b>	HV-21
<b>Aperture Diameter :</b>	55 cm, no obscuration
<b>Beacon Wavelength :</b>	500 nm
<b>HEL Wavelength :</b>	500 nm
<b>Zenith Angle :</b>	0°
<b>Source Geometry :</b>	Single Source
<b>Source Range :</b>	5 km
<b>Source Diameter :</b>	Point Source

## 5.1 SINGLE-BEACON PERFORMANCE ESTIMATES

The first series of SWAT experiments will study the degree of turbulence correction that can be achieved with a single Rayleigh beacon. With this geometry the main contributors to the figure variance will be the unsampled atmosphere above the beacon, focal anisoplanatism below the beacon, and anisoplanatic errors due to beacon misplacement.

### 5.1.1 Beacon-Altitude Dependence

The upper chart in Figure 5-1 shows the expected figure variance as a function of beacon altitude between 2 and 15 km for a point source at zenith. The numerical and analytical results are given by the dashed and solid curves respectively. The agreement between the two computational approaches is seen to be extremely good over the entire parameter range.

The figure-Strehl predictions derived from the numerical study are summarized in the lower chart of Figure 5-1, where the HV-21 and SLC-Day results have been represented by the dashed and solid curves respectively. Note that the two models show a cross-over point at the baseline altitude of 5 km, and differ by only 30% for a 15 km scattering altitude. On the basis of this analysis, one would place a rough upper limit of 0.5 on the achievable Strehl for single-beacon Rayleigh correction for scattering altitudes between 5 and 10 km.

### 5.1.2 Zenith-Angle Dependence

As discussed in Section 4.2, both the upper-altitude and lower-altitude figure-error components associated with synthetic beacons have an explicit  $\sec(\xi)$  dependence for a fixed source altitude  $H$ . For a fixed range,  $L$ , the error variance displays a faster angular dependence due to the  $\cos(\xi)$  reduction in beacon altitude. These effects are illustrated in Figure 5-2 for a 5-km beacon range and zenith angles between  $0^\circ$  and  $60^\circ$ .

### 5.1.3 Beacon-Offset Dependence

One of the many experiments proposed in the original SWAT test plan involves the displacement of the beacon from its nominal point-ahead position, as a means of measuring tilt anisoplanatic effects. Although  $\theta_o$  is about  $10 \mu\text{rad}$  for both the HV-21 and SLC-Day models, Figure 5-3 shows that essentially no degradation is predicted for beacon offset angles as large as  $15 \mu\text{rad}$ . This response can be attributed to an effect that might be labeled the "fractional isoplanatic angle", which is related to the  $5/3$  turbulence integral between the transmitter and the beacon altitude. For the baseline conditions in which a 5 km source is used to probe HV-21 a turbulence profile, the fractional isoplanatic angle is approximately  $25 \mu\text{rad}$ .

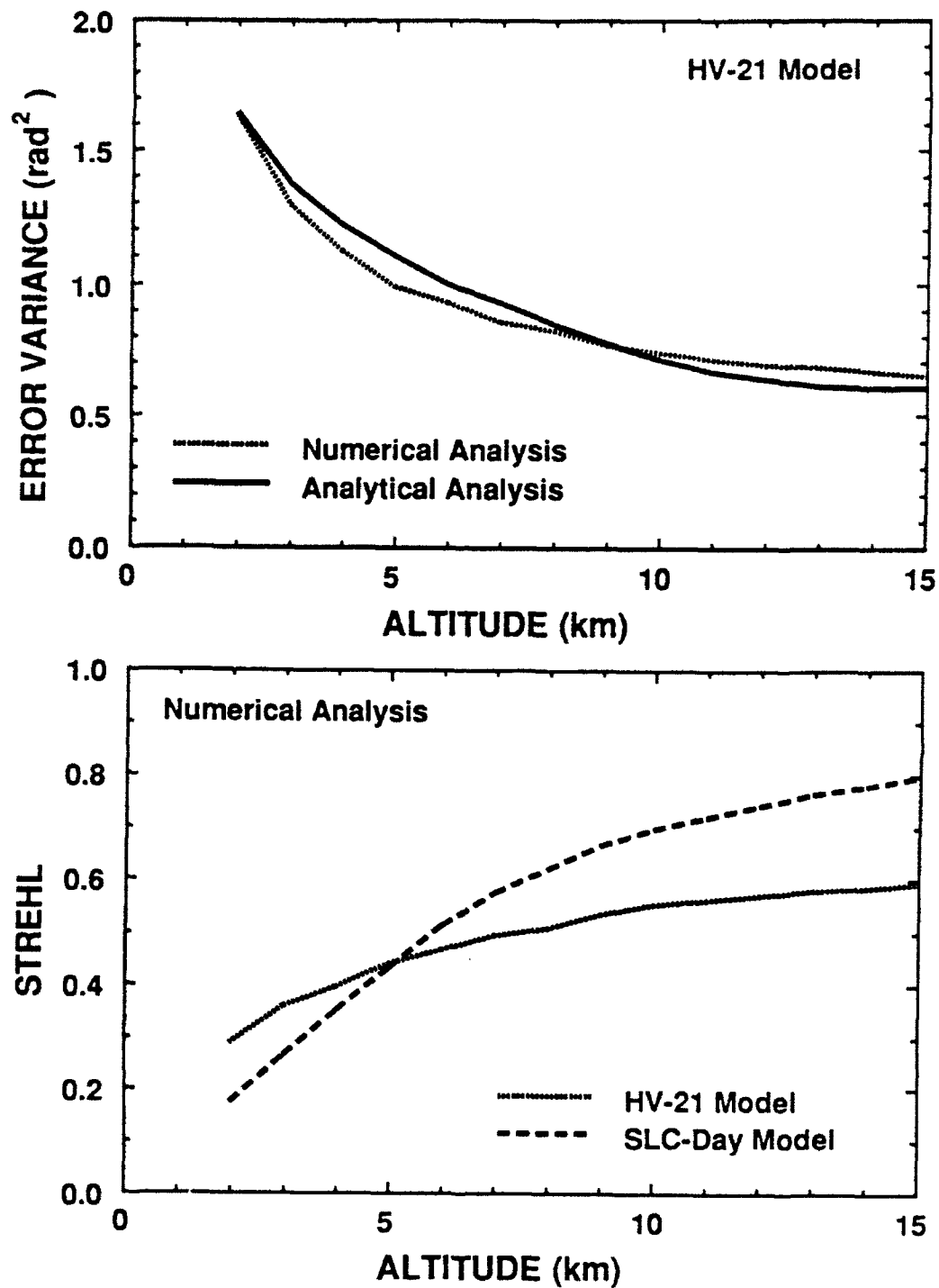


Figure 5-1. Single-beacon performance as a function of beacon altitude. Calculations are performed at zenith for a 500 nm beam.

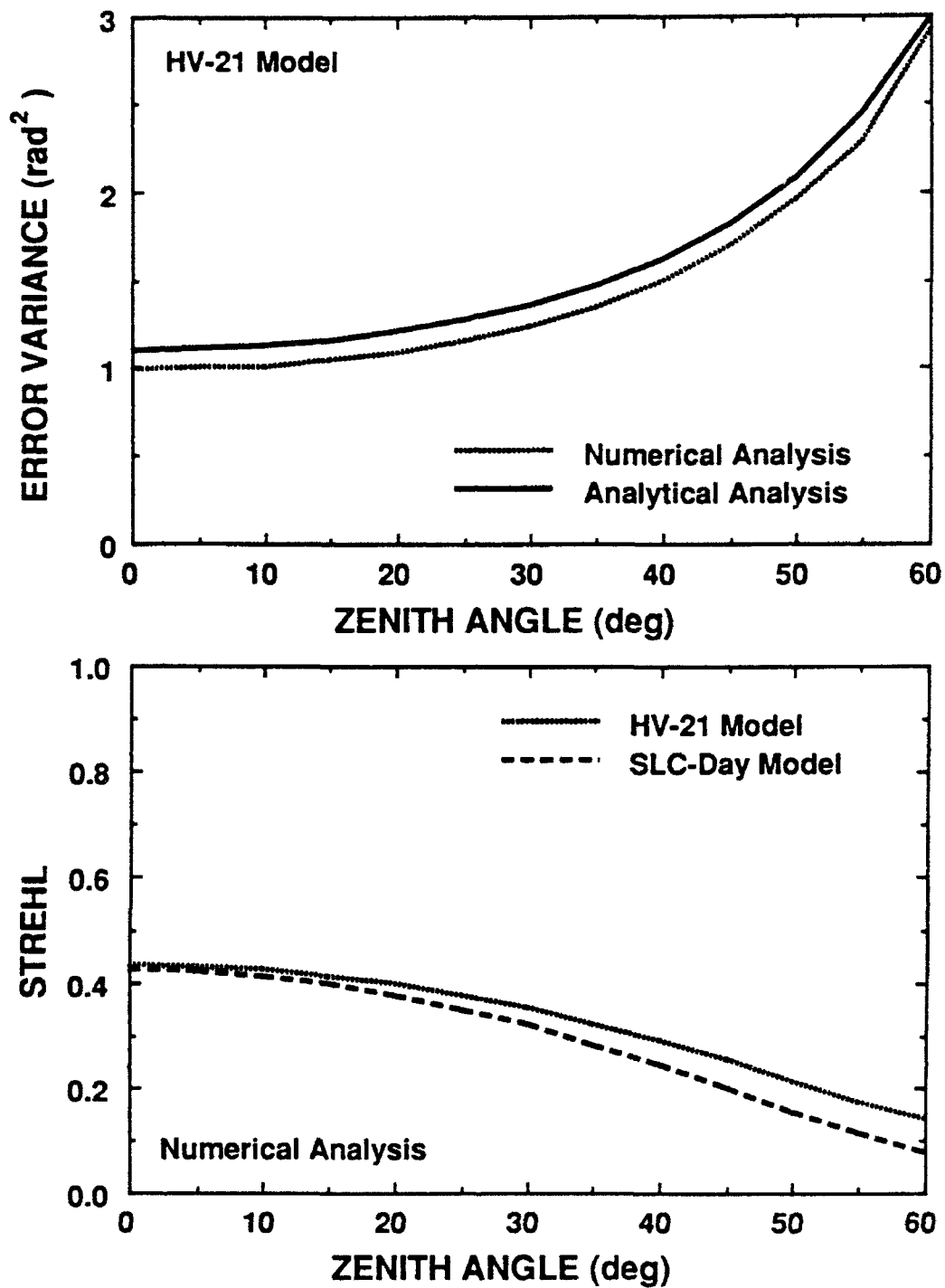


Figure 5-2. Single-beacon performance as a function of zenith angle for a beacon range of 5 km.

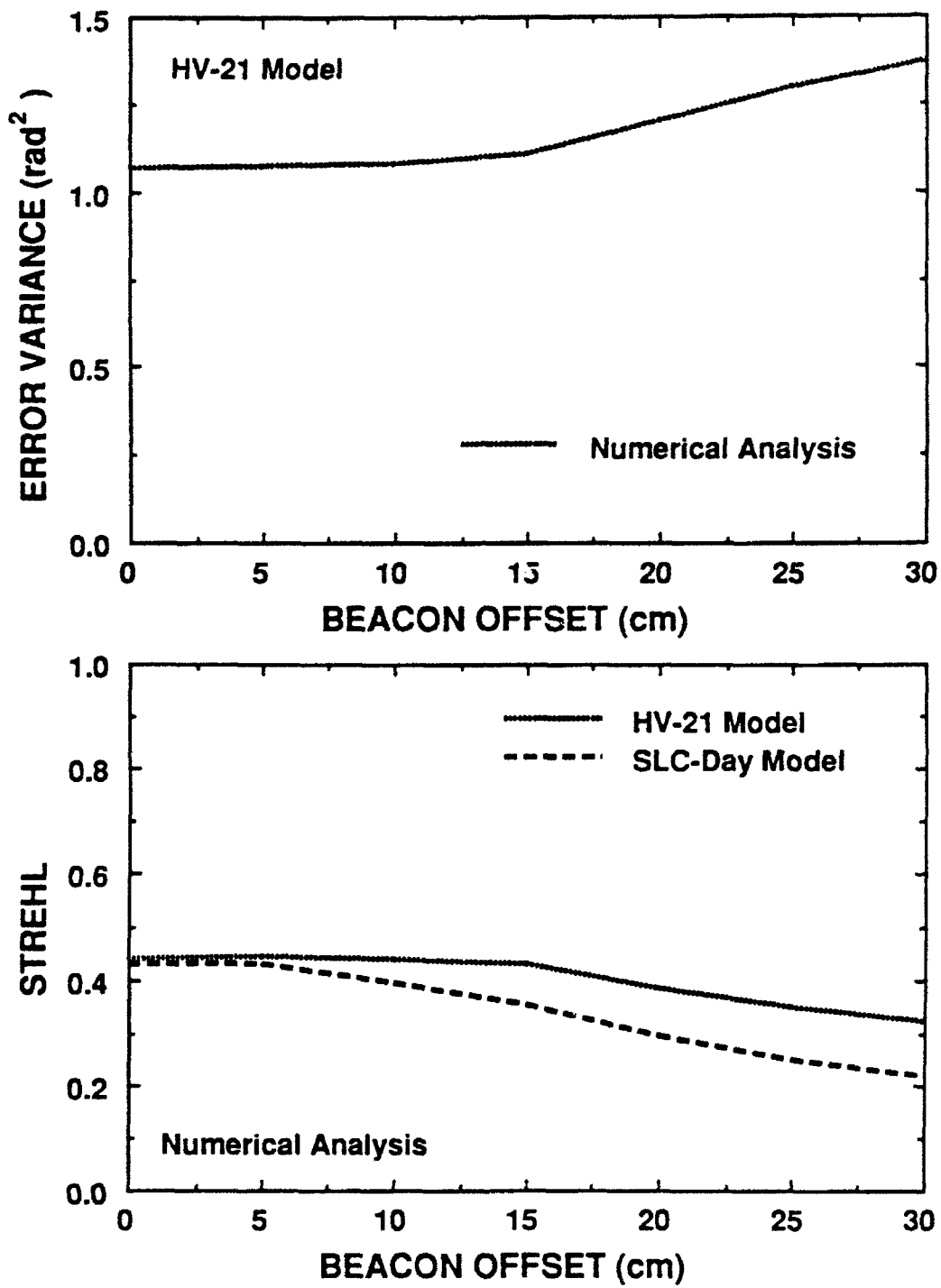


Figure 5-3. Single-beacon performance as a function of source displacement. The beacon altitude is 5 km and the zenith angle is 0.

#### **5.1.4 Beacon-Size Dependence**

The generation of synthetic beacons using Rayleigh or resonance backscatter requires a non-trivial expenditure of laser energy, and this task can be greatly simplified if beams of relatively poor quality can be employed. Following the same logic applied above, one would expect that beam diameters of the order of the fractional isoplanatic angle would provide adequate performance. This effect is demonstrated in Figure 5-4, in which virtually no change in figure variance is indicated for beacon profiles as large as 60 cm. This result, which has been confirmed by an independent study, predicts that compensated beacons will not be a requirement for the SWAT experiments. The current design of the SWAT dye-laser system assumes that beam quality values in the range of 10 to 20 are tolerable.

### **5.2 PERFORMANCE ESTIMATES FOR FOUR BEACONS**

As discussed in Section 2 of this report, the use of multiple synthetic beacons has been proposed as a means of reducing low-altitude focal anisoplanatism, thus allowing the synthetic beacon concept to be applied to apertures of arbitrary extent. The SWAT system is equipped to deploy as many as five dye-laser beams in rapid sequence. This capability will permit direct comparisons of single and multiple-beacon performance for a variety of altitudes, zenith angles, and source displacements. The two most important tests to be conducted with this four-beacon geometry are described below.

#### **5.2.1 Beacon-Altitude Dependence**

As shown in Figure 2-2, the four-beacon SWAT experiment will place one source over the center of each of four aperture quadrants. In the simulation process, phase gradients are derived from the associated artificial source within each quadrant, and overall tilt measurements of each beacon are made as a means of removing anomalous section tilts. Finally, a standard Gauss estimator is used to convert the corrected gradients into a single phase array. The expected figure variance and Strehl ratio values related to this process are given in Figure 5-5 as a function of beacon altitude.

The results shown in this figure can be directly compared to the single-source calculations presented in Figure 5-1. For the baseline altitude of 5 km, a Strehl improvement of about 25% is obtained for both the HV-21 and SLC-Day models.

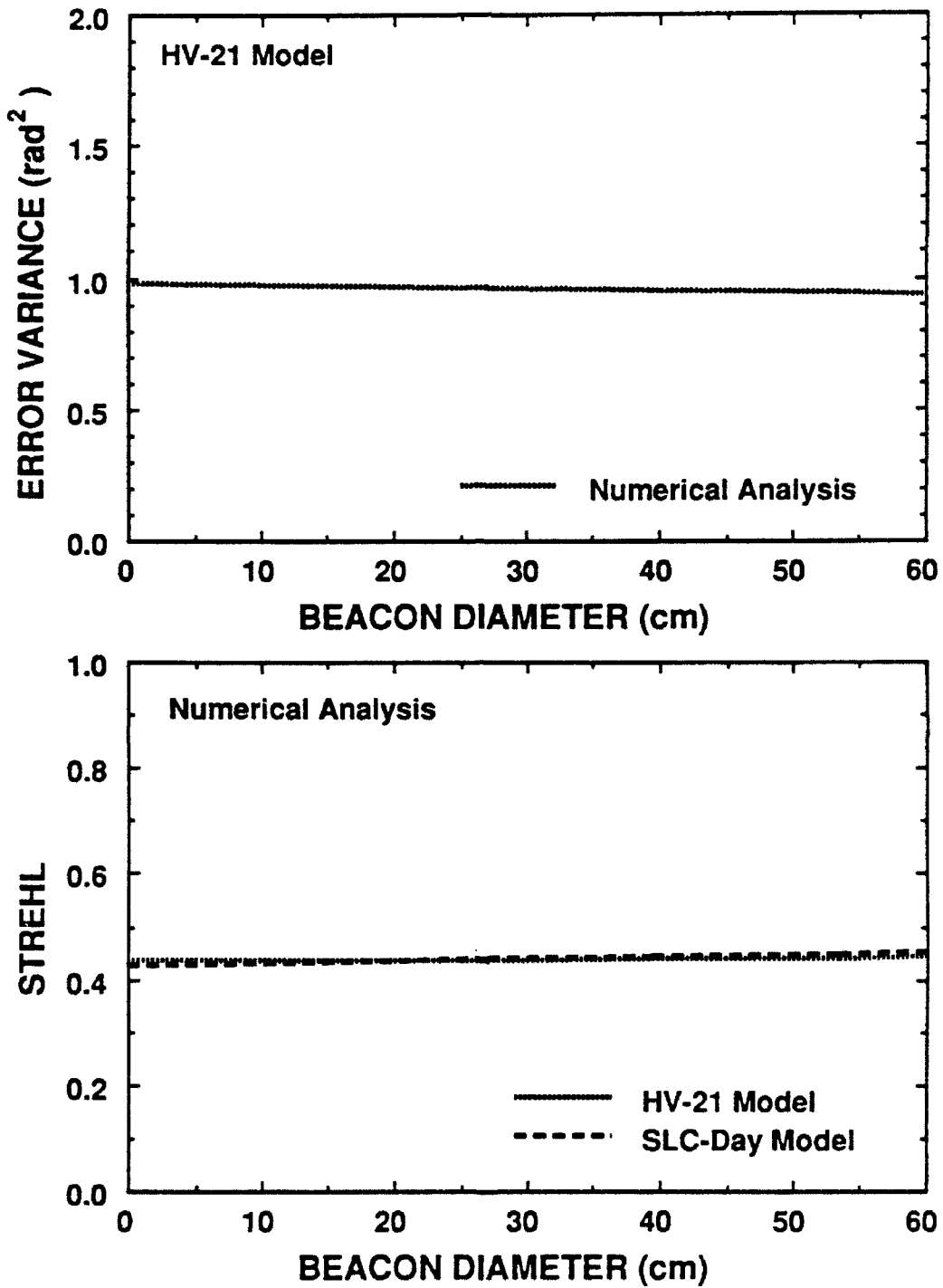


Figure 5-4. Single-beacon performance as a function of beacon diameter. The beacon altitude is 5 km and the zenith angle is 0°.

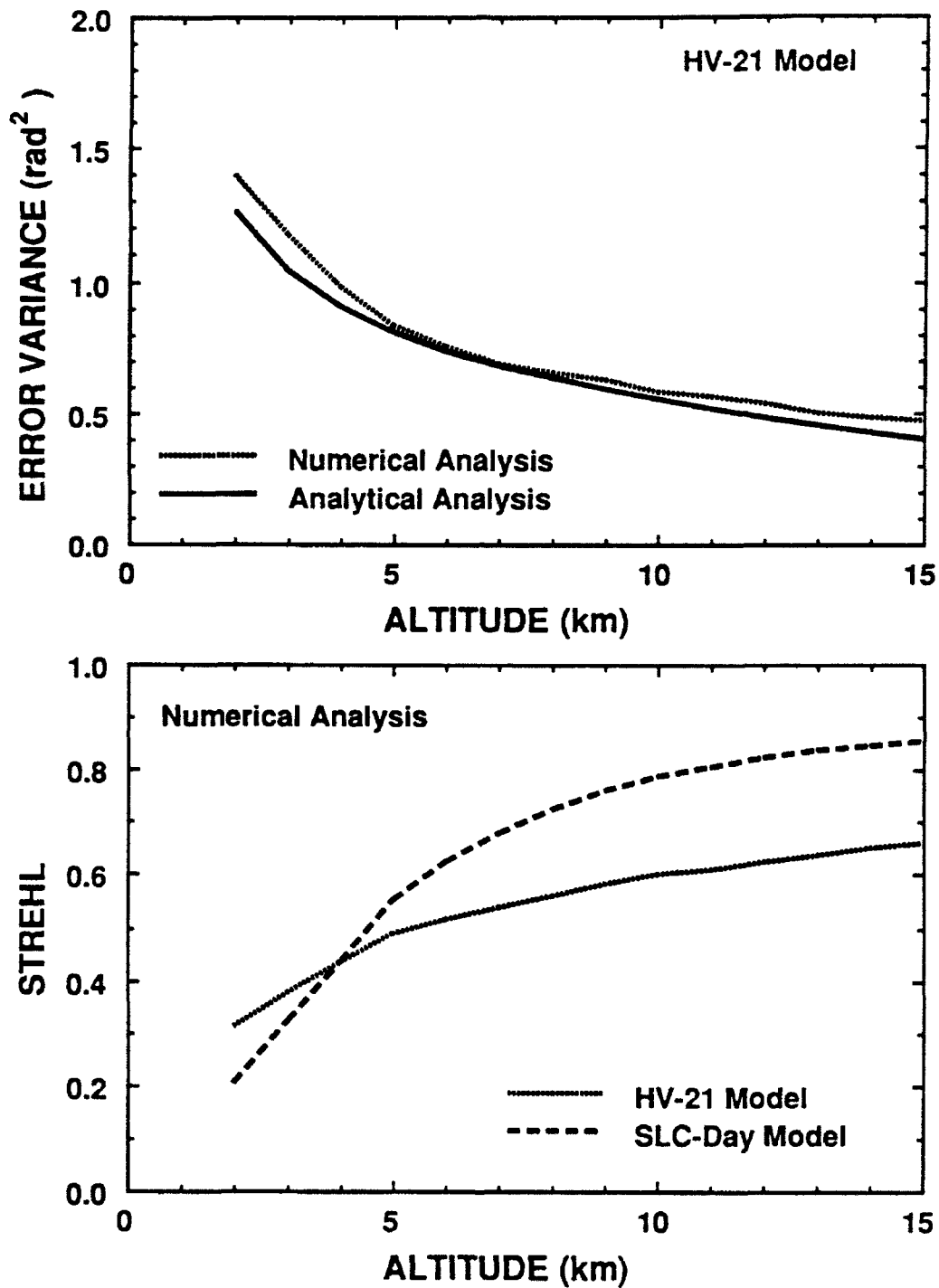


Figure 5-5. Four-beacon performance as a function of beacon altitude. Calculations are performed at zenith for a 500 nm HEL.

### 5.2.2 Error Due to Beacon Misplacement

The purpose of the section-stitching algorithm is to render the gradient measurements insensitive to small changes in relative beacon placement due to atmospheric effects or imperfections in the beam-placement system. Figure 5-6 shows the performance as a function of the magnitude of the beacon-placement error with respect to the center of the aperture section. Note that essentially no change is seen for placement errors as large as  $\pm 15$  cm.

## 5.3 DUAL-ALTITUDE GEOMETRIES

One way to obtain the benefit of a high-altitude source while retaining an acceptable signal level is to perform the phase correction in two distinct stages: the first stage entails a conventional Rayleigh measurement using  $r_0$ -sized subapertures that provide high-spatial-frequency information, and the second entails section-tilt measurements by large subapertures viewing the returns from a more distant beacon. This so-called dual-altitude, or hybrid approach can be implemented with illumination sources of relatively modest power. A 0.5-J laser pump at the sodium resonance wavelength has already been constructed for this purpose.<sup>3</sup>

### 5.3.1 Single Rayleigh Beacon with One Sodium Beacon

The physical structure of the high-altitude gradient subapertures need not be matched to the number of beacons used in the low altitude array. The high-altitude measurements serve to provide tilt corrections over contiguous aperture sections that can be arbitrarily specified. In the analysis described in Figure 5-7, section-tilt measurements derived from a 90-km source were applied to aperture quadrants subsequent to a phase reconstruction based on low-altitude gradients obtained from a single beacon. The results are given as a function of the position of the low-altitude source. When compared with Figure 5-1, it can be seen that this hybrid scheme provides a 45% Strehl improvement over the performance of a single beacon at 5 km.

### 5.3.2 Four Rayleigh Beacons with One Sodium Beacon

Dual-altitude turbulence sampling was originally proposed as a means of removing the residual section-tilts associated with multiple-beacon stitching algorithms. Figure 5-8 gives performance estimates for a hybrid scheme in which an initial phase is obtained from a four-beacon Rayleigh geometry, followed by section-tilt correction using gradient measurements provided by a sodium source. This five-source compensation process yields roughly a 20% higher Strehl than the hybrid approach in which a single Rayleigh beacon is deployed.

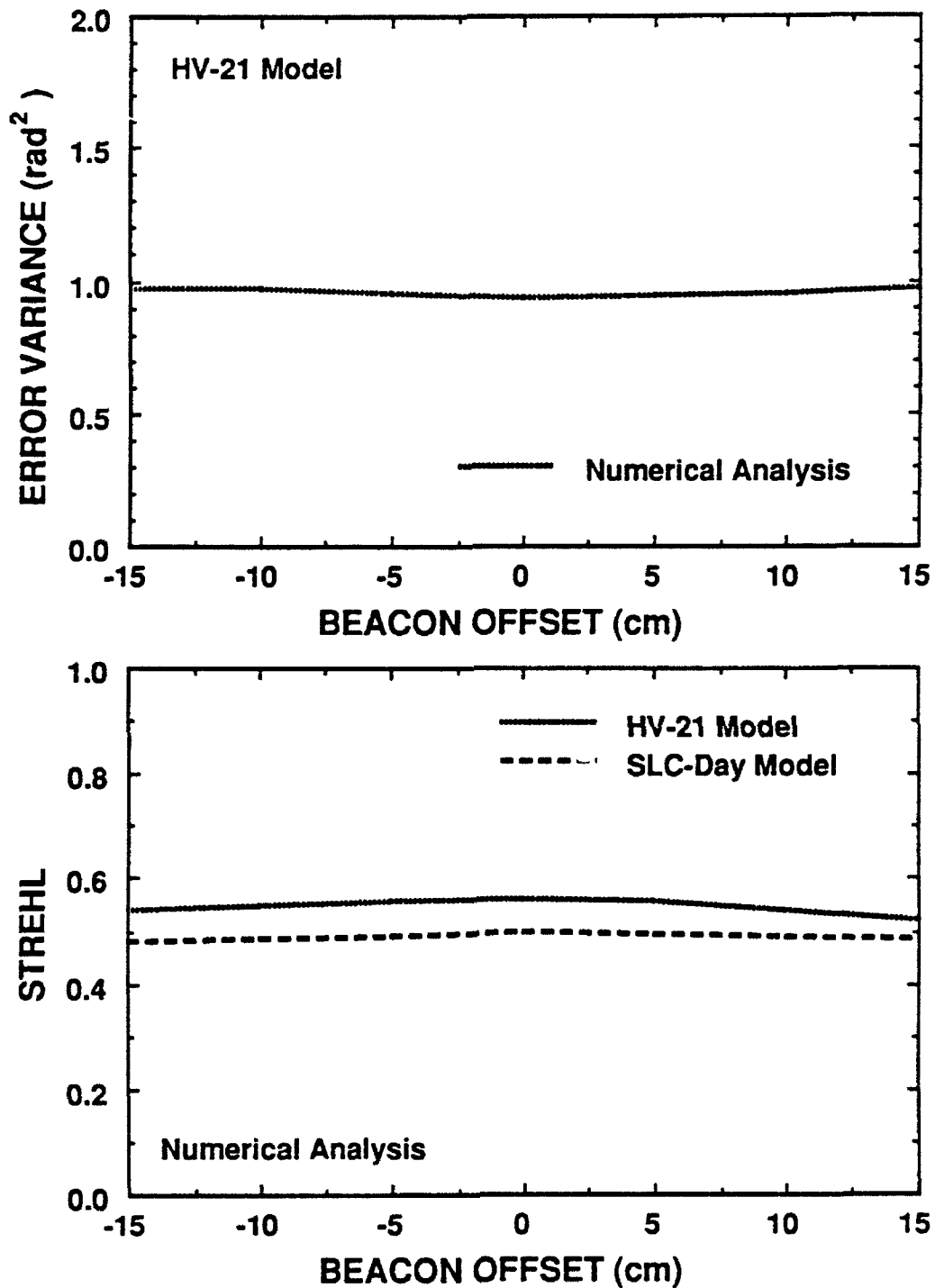


Figure 5-6. Performance of a four-beacon system with one beacon displaced from the center of its section. The displacement is radial with respect to the center of the full aperture.

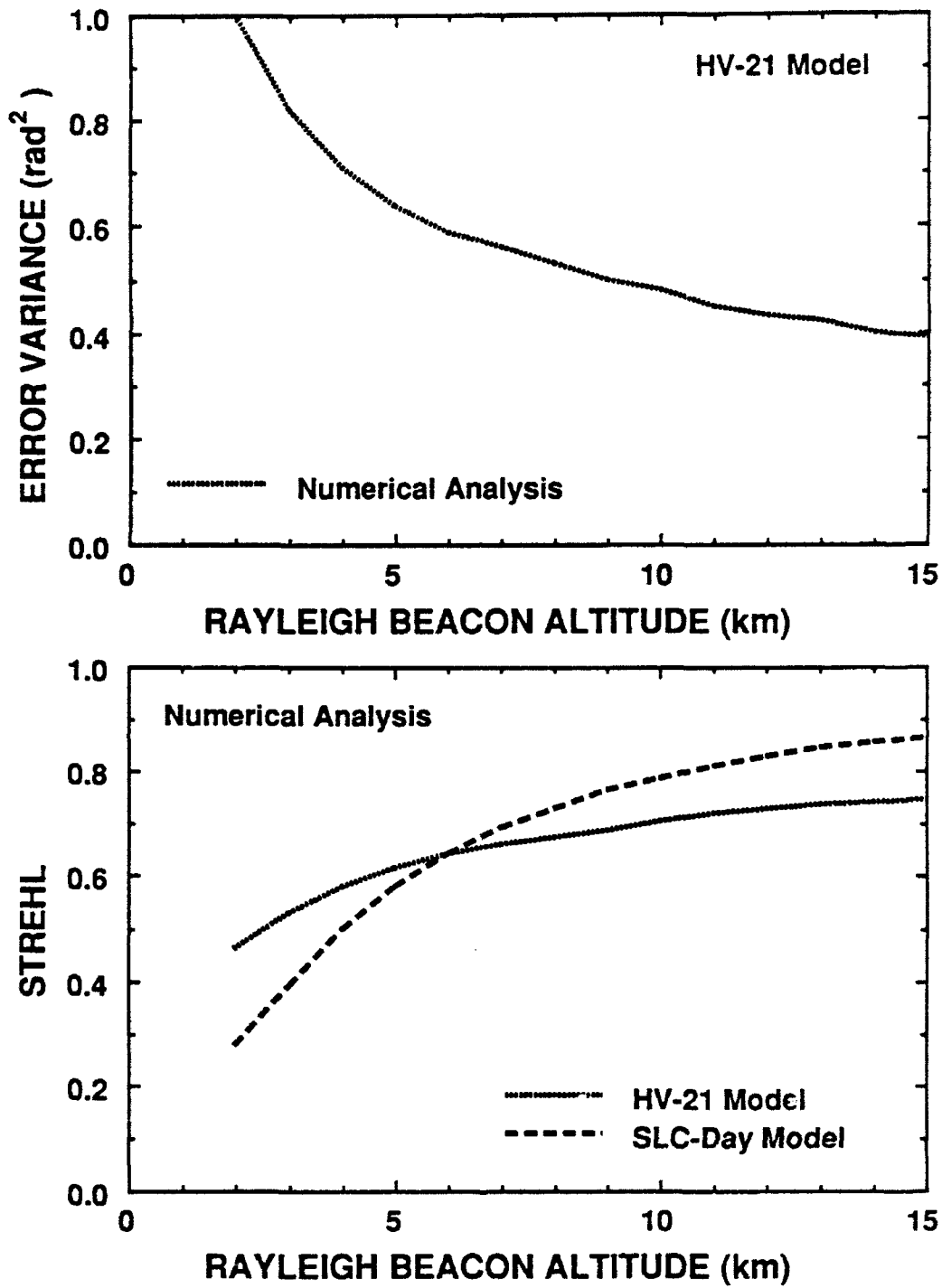


Figure 5-7. Analysis of a hybrid-beacon geometry in which the high-spatial-frequency information is derived from a single beacon placed at the specified altitude and tilt correction is subsequently applied to aperture quadrants based on returns from a single 90-km source.

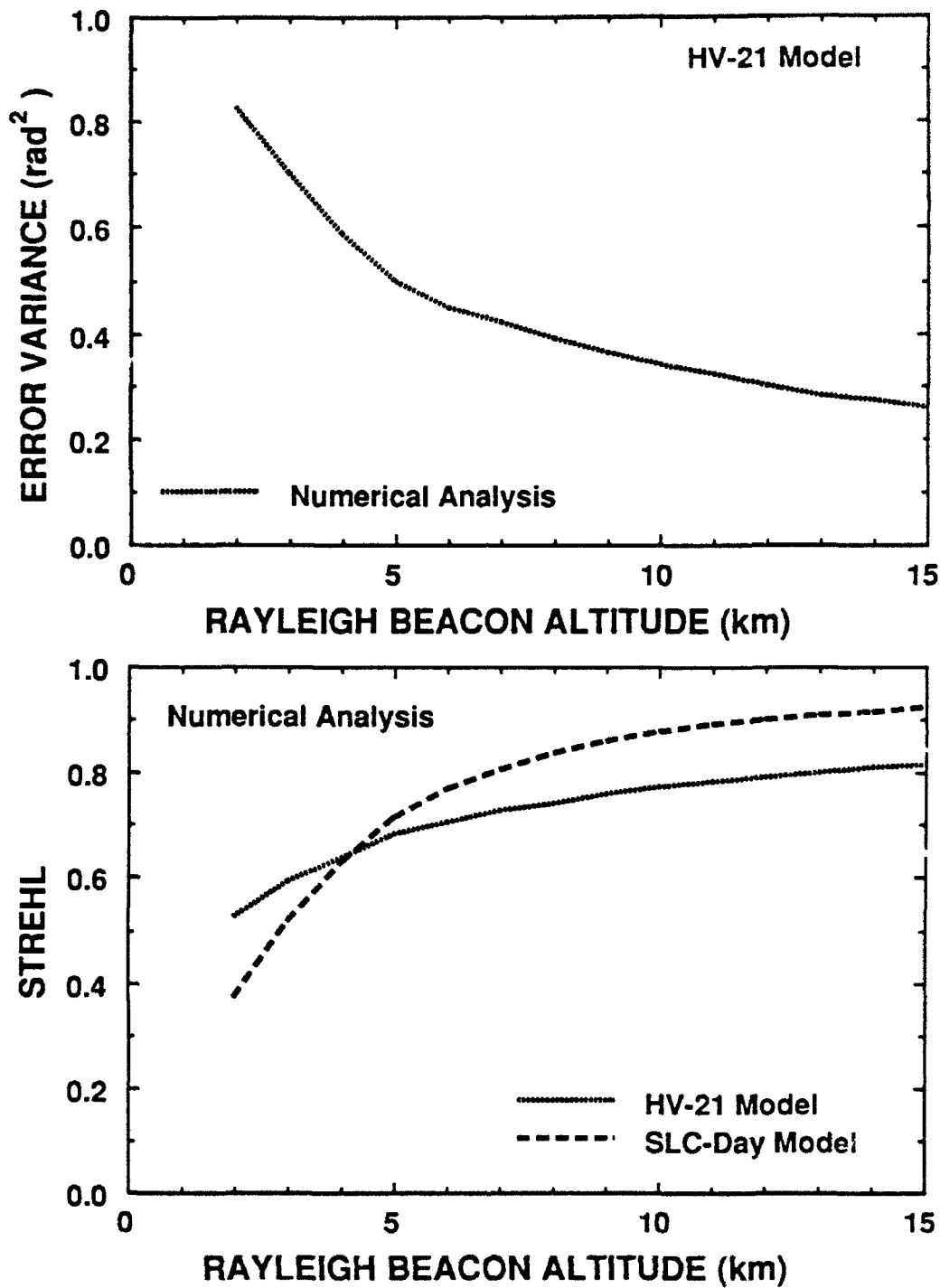


Figure 5-8. Analysis of a hybrid-beacon geometry in which the high-spatial-frequency information is derived from a set of four beacons placed at the specified altitude and tilt correction is subsequently applied to the four aperture sections based on returns from a single 90-km source.

## 5.4 PERFORMANCE COMPARISONS FOR THE PRINCIPAL BEACON GEOMETRIES

A summary of the performance results developed in this section is presented in Figures 5-9 and 5-10. Both illustrations provide Strehl estimates for the HV-21 and SLC-Day models based on output from the numerical code ELVIRA. The four principal beacon geometries are described for a range of altitudes and zenith angles. These constructs include single-altitude one and four-source arrays, along with the associated hybrid schemes in which a sodium source is used to sense residual section tilts.

A number of general observations can be made on the basis of the curves shown in Figures 5-9 and 5-10. These comments have direct relevance to experimental priorities for future SWAT field tests.

- 1) The Strehl curves are not strongly model dependent and probably represent worst-case examples for night-time operation at the Maui observatory. It should be noted, however, that all calculations have assumed high signal-to-noise in both the wavefront sensor and far-field scoring camera.
- 2) Far-field performance at small zenith angles is expected to be relatively insensitive to beacon altitude between 7 and 15 km. Above 7 km most of the strong turbulence is well characterized and focal anisoplanatic effects for a 60-cm aperture are not severe. For this reason it is likely that the 5-7 km range will be of most interest in order to maintain a strong signal level.
- 3) An enhancement in Strehl between the four-beacon and single-beacon configuration is likely to be difficult to measure. On this point the results from the two turbulence models are somewhat different, but under no conditions is the improvement expected to be larger than 30%. In order to detect a factor of this magnitude, the SWAT hardware will need to be operating close to its theoretical limit, and a large sample ensemble will be required to provide good measurement statistics. There appears to be a significantly higher probability of distinguishing between the single-altitude and hybrid-sensing geometries.

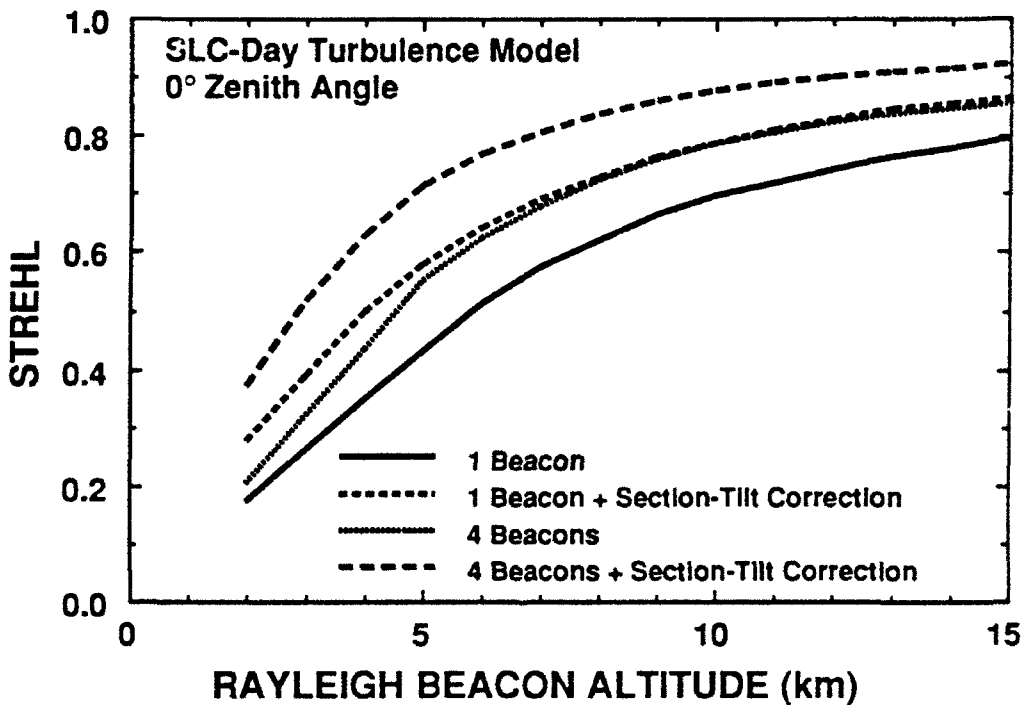
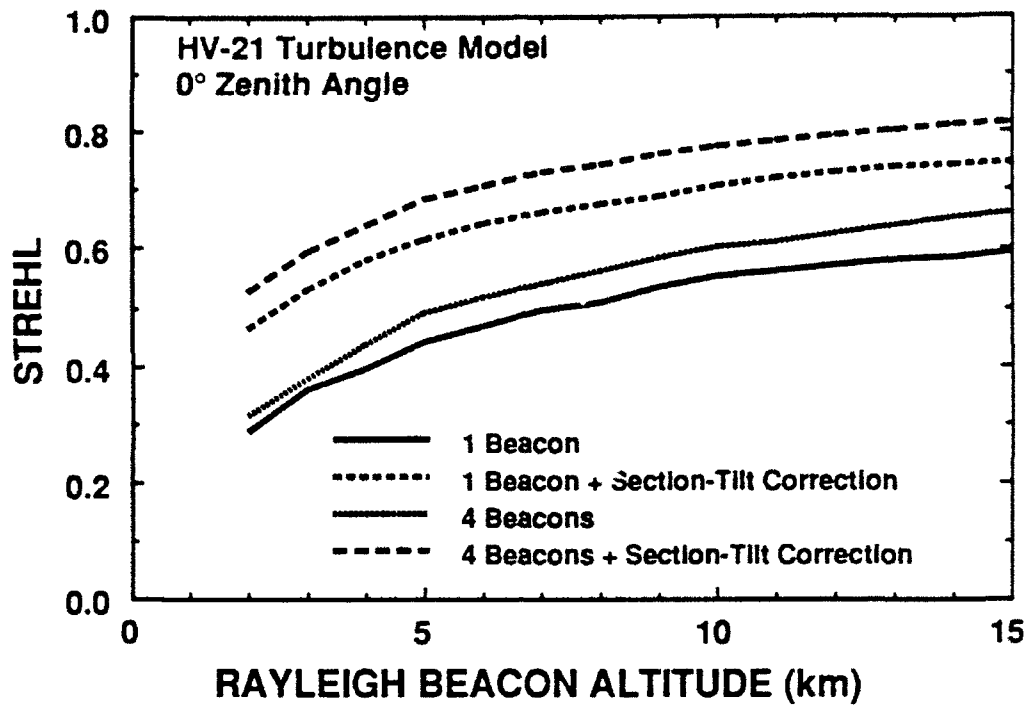


Figure 5-9. Comparison of far-field performance for the four major beacon geometries scheduled for test by the SWAT experimental system as a function of the position of the low-altitude beacon array. Quadrant-tilt correction is derived from a single beacon at 90 km.

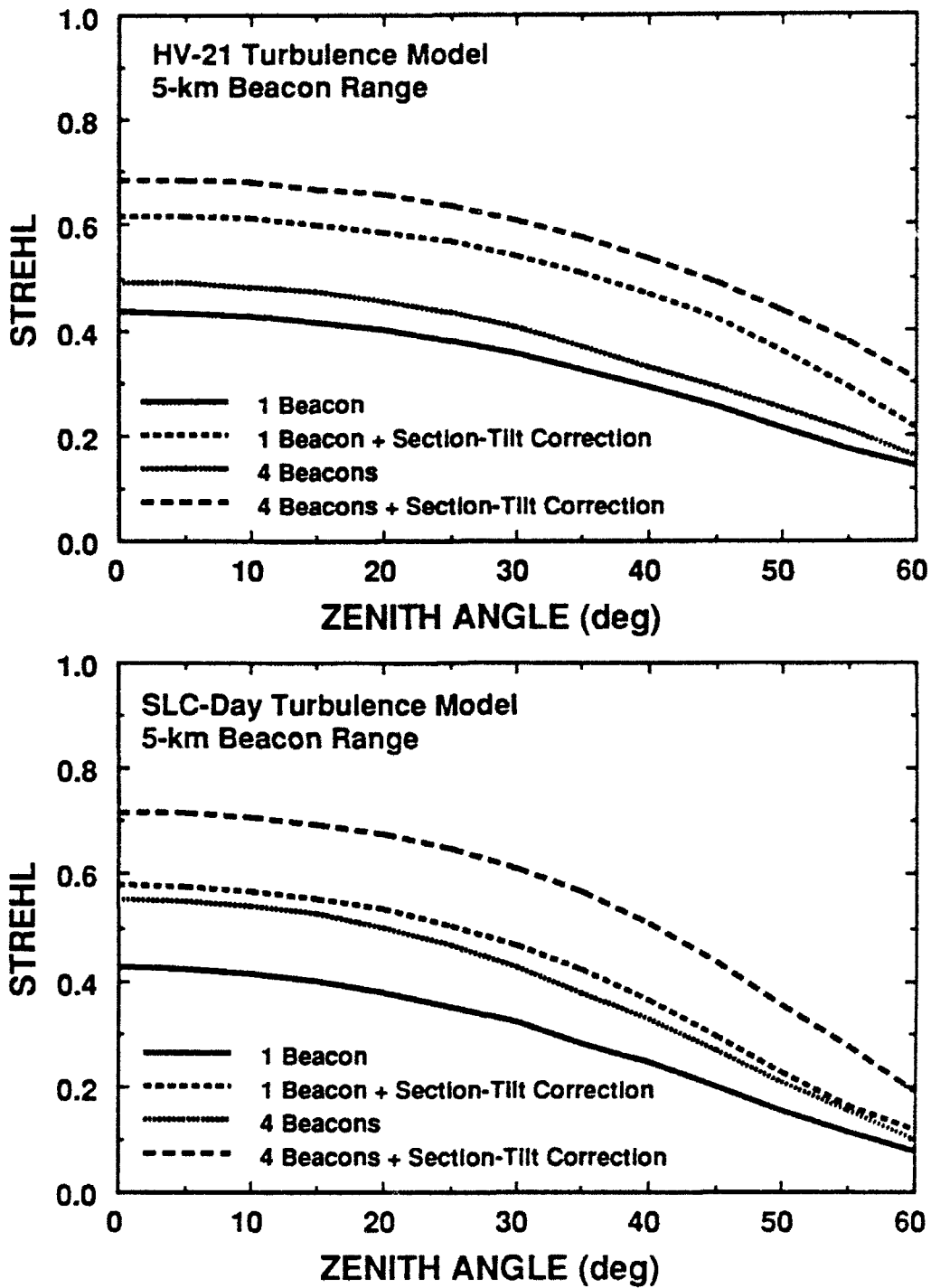


Figure 5-10. Comparison of far-field performance for the four major beacon geometries scheduled for test by the SWAT experimental system as a function of zenith angle. Quadrant tilt correction is derived from a single beacon at 90 km.

In addition to the Rayleigh and hybrid-beacon designs covered in this section, the SWAT program is also funding the construction of a 7-joule sodium-frequency laser based on the sum-frequency concept<sup>3</sup>, which could be used to generate a single source at 90 km. At this altitude, focal anisoplanatic effects become virtually negligible for a 60-cm aperture. Performance curves showing the zenith angle dependence for a 90-km source are given in Figure 5-11. It can be seen that Strehl ratios in excess of 80% are expected for angles as large as 45°.

It should be emphasized at this point that the most important output of the SWAT experiments will be a validation of the basic HAVE REACH concept and a verification that single-beacon Strehl ratios close to the predicted values can be consistently achieved. The exploration of a more general parameter space involving sources of varying size, configurations, and altitudes will require considerably more care in order to detect subtle differences in performance. It will, however, be important to demonstrate good correlation between experiment and theory for a wide range of synthetic-beacon constructs in order to allow performance extrapolations for apertures of larger dimensions to be made with high confidence.

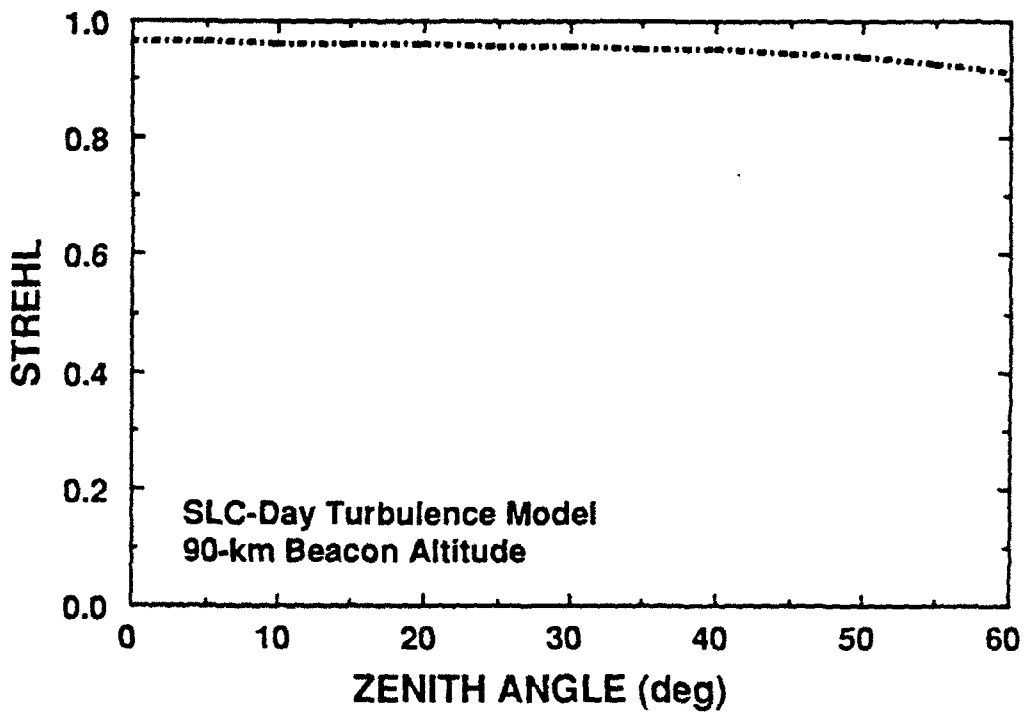
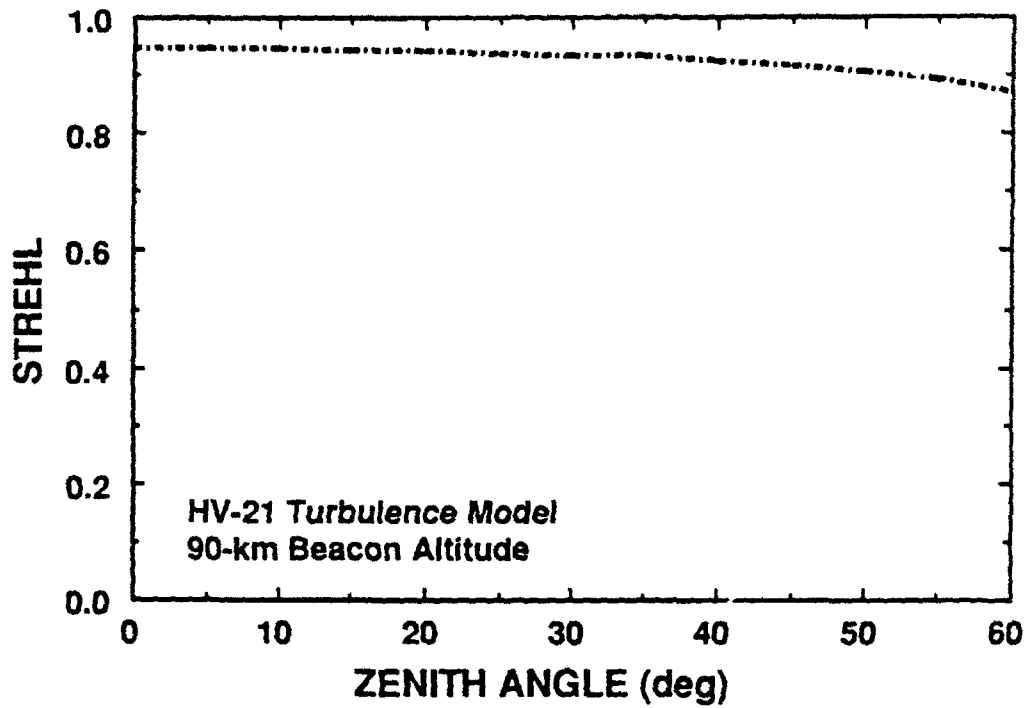


Figure 5-11. Far-field performance as a function of zenith angle for a single sodium beacon.

## 6. SUMMARY

As part of a comprehensive analysis effort in support of the SWAT experimental program, independent numerical and analytical techniques have been developed to provide estimates of system performance. With the aid of this software it is now possible to accurately predict both the near-field phase variance or far-field Strehl for a wide range of synthetic beacon geometries. Despite the dissimilarity of these two computational approaches, the agreement between the figure-variance estimates is extremely good for all of the scenarios studied.

In the system's baseline configuration, in which a single beacon is deployed at a range of 5 km, both the SLC-Day and HV-21 atmospheric models yield Strehl predictions in excess of 0.3. This number exceeds the uncorrected Strehl by nearly a factor of 100, and the measurement of an improvement of this magnitude would provide definitive proof of the efficacy of the synthetic-beacon concept.

The intent of the multiple-beacon stitching, hybrid-beacon, and sodium-beacon experiments is to test the scalability of these approaches to apertures of much larger diameter. Although a measurable Strehl improvement is of marginal probability for the first two of these constructs, the single-sodium experiments are likely to provide a clear verification of the benefits of high-altitude sampling.

## REFERENCES

1. R. R. Parenti, P. N. Everett, R. Kramer, and D. A. Page, "SWAT II Overview," Lincoln Laboratory Project Report SWP-3 (10 February 1988).
2. R. R. Parenti and D. V. Murphy, "SWAT II Laboratory Test Results," Lincoln Laboratory Project Report SWP-6 (16 January 1989).
3. T. H. Jeys, "Nd:YAG Sum-Frequency Generation of Sodium-Resonance Radiation," Lincoln Laboratory Project Report SWP-2 (4 August 1987).
4. J. Herrmann, "Least-Squares Wave Front Errors of Minimum Norm," J. Opt. Soc. Am., 70, 1, 28-35 (January 1980).
5. D. G. Luenberger, Optimization by Vector Space Methods, John Wiley & Sons, Inc. (1969).
6. D. P. Greenwood, "Adaptive Compensation for Atmospheric Turbulence Effects on Optical Propagation," 33rd Electromagnetic Wave Propagation Panel Meeting (4-7 October 1983).
7. R. J. Sasiela, "Unified Approach to Electromagnetic Wave Propagation in Turbulence and the Evaluation of Multiparameter Integrals," TR-807 July 1988.
8. I. S. Gradshteyn and I. M. Ryzhik, Table of Integrals, Series, and Products (Academic Press, New York, 1980).
9. R. E. Hufnagel, "Variations in Atmospheric Turbulence," Digest of Technical Papers, Topical Meeting on Optical Propagation Through Turbulence, (Optical Society of America, 1974).
10. G. C. Valley, Applied Optics, 19, 574, (1980).

## APPENDIX A

### FOCAL ANISOPLANATISM

#### A-1 THEORY

One can use Mellin transform techniques to calculate the phase variance of a beacon at a given altitude,  $H$ , with all the phase present using Equation (3.7.4) of Technical Report 807<sup>6</sup> which is

$$\sigma^2 = 0.5k_0^2 \mu_{5/3} \left( \frac{D}{H} \right)^{5/3} = \left( \frac{0.348D}{H\theta_0} \right)^{5/3} \quad (A-1)$$

Often one is interested in the phase variance with piston or piston and tilt removed. The phase variance due to piston and tilt can be calculated separately and subtracted from the total phase variance to obtain these variances. The filter functions to remove piston and tilt are given in Equations (3.4.20) and (3.4.23) and the remark at the bottom of page 102 of TR-807. The piston removal filter function for a beacon at a distance  $L$  is

$$F(\bar{\kappa}, z) = \left[ \frac{2J_1(\kappa D/2)}{\kappa D/2} - \frac{2J_1(\kappa D(1-z/L)/2)}{\kappa D(1-z/L)/2} \right]^2 \quad (A-2)$$

The filter function to remove the phase variance due to tilt is

$$F(\bar{\kappa}, z) = \left[ \frac{4J_2(\kappa D/2)}{\kappa D/2} - \frac{4J_2(\kappa D(1-z/L)/2)}{\kappa D(1-z/L)/2} \right]^2 \quad (A-3)$$

These must be inserted into the standard expression given below to find the variance

$$\sigma^2 = 0.2073k_0^2 \int_0^L dz C_n^2(z) \int d\bar{\kappa} f(\kappa) F_d(\bar{\kappa}, z) \quad (A-4)$$

To find the piston variance insert Equation (A-2) into (A-4), perform the angular integration, and obtain

$$\sigma_p^2 = 5.212k_0^2 \int_0^L dz C_n^2(z) \int_0^\infty d\kappa \kappa^{-8/3} \left[ \frac{J_1(\kappa D/2)}{\kappa D/2} - \frac{J_1(\kappa D(1-z/L)/2)}{\kappa D(1-z/L)/2} \right]^2 \quad (A-5)$$

Similarly, the tilt variance is

$$\sigma_t^2 = 20.85k_0^2 \int_0^L dz C_n^2(z) \int_0^\infty d\kappa \kappa^{-8/3} \left[ \frac{J_2(\kappa D/2)}{\kappa D/2} - \frac{J_2(\kappa D(1-z/L)/2)}{\kappa D(1-z/L)/2} \right]^2. \quad (\text{A-6})$$

Evaluating the integral in kappa space poses some difficulty. The two terms in brackets almost cancel especially for very high beacon altitudes. If the bracket is expanded, three terms result. Two of these terms can be evaluated by table lookup for the tilt case. For piston each of these terms is divergent. The term that is the product of the two terms must be evaluated using the Mellin convolution integral. To obtain sufficient accuracy a large number of terms in the resulting series expansion would have to be retained to get an accurate final answer for the tilt case. A more productive way to manipulate the integral uses the multiplication formula for Bessel functions given in Equation (8.535) from Gradshteyn and Ryzhik<sup>8</sup> which is.

$$Z_\nu(\lambda x) = \lambda^\nu \sum_{k=0}^{\infty} \frac{1}{k!} Z_{\nu+k}(x) \left[ \frac{1-\lambda^2}{2} x \right]^k \quad |1-\lambda^2| < 1. \quad (\text{A-7})$$

For this problem

$$\lambda = 1 - z/L, \quad (\text{A-8})$$

which is less than unity so that the inequality is satisfied. The first three terms of the expansion are

$$J_\nu(\lambda x) = \lambda^\nu \left[ J_\nu(x) + J_{\nu+1}(x) \frac{xz}{L} (1-z/2L) + \frac{J_{\nu+2}(x)}{2} \left\{ \frac{xz}{L} (1-z/2L) \right\}^2 \right]. \quad (\text{A-9})$$

The term in brackets to find the piston in Equation (A-5) becomes

$$\frac{J_1(x)}{x} - \frac{J_1(x[1-z/L])}{x(1-z/L)} = \frac{z}{L} \left[ J_2(x)(1-z/2L) - \frac{J_3(x)}{2} \left\{ \frac{xz}{L} (1-z/2L) \right\}^2 \right]. \quad (\text{A-10})$$

The terms that diverge exactly cancel in this approach. The term in brackets to find the tilt in Equation (A-6) is

$$\begin{aligned} & \frac{J_2(x)}{x} - \frac{J_2(x[1-z/L])}{x(1-z/L)} \\ &= \frac{z}{L} \left[ \frac{J_2(x)}{x} - J_3(x) \left\{ 1 - \frac{3z}{2L} + \frac{z^2}{2L^2} \right\} - \frac{J_4(x)}{2} \frac{xz}{L} \left( 1 - \frac{z}{L} \right) \left( 1 - \frac{z}{2L} \right)^2 \right]. \end{aligned} \quad (\text{A-11})$$

The entire first term does not cancel in this approach. The reason why there is exact cancellation of

the piston term and not the tilt term is that piston measured at any altitude adds up with the other piston contributions to get the total piston. The tilt measured at any altitude is magnified by the ratio of the diameters when it is added to the other tilts; therefore, there is not perfect cancellation of the tilt. The first term is by far the most significant for both piston and tilt. If these terms are put back into the variance expression and squared as required, the Mellin transforms can be performed to give the following approximation for the variances.

The piston variance is

$$\sigma_p^2 = D^{5/3} k_0^2 \left[ 0.0835 \frac{\mu_2}{L^2} + 0.01378 \frac{\mu_3}{L^3} + 0.00697 \frac{\mu_4}{L^4} - 0.0591 \frac{\mu_5}{L^5} + 0.045 \frac{\mu_6}{L^6} \right]. \quad (\text{A-12})$$

The tilt variance is

$$\sigma_t^2 = D^{5/3} k_0^2 \left[ 0.355 \frac{\mu_2}{L^2} - 0.484 \frac{\mu_3}{L^3} + 1.00 \frac{\mu_4}{L^4} - 0.543 \frac{\mu_5}{L^5} + 0.116 \frac{\mu_6}{L^6} \right]. \quad (\text{A-13})$$

The piston removed variance is

$$\sigma_{pr}^2 = \left( \frac{0.348D}{H\theta_o} \right)^{5/3} - \sigma_p^2. \quad (\text{A-14})$$

The piston and tilt removed variance is

$$\sigma_{ptr}^2 = \left( \frac{0.348D}{H\theta_o} \right)^{5/3} - \sigma_p^2 - \sigma_t^2. \quad (\text{A-15})$$

## A-2 SUMMARY

A simple way to compute the phase variance with focal anisoplanatism with and without the presence of piston and tilt has been provided. This is easily extended to remove other Zernike components. A Basic computer program has been written for the Macintosh that performs these calculations.

Using the above results, a good approximation to the piston removed phase is

$$\sigma_{pr}^2 = 0.5 D^{5/3} k_0^2 \left[ \frac{\mu_{5/3}}{L^{5/3}} - 0.17 \frac{\mu_2}{L^2} - 0.02756 \frac{\mu_3}{L^3} - 0.0139 \frac{\mu_4}{L^4} + 0.118 \frac{\mu_5}{L^5} - 0.09 \frac{\mu_6}{L^6} \right]. \quad (\text{A-16})$$

Similarly, a good approximation to the piston and tilt removed phase is

$$\sigma_{ptr}^2 = 0.5D^{5/3}k_0^2 \left[ \frac{\mu_{5/3}}{L^{5/3}} - 0.877 \frac{\mu_2}{L^2} + 0.94 \frac{\mu_3}{L^3} - 2.014 \frac{\mu_4}{L^4} + 1.204 \frac{\mu_5}{L^5} - 0.322 \frac{\mu_6}{L^6} \right]. \quad (\text{A-17})$$

## APPENDIX B FOCAL ANISOPLANATIC TILT

### B-1 INTRODUCTION

Consider two beacon sources at an altitude  $L$  with a separation  $b$  as shown in Figure B1. Let the position of each of these beacons be measured with a common aperture. The tilt difference measured between these two beacons will be equal to the real difference between these two beacons and, in addition, there will be a stochastic difference with zero mean that is due to the different paths that the two beacon rays take through the atmospheric turbulence. It is the two-axis rms stochastic tilt difference between these two point beacons that is calculated in this memorandum.

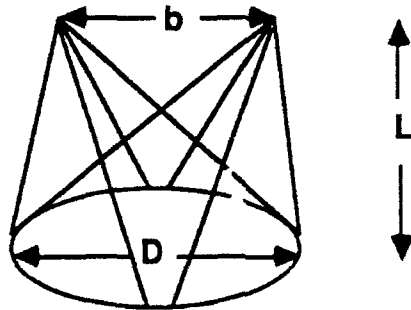


*Figure B1. Focal anisoplanatic geometry.*

### B-2 THEORY

The tilt difference between two infinite plane waves looking in different directions with infinite outer scale size has been treated in Section 3.6.2 and 3.6.3 of TR-807. This effect is referred to as tilt anisoplanatism. In this memorandum, rather than having infinite plane waves, one is dealing with focused waves. The only difference between this problem and the one that has been solved is that the tilt filter function must be the one appropriate for focused beams. The filter function is a product of the term for anisoplanatism and the one to extract tilt of a beam focused at  $L$ . The mean squared tilt variance can be written down as

$$T_Z^2 = 0.2073 k_0^2 \int_0^L dz C_n^2(z) \int d\vec{\kappa} \kappa^{-11/3} \left( \frac{16}{k_0 D} \right)^2 \left( \frac{J_2(\kappa D [1 - z/L] / 2)}{\kappa D [1 - z/L] / 2} \right)^2 2 [1 - \cos\{\vec{\kappa} \cdot \vec{d}(z)\}], \quad (\text{B-1})$$

where

$$\bar{d}(z) = \bar{b} \frac{z}{L} . \quad (\text{B-2})$$

The angular integration can be performed and if the substitutions

$$x = \kappa D [1 - z / L] / 2 , \quad (\text{B-3})$$

and

$$t = \frac{D}{2b} \frac{L}{z} (1 - z / L) \quad (\text{B-4})$$

are made, then the tilt variance is

$$T_Z^2 = \frac{210 \sec(\xi)^L}{D^{1/3}} \int_0^L dz C_n^2(z) (1 - z / L)^{5/3} \int_0^\infty \frac{dx}{x} x^{-11/3} J_2^2(x) [1 - J_0(x/t)] . \quad (\text{B-5})$$

In the last formula the zenith dependence was included. It was assumed that as the zenith angle changes the distance of the beacon to the transmitter changed to keep the beacon altitude constant. To get the zenith dependence with that assumption the substitutions  $z \rightarrow z \sec(\xi)$  and  $L \rightarrow L \sec(\xi)$  were made. For large values of  $t$  the last integral goes to zero. This occurs at low altitude because there is very little separation between the rays of the two beacons. There is a large separation between the rays close to the beacon but there is also very little contribution from this region because of the demagnification factor of the tilt. This is seen from the term on the right of the turbulence strength. The Mellin convolution integral can be used to convert the last integral into

$$I = -\frac{1}{2\sqrt{\pi}} \frac{1}{2\pi i} \int_C ds (2t)^{-2s} \Gamma \left[ \begin{matrix} s + \frac{1}{6}, -s + \frac{7}{3}, -s^* \\ -s + \frac{29}{6}, -s + \frac{17}{6}, s + 1 \end{matrix} \right] . \quad (\text{B-6})$$

Since  $\Delta = 0$ , the path of integration should be closed in the left-half plane for small values of the parameter and in the right half plane for large values. The parameter in the integral is large for low altitude and small for high altitudes; therefore, to get a rapidly converging series one wants one power series for high altitudes and the other power series for low altitudes. The power series has poles at  $s = 0$ , and  $s = -1/6 - n$  for  $n = 0, 1, 2, \dots$ . The parameter is equal to unity at an altitude of

$$z_t = \frac{L}{b/D + 1} . \quad (\text{B-7})$$

From the pole locations, the power series solution for high altitudes can be written as

$$I = \frac{1}{2\sqrt{\pi}} \left[ 0.2052 - \sum_{n=0}^{\infty} \frac{(-1)^n}{n!} (2t)^{2n+1/3} \Gamma \left[ \begin{matrix} n + \frac{5}{2}, n + \frac{1}{6} \\ n + 5, n + 3, -n + \frac{5}{6} \end{matrix} \right] \right]. \quad (\text{B-8})$$

The power series good for low altitudes is

$$2\sqrt{\pi}I = \left[ -\sum_{n=1}^{\infty} \frac{(-1)^n}{n!} (2t)^{2n} \Gamma \left[ \begin{matrix} n + \frac{1}{6}, -n + \frac{7}{3} \\ -n + \frac{29}{6}, -n + \frac{17}{6}, 1 + n \end{matrix} \right] - \sum_{n=0}^{\infty} \frac{(-1)^n}{n!} (2t)^{2n+14/3} \Gamma \left[ \begin{matrix} n + \frac{5}{2}, -n - \frac{7}{3} \\ -n + \frac{5}{2}, -n + \frac{1}{2}, n + \frac{10}{3} \end{matrix} \right] \right]. \quad (\text{B-9})$$

The transition altitude when one should change from one power series to the other is  $z_t$ , however, for good convergence with only a few terms use the second power series whenever  $z > z_t / 2$  and the first power series for lower altitudes. Substitute these results back into Equation (B-5). The first few terms of each solution give the tilt variance as

$$\begin{aligned} T_Z^2 = & \frac{10.68}{D^{1/3}} \int_0^{z_t/2} dz C_n^2(z) \left[ \left( \frac{bz}{DL} \right)^2 (1-z/L)^{-1/3} - 2.067 \left( \frac{bz}{DL} \right)^4 (1-z/L)^{-7/3} \right. \\ & \left. - 1.472 \left( \frac{bz}{DL} \right)^{14/3} (1-z/L)^{-3} + 0.339 \left( \frac{bz}{DL} \right)^6 (1-z/L)^{-13/3} \right] \\ & + \frac{12.16}{D^{1/3}} \int_{z_t/2}^L dz C_n^2(z) \left[ (1-z/L)^{5/3} - 0.6657 \left( \frac{DL}{bz} \right)^{1/3} (1-z/L)^2 - 0.00308 \left( \frac{DL}{bz} \right)^{7/3} (1-z/L)^4 \right. \\ & \left. - 3.06 \times 10^{-6} \left( \frac{DL}{bz} \right)^{13/3} (1-z/L)^6 - 6.15 \times 10^{-6} \left( \frac{DL}{bz} \right)^{19/3} (1-z/L)^8 \right]. \end{aligned} \quad (\text{B-10})$$

Therefore, to evaluate this expression for a particular beacon separation and height, aperture diameter, and turbulence model, one has to perform the numerical integration over the turbulence profile. A Basic program has been written to perform this calculation. As an example, for a beacon altitude of 100 km and separation of 0.3 m with a 0.6-m receiving aperture the tilt standard deviation is 42, 41, and 72 nanoradians for the SLC-Day, SLC-Night and HV-21 turbulence models.

### **B-3 SUMMARY**

Mellin transform techniques have been used to derive an expression for the variance of the tilt difference between two beacons that emanate from point sources at the same altitude and whose positions are measured by a common aperture. A computer program is available to perform this calculation.

## APPENDIX C

### CORRELATION FUNCTIONS OF TILT AND OF THE TILT AND PISTON COMPONENTS OF FOCAL ANISOPLANATISM

#### C-1 INTRODUCTION

Consider the tilt or piston difference between a collimated beam and a focused beam. In this memorandum the correlation function for these tilt and piston components is calculated first for the case in which the point source is directly over the aperture and then for the case in which the point source is displaced from the central location. The correlation function for tilt is a function of the direction of the displacement relative to the tilt component. Surprisingly, it is found that perpendicular components of tilt, which are uncorrelated in a given aperture, are correlated for apertures that are displaced in a skewed direction.

In focal anisoplanatism the major part of the tilt component comes about because the tilt measured at higher altitudes is sampled over a smaller area than the collimated beam and is demagnified as the beam expands. The result is that the tilt and the tilt component of focal anisoplanatism to first order have the same spatial statistics and subsequently the same correlation function.

#### C-2 CORRELATION FUNCTION FOR A CENTERED POINT SOURCE

For some problems it is necessary to compute the correlation function of the tilt and piston variance components of focal anisoplanatism. Using the filter function method it is relatively easy to calculate this correlation. The correlation function for the piston and tilt is defined to be

$$C_{p,t}(\vec{d}) = \frac{\sigma_{p,t}(\vec{r})\sigma_{p,t}(\vec{r} + \vec{d})}{\sigma_{p,t}^2(\vec{r})} = 1 - \frac{[\sigma_{p,t}(\vec{r}) - \sigma_{p,t}(\vec{r} + \vec{d})]^2}{2\sigma_{p,t}^2(\vec{r})} = 1 - \frac{N_{p,t}}{2\sigma_{p,t}^2(\vec{r})} \quad (C-1)$$

The denominators of the equations have been calculated in the appendix on focal anisoplanatism. The numerators can be calculated from the expressions in that memorandum by incorporating the anisoplanatic filter function. There are three correlation functions of the tilt that must be calculated. The numerator terms can be written as

$$N_p = \left[ \sigma_p(\vec{r}) - \sigma_p(\vec{r} + \vec{d}) \right]^2 = 1.659k_0^2 \int_0^L dz C_n^2(z) \int d\vec{\kappa} \kappa^{-11/3} \times \left[ \frac{J_1(\kappa D/2)}{\kappa D/2} - \frac{J_1(\kappa D(1-z/L)/2)}{\kappa D(1-z/L)/2} \right]^2 \left[ 1 - \cos(\vec{\kappa} \cdot \vec{d}) \right], \quad (C-2)$$

and for the  $a$  and  $b$  components of tilt it is

$$N_{iab} = \left[ \sigma_{ia}(\vec{r}) - \sigma_{ib}(\vec{r} + \vec{d}) \right]^2 = 3.318k_0^2 \int_0^L dz C_n^2(z) \int d\vec{\kappa} \kappa^{-11/3} \left| G_{ia} - G_{ib} \exp[j\vec{\kappa} \cdot \vec{d}] \right|^2. \quad (C-3)$$

where the complex filter function applies to that component of tilt. The correlation coefficient between the  $x$ -components of tilt is

$$N_{\alpha\alpha} = \left[ \sigma_{\alpha}(\vec{r}) - \sigma_{\alpha}(\vec{r} + \vec{d}) \right]^2 = 6.636k_0^2 \int_0^L dz C_n^2(z) \int d\vec{\kappa} \kappa^{-11/3} \times \left[ \frac{J_2(\kappa D/2)}{\kappa D/2} - \frac{J_2(\kappa D(1-z/L)/2)}{\kappa D(1-z/L)/2} \right]^2 \cos^2(\phi) \left[ 1 - \cos(\vec{\kappa} \cdot \vec{d}) \right]. \quad (C-4)$$

The correlation function of the  $x$ -tilt is the correlation of the  $x$ -tilt component with the  $x$ -tilt displaced in an arbitrary direction. The formula for the  $y$  component will be written by inspection after this derivation. A useful integral in the evaluation is

$$\int_0^{2\pi} d\theta \cos(\theta) \sin(\theta) \cos[\kappa d \cos(\theta)] = 2 \int_0^{\pi} d\theta \cos(\theta) \sin(\theta) \cos[\kappa d \cos(\theta)] = 0. \quad (C-5)$$

If the last integral is broken up into a part from 0 to  $\pi/2$  and from  $\pi/2$  to  $\pi$ , and the substitution  $\theta = \theta - \pi$  is made in the second, the two parts cancel. If the angle between the displacement and the  $x$ -axis is  $\theta'$ , the angular integration can be expanded using the trigonometric identity

$$\cos(a+b) = \cos(a)\cos(b) - \sin(a)\sin(b), \quad (C-6)$$

to give

$$\begin{aligned}
& \int_0^{2\pi} d\phi \cos^2(\phi) \{1 - \cos[\kappa d \cos(\phi + \theta_i)]\} = \int_0^{2\pi} d\phi \cos^2(\phi - \theta_i) \{1 - \cos[\kappa d \cos(\phi)]\} \\
& = \int_0^{2\pi} d\phi [\cos^2(\theta_i) \cos^2(\phi) + \sin^2(\theta_i) \sin^2(\phi) - 2 \cos(\theta_i) \cos(\phi) \sin(\theta_i) \sin(\phi)] \\
& \quad \times \{1 - \cos[\kappa d \cos(\phi)]\}. \tag{C-7}
\end{aligned}$$

The integral of the last term in brackets is zero since it is the same integral as in Equation (C-5). The angular integration of the second term can be performed using Equation (3.915 #5) from Gradshteyn and Ryzhik which is

$$\int_0^{\pi} \exp[i\beta \cos(x)] \sin^{2\nu}(x) dx = \sqrt{\pi} \left(\frac{2}{\beta}\right)^{\nu} \Gamma\left[\nu + \frac{1}{2}\right] J_{\nu}(\beta); \quad \text{Re } \nu > -\frac{1}{2} \tag{C-8}$$

Use the trigonometric identity

$$\cos^2(\varphi) = 1 - \sin^2(\varphi) \tag{C-9}$$

to express the first term in the form of Equation (C-7) which integrals can then be performed to give

$$\begin{aligned}
N_{\text{ax}} &= 41.7k_0^2 \int_0^L dz C_n^2(z) \int_0^{\infty} d\kappa \kappa^{-8/3} \left[ \frac{J_2(\kappa D/2)}{\kappa D/2} - \frac{J_2(\kappa D(1-z/L)/2)}{\kappa D(1-z/L)/2} \right]^2 \\
& \quad [\sin^2(\theta_i) [1/2 - J_1(\kappa d)/\kappa d] + \cos^2(\theta_i) \{[1 - J_0(\kappa d)] - [1/2 - J_1(\kappa d)/\kappa d]\}]. \tag{C-10}
\end{aligned}$$

The first term of the expansions of the Bessel function contained in the brackets in Equations (C-2) and (C-10) is the dominant term. With this single term approximation, which is evaluated using Equations (A-10) and (A-11), the numerator terms can be written as

$$N_p = 10.42k_0^2 \int_0^L dz C_n^2(z) \frac{z^2}{L^2} \int_0^{\infty} d\kappa \kappa^{-8/3} J_2^2(\kappa D/2) [1 - J_0(\kappa d)], \tag{C-11}$$

and for the tilt, the axial integration can be performed to give

$$\begin{aligned}
N_{xx'} &= 41.7k_0^2 \left(\frac{D}{2}\right)^{5/3} \frac{\mu_2}{L^2} \left[ \sin^2(\theta_i) I_1 + \cos^2(\theta_i) \{I_T - I_1\} \right] \\
&= 41.7k_0^2 \left(\frac{D}{2}\right)^{5/3} \frac{\mu_2}{L^2} \left[ I_T \cos^2(\theta_i) - I_1 \cos(2\theta_i) \right], \tag{C-12}
\end{aligned}$$

where

$$\begin{bmatrix} I_T \\ I_1 \end{bmatrix} = \left(\frac{2}{D}\right)^{5/3} \int_0^\infty d\kappa \kappa^{-8/3} J_2^2(\kappa D/2) \begin{bmatrix} 1 - J_0(\kappa d) \\ 1/2 - J_1(\kappa d)/\kappa d \end{bmatrix}. \tag{C-13}$$

The y-tilt correlation coefficient is found by rotating the above result by 90 degrees to get

$$N_{yy'} = 41.7k_0^2 \left(\frac{D}{2}\right)^{5/3} \frac{\mu_2}{L^2} \left[ \sin^2(\theta_i - \pi/2) I_1 + \cos^2(\theta_i - \pi/2) \{I_T - I_1\} \right]. \tag{C-14}$$

For pure tilt the expression above has the second moment divided by the source distance squared replaced by the zeroth moment. When the correlation function is calculated, this term is cancelled by the denominator term; therefore, in this approximation where only the first term of the expansion of the difference of Bessel functions is used, the correlation functions of tilt focal anisoplanatism and tilt are the same.

The correlation coefficient of the perpendicular components of tilt will now be found. Use Equation (C-3) to get

$$\begin{aligned}
N_{xy'} &= \left[ \sigma_{ix}(\vec{r}) - \sigma_{iy}(\vec{r} + \vec{d}) \right]^2 = 3.318k_0^2 \int_0^L dz C_n^2(z) \int d\vec{\kappa} \kappa^{-11/3} \\
&\quad \times \left[ \frac{J_2(\kappa D/2)}{\kappa D/2} - \frac{J_2(\kappa D(1-z/L)/2)}{\kappa D(1-z/L)/2} \right]^2 \left| \cos(\phi) - \sin(\phi) \exp[j\vec{\kappa} \cdot \vec{d}] \right|^2. \tag{C-15}
\end{aligned}$$

This can be simplified to give

$$\begin{aligned}
N_{xy'} &= 3.318k_0^2 \int_0^L dz C_n^2(z) \int d\vec{\kappa} \kappa^{-11/3} \\
&\quad \times \left[ \frac{J_2(\kappa D/2)}{\kappa D/2} - \frac{J_2(\kappa D(1-z/L)/2)}{\kappa D(1-z/L)/2} \right]^2 \left[ 1 - 2\sin(\phi)\cos(\phi)\cos(\vec{\kappa} \cdot \vec{d}) \right]. \tag{C-16}
\end{aligned}$$

The integral of the last term over angle is

$$I = \int_0^{2\pi} d\phi \sin(\phi) \cos(\phi) \cos[\kappa d \cos(\phi - \theta')] . \quad (\text{C-17})$$

Let  $\phi - \theta' = \theta$ , then using the trigonometric identities for the sum of angles one obtains

$$\begin{aligned} I &= \int_0^{2\pi} d\theta \sin(\theta + \theta') \cos(\theta + \theta') \cos[\kappa d \cos(\theta)] \\ &= \int_0^{2\pi} d\theta \cos[\kappa d \cos(\theta)] \left\{ \sin(\theta') \cos(\theta') [1 - 2\sin^2(\theta)] + \sin(\theta) \cos(\theta) [\cos^2(\theta') - \sin^2(\theta')] \right\} . \end{aligned} \quad (\text{C-18})$$

Using Equation (C-5) one sees that the last term in braces integrates to zero giving

$$I = 2 \sin(\theta') \cos(\theta') \int_0^{\pi} d\theta [1 - 2\sin^2(\theta)] \cos[\kappa d \cos(\theta)] . \quad (\text{C-19})$$

Using Equation (C-7) twice and inserting this into Equation (C-15) one obtains

$$\begin{aligned} N_{xy'} &= 20.85 k_0^2 \int_0^L dz C_n^2(z) \int_0^{\infty} d\kappa \kappa^{-8/3} \left[ \frac{J_2(\kappa D/2)}{\kappa D/2} - \frac{J_2(\kappa D(1-z/L)/2)}{\kappa D(1-z/L)/2} \right]^2 \\ &\times \left\{ 1 - 2 \sin(\theta') \cos(\theta') [J_0(\kappa d) - 2J_1(\kappa d) / \kappa d] \right\} . \end{aligned} \quad (\text{C-20})$$

The correlation term which is the last term in braces is not always zero. It is zero if the displacement is along the  $x$  or  $y$  axis or if the wavenumber is zero or infinitely large. Again, using only the first term of the expansion for the expression in brackets one obtains

$$N_{xy'} = 20.85 k_0^2 \frac{\mu_2}{L^2} \left( \frac{D}{2} \right)^{5/3} \left[ 0.0579 + \sin(2\theta') (2I_1 - I_T) \right] . \quad (\text{C-21})$$

### C-3 EVALUATION OF CORRELATION COEFFICIENTS

The expressions developed in the last section will now be evaluated using Mellin transform techniques. Let  $\alpha = \kappa D/2$  and  $\beta = D/2d$ , Equation (C-11) and (C-13) become

$$\begin{aligned}
N_p &= 3.282 D^{5/3} k_0^2 \int_0^L dz C_n^2(z) \frac{z^2}{L^2} (1-z/2L)^2 \int_0^\infty \frac{d\alpha}{\alpha} \alpha^{-5/3} J_2^2(\alpha) [1 - J_0(\alpha/\beta)] \\
&= 3.282 D^{5/3} k_0^2 \int_0^L dz C_n^2(z) \frac{z^2}{L^2} (1-z/2L)^2 I_p,
\end{aligned} \tag{C-22}$$

and

$$\begin{bmatrix} I_T \\ I_1 \end{bmatrix} = \int_0^\infty \frac{d\alpha}{\alpha} \alpha^{-11/3} J_2^2(\alpha) \begin{bmatrix} 1 - J_0(\alpha/\beta) \\ 1/2 - J_1(\alpha/\beta)\beta/\alpha \end{bmatrix}. \tag{C-23}$$

Using the Mellin convolution integral, the integrals over  $\alpha$  can be written as

$$I_p = -\frac{1}{2\sqrt{\pi}} \frac{1}{2\pi i} \int_C ds \left(\frac{D}{d}\right)^{-2s} \Gamma \left[ \begin{matrix} s + \frac{7}{6}, -s + \frac{4}{3}, -s^* \\ -s + \frac{23}{6}, -s + \frac{11}{6}, s+1 \end{matrix} \right]. \tag{C-24}$$

For the first component of tilt

$$I_T = -\frac{1}{2\sqrt{\pi}} \frac{1}{2\pi i} \int_C ds \left(\frac{D}{d}\right)^{-2s} \Gamma \left[ \begin{matrix} s + \frac{1}{6}, -s + \frac{7}{3}, -s^* \\ -s + \frac{29}{6}, -s + \frac{17}{6}, s+1 \end{matrix} \right]. \tag{C-25}$$

For the second component of tilt

$$I_1 = -\frac{1}{4\sqrt{\pi}} \frac{D}{d} \frac{1}{2\pi i} \int_C ds \left(\frac{D}{d}\right)^{-2s} \Gamma \left[ \begin{matrix} s - \frac{1}{3}, -s + \frac{17}{6}, -s + \frac{1}{2}^* \\ -s + \frac{16}{3}, -s + \frac{10}{3}, s + \frac{3}{2} \end{matrix} \right]. \tag{C-26}$$

Since  $\Delta = 0$ , the direction of path closure is determined by the size of the parameter in the integral. That parameter can be less than or greater than unity which requires the solution for both ways of closing the integration path. If  $d > D$ , the path of integration is closed in the left-half plane, and there are poles at  $s = 0$  and at  $s = -7/6 - n$  for  $n = 0, 1, 2 \dots$  for the piston integral, and at  $s = 0$  and at  $s = -1/6 - n$  for  $n = 0, 1, 2 \dots$  for the first tilt integral and at  $s = 1/2$  and at  $s = -1/3 - n$  for  $n = 0, 1, 2 \dots$  for the second tilt integral. If  $d < D$ , the path of integration is closed in the right-half plane and there are poles at  $s = n$  for  $n = 1, 2, 3 \dots$  and at  $s = 4/3 + n$  for  $n = 0, 1, 2 \dots$  for the piston integral and at  $s = n$  for  $n = 1, 2, 3 \dots$  and at  $s = 7/3 + n$  for  $n = 0, 1, 2 \dots$  for the first tilt integral and at  $s = 1/2 + n$  for  $n = 1, 2, 3 \dots$  and at  $s = 17/6 + n$  for  $n = 0, 1, 2 \dots$  for the second tilt integral. Therefore, the piston integral is equal to

$$2\sqrt{\pi}I_p = 0.1802 - \sum_{n=0}^{\infty} \frac{(-1)^n}{n!} \Gamma \left[ \begin{matrix} n + \frac{5}{2}, n + \frac{7}{6} \\ n + 5, n + 3, -n - \frac{1}{6} \end{matrix} \right] \left( \frac{D}{d} \right)^{2n+1/3}; \quad d > D, \quad (\text{C-27})$$

and

$$2\sqrt{\pi}I_p = - \sum_{n=1}^{\infty} \frac{(-1)^{n+1}}{n!} \Gamma \left[ \begin{matrix} n + \frac{7}{6}, -n + \frac{4}{3} \\ -n + \frac{23}{6}, -n + \frac{11}{6}, n + 1 \end{matrix} \right] \left( \frac{d}{D} \right)^{2n} \\ - \sum_{n=0}^{\infty} \frac{(-1)^n}{n!} \Gamma \left[ \begin{matrix} n + \frac{5}{2}, -n - \frac{4}{3} \\ -n + \frac{5}{2}, -n + \frac{1}{2}, n + \frac{7}{3} \end{matrix} \right] \left( \frac{d}{D} \right)^{2n+8/3}; \quad d < D. \quad (\text{C-28})$$

Using this in Equation (C-22), one finds

$$N_p = 0.17k_0^2 D^{5/3} \left( \frac{\mu_2}{L^2} - \frac{\mu_3}{L^3} + \frac{\mu_4}{4L^4} \right) \\ \times \left\{ 1 - 5.549 \sum_{n=0}^{\infty} \frac{(-1)^n}{n!} \Gamma \left[ \begin{matrix} n + \frac{5}{2}, n + \frac{7}{6} \\ n + 5, n + 3, -n - \frac{1}{6} \end{matrix} \right] \left( \frac{D}{d} \right)^{2n+1/3} \right\}; \quad d > D, \quad (\text{C-29})$$

and

$$N_p = 0.17k_0^2 D^{5/3} \left( \frac{\mu_2}{L^2} - \frac{\mu_3}{L^3} + \frac{\mu_4}{4L^4} \right) 5.549 \left\{ - \sum_{n=1}^{\infty} \frac{(-1)^{n+1}}{n!} \Gamma \left[ \begin{matrix} n + \frac{7}{6}, -n + \frac{4}{3} \\ -n + \frac{23}{6}, -n + \frac{11}{6}, n + 1 \end{matrix} \right] \left( \frac{d}{D} \right)^{2n} \right. \\ \left. - \sum_{n=0}^{\infty} \frac{(-1)^n}{n!} \Gamma \left[ \begin{matrix} n + \frac{5}{2}, -n - \frac{4}{3} \\ -n + \frac{5}{2}, -n + \frac{1}{2}, n + \frac{7}{3} \end{matrix} \right] \left( \frac{d}{D} \right)^{2n+8/3} \right\}; \quad d < D. \quad (\text{C-30})$$

The piston variance is found by using the first term of Equation (A-10) in (A-5) to give

$$\sigma_p^2 = 0.0835k_0^2 D^{5/3} \left( \frac{\mu_2}{L^2} - \frac{\mu_3}{L^3} + \frac{\mu_4}{4L^4} \right). \quad (\text{C-31})$$

The piston correlation function can then be written as

$$C_p(d) = 5.549 \sum_{n=0}^{\infty} \frac{(-1)^n}{n!} \Gamma \left[ \begin{matrix} n + \frac{5}{2}, n + \frac{7}{6} \\ n + 5, n + 3, -n - \frac{1}{6} \end{matrix} \right] \left( \frac{D}{d} \right)^{2n+1/3}; \quad d > D, \quad (\text{C-32})$$

and

$$C_p(d) = 1 - 5.549 \sum_{n=1}^{\infty} \frac{(-1)^{n+1}}{n!} \Gamma \left[ \begin{matrix} n + \frac{7}{6}, -n + \frac{4}{3} \\ -n + \frac{23}{6}, -n + \frac{11}{6}, n + 1 \end{matrix} \right] \left( \frac{d}{D} \right)^{2n} \\ - 5.549 \sum_{n=0}^{\infty} \frac{(-1)^n}{n!} \Gamma \left[ \begin{matrix} n + \frac{5}{2}, -n - \frac{4}{3} \\ -n + \frac{5}{2}, -n + \frac{1}{2}, n + \frac{7}{3} \end{matrix} \right] \left( \frac{d}{D} \right)^{2n+8/3}; \quad d < D. \quad (C-33)$$

The piston is the difference between the piston of the parallel and focused beams. Both beams sample the piston correctly and one expects that there will be very little correlation when the apertures move far enough apart that they are no longer touching. The plot in Figure C-1 indicates that this is the case. The correlation function essentially drops to zero at that separation.

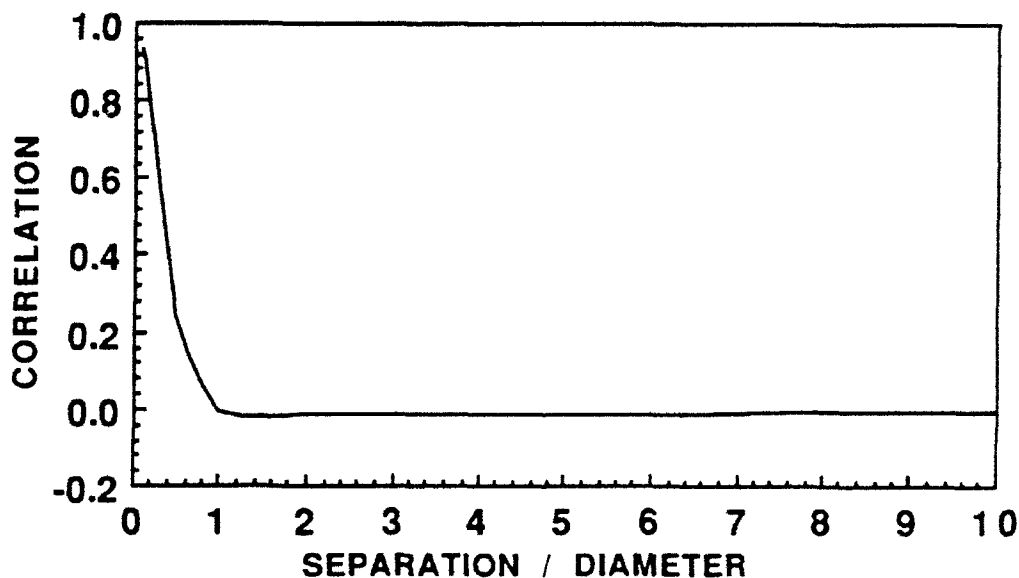


Figure C-1. Correlation function for the piston component of focal anisoplanatism.

For the first component of tilt, the integral is equal to

$$2\sqrt{\pi}I_T = 0.2052 - \sum_{n=0}^{\infty} \frac{(-1)^n}{n!} \Gamma \left[ \begin{matrix} n + \frac{5}{2}, n + \frac{1}{6} \\ n + 5, n + 3, -n + \frac{5}{6} \end{matrix} \right] \left( \frac{D}{d} \right)^{2n+1/3}; \quad d > D, \quad (\text{C-34})$$

and

$$\begin{aligned} 2\sqrt{\pi}I_T = & - \sum_{n=0}^{\infty} \frac{(-1)^n}{n!} \Gamma \left[ \begin{matrix} n + \frac{5}{2}, -n - \frac{7}{3} \\ -n + \frac{5}{2}, -n + \frac{1}{2}, n + \frac{10}{3} \end{matrix} \right] \left( \frac{d}{D} \right)^{2n+14/3} + \\ & - \sum_{n=1}^{\infty} \frac{(-1)^n}{n!} \Gamma \left[ \begin{matrix} n + \frac{1}{6}, -n + \frac{7}{3} \\ -n + \frac{29}{6}, -n + \frac{17}{6}, n + 1 \end{matrix} \right] \left( \frac{d}{D} \right)^{2n}; \quad d < D. \quad (\text{C-35}) \end{aligned}$$

For the second component of tilt, the integral is equal to

$$4\sqrt{\pi}I_1 = 0.2052 - \sum_{n=0}^{\infty} \frac{(-1)^n}{n!} \Gamma \left[ \begin{matrix} n + \frac{5}{2}, n + \frac{1}{6} \\ n + 5, n + 3, -n + \frac{11}{6} \end{matrix} \right] \left( \frac{D}{d} \right)^{2n+1/3}; \quad d > D, \quad (\text{C-36})$$

and

$$\begin{aligned} 4\sqrt{\pi}I_1 = & - \sum_{n=0}^{\infty} \frac{(-1)^n}{n!} \Gamma \left[ \begin{matrix} n + \frac{5}{2}, -n - \frac{7}{3} \\ -n + \frac{5}{2}, -n + \frac{1}{2}, n + \frac{13}{3} \end{matrix} \right] \left( \frac{d}{D} \right)^{2n+14/3} + \\ & - \sum_{n=1}^{\infty} \frac{(-1)^n}{n!} \Gamma \left[ \begin{matrix} n + \frac{1}{6}, -n + \frac{7}{3} \\ -n + \frac{29}{6}, -n + \frac{17}{6}, n + 2 \end{matrix} \right] \left( \frac{d}{D} \right)^{2n}; \quad d < D. \quad (\text{C-37}) \end{aligned}$$

The single axis tilt variance can be found by using the first term of Equation (A-11) in (A-6) and dividing by two, to obtain

$$\sigma_T^2 = 0.190k_0^2 D^{5/3} \frac{\mu_2}{L^2}. \quad (\text{C-38})$$

The tilt correlation function can then be written as

$$\begin{aligned}
C_{t_{xx}}(d) = & -4.873 \cos(2\theta_i) \sum_{n=0}^{\infty} \frac{(-1)^n}{n!} \Gamma \left[ \begin{matrix} n + \frac{5}{2}, n + \frac{1}{6} \\ n + 5, n + 3, -n + \frac{11}{6} \end{matrix} \right] \left( \frac{D}{d} \right)^{2n+1/3} \\
& + 9.746 \cos^2(\theta_i) \sum_{n=0}^{\infty} \frac{(-1)^n}{n!} \Gamma \left[ \begin{matrix} n + \frac{5}{2}, n + \frac{1}{6} \\ n + 5, n + 3, -n + \frac{5}{6} \end{matrix} \right] \left( \frac{D}{d} \right)^{2n+1/3}; \quad d > D, \quad (C-39)
\end{aligned}$$

and

$$\begin{aligned}
C_{t_{xx}}(d) = & 1 - 4.873 \cos(2\theta_i) \left\{ \sum_{n=0}^{\infty} \frac{(-1)^n}{n!} \Gamma \left[ \begin{matrix} n + \frac{5}{2}, -n - \frac{7}{3} \\ -n + \frac{5}{2}, -n + \frac{1}{2}, n + \frac{13}{3} \end{matrix} \right] \left( \frac{d}{D} \right)^{2n+14/3} + \right. \\
& \left. + \sum_{n=1}^{\infty} \frac{(-1)^n}{n!} \Gamma \left[ \begin{matrix} n + \frac{1}{6}, -n + \frac{7}{3} \\ -n + \frac{29}{6}, -n + \frac{17}{6}, n + 2 \end{matrix} \right] \left( \frac{d}{D} \right)^{2n} \right\} \\
& - 9.746 \cos^2(\theta_i) \left\{ \sum_{n=0}^{\infty} \frac{(-1)^n}{n!} \Gamma \left[ \begin{matrix} n + \frac{5}{2}, -n - \frac{7}{3} \\ -n + \frac{5}{2}, -n + \frac{1}{2}, n + \frac{10}{3} \end{matrix} \right] \left( \frac{d}{D} \right)^{2n+14/3} + \right. \\
& \left. + \sum_{n=1}^{\infty} \frac{(-1)^n}{n!} \Gamma \left[ \begin{matrix} n + \frac{1}{6}, -n + \frac{7}{3} \\ -n + \frac{29}{6}, -n + \frac{17}{6}, n + 1 \end{matrix} \right] \left( \frac{d}{D} \right)^{2n} \right\}; \quad d < D. \quad (C-40)
\end{aligned}$$

The correlation function is independent of the turbulence distribution. The tilt correlation functions for parallel, perpendicular and 45 degree displacement are plotted in Figure C-2. Observe that the correlation function is significant even for large separations. Using the relations in Equations (C-21) and (C-28) in (C-1), one obtains

$$C_{t_{xy}}(d) = 17.28 \sin(2\theta_i) (I_T - 2I_1). \quad (C-41)$$

If the values of  $I_T$  and  $I_1$  are inserted into the equation above, the correlation functions of the perpendicular components of tilt are equal to

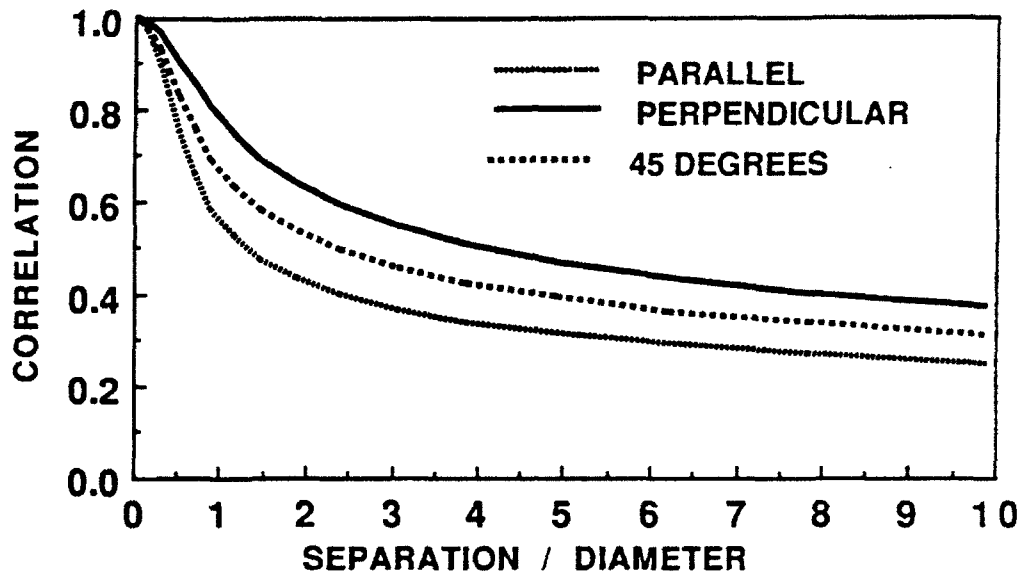


Figure C-2. Correlation function for tilt.

$$C_{txy}(d) = 4.873 \sin(2\theta_i) \sum_{n=0}^{\infty} \frac{(-1)^n}{n!} \Gamma \left[ \begin{matrix} n + \frac{5}{2}, n + \frac{7}{6} \\ n + 5, n + 3, -n + \frac{11}{6} \end{matrix} \right] \left( \frac{D}{d} \right)^{2n+1/3}; \quad d > D, \quad (C-42)$$

and

$$C_{txy}(d) = 4.873 \sin(2\theta_i) \left\{ \sum_{n=0}^{\infty} \frac{(-1)^n}{n!} \Gamma \left[ \begin{matrix} n + \frac{5}{2}, -n - \frac{4}{3} \\ -n + \frac{5}{2}, -n + \frac{1}{2}, n + \frac{13}{3} \end{matrix} \right] \left( \frac{d}{D} \right)^{2n+14/3} + \right. \\ \left. - \sum_{n=1}^{\infty} \frac{(-1)^n}{(n-1)!} \Gamma \left[ \begin{matrix} n + \frac{1}{6}, -n + \frac{7}{3} \\ -n + \frac{29}{6}, -n + \frac{17}{6}, n + 2 \end{matrix} \right] \left( \frac{d}{D} \right)^{2n} \right\}; \quad d < D. \quad (C-43)$$

If the displacement is parallel to one of the tilts the correlation is zero. For a displacement of 45 degrees to the tilts the correlation is plotted in Figure C-3. There is not as much correlation as that between parallel components of tilt.

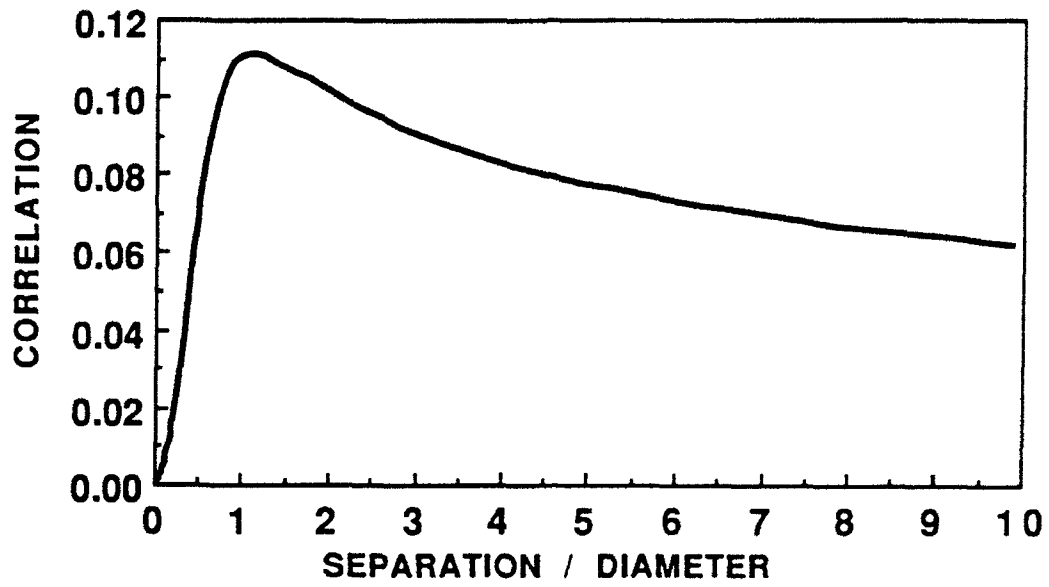


*Figure C-3. Correlation function of perpendicular components of tilt with the displacement 45 degrees to the tilt.*

## APPENDIX D FAR-FIELD IMAGE ANALYSIS

The processing methods used to extract estimates of Strehl from far-field imagery are typically reviewed at the beginning of each new field exercise, and the SWAT experiments have been no exception. Over the years a wide variety of approaches have been developed to deal with this problem, all of which display a fairly high susceptibility to data normalization errors. Following a careful preliminary analysis of the data obtained during the SWAT laboratory exercise, a new approach has been devised that appears to be somewhat better suited to this task. The process comprises two distinct stages: during the first step the raw data are carefully corrected to remove fixed-pattern noise and stray light effects; in the second step an estimate of the peak irradiance value is obtained from an energy distribution function. The essential elements of this process are outlined below.

The high-resolution CCD cameras used in the SWAT program can provide two-dimensional beam images of extremely high quality. The raw output data  $Z(x,y)$  can be modeled as follows

$$Z(x, y) = \tau_d \tau_o d^2 g(x, y) E(x, y) + Z_b(x, y) , \quad (D-1)$$

where  $E$  and  $Z$  represent the input optical irradiance and the electrical output signals respectively,  $\tau_d$  is the camera dwell time,  $\tau_o$  is the optical throughput,  $d$  is the pixel dimension,  $g$  is the camera gain, and  $Z_b$  is the fixed-pattern background. The background is normally assumed to be spatially varying but temporally static so that the  $Z_b$  term can be eliminated by subtracting camera frames taken with the input light blocked. It is further assumed that the gain is independent of pixel location but that it, and the system throughput, cannot be accurately measured. Therefore, the optical irradiance function at the camera focal plane bears the following relationship to the output data

$$E(x, y) = (1 / \gamma) [Z(x, y) - Z_b(x, y)] \quad (D-2)$$

where  $\gamma$  is indeterminate. Therefore, a direct radiometric determination of the Strehl ratio is precluded but a reasonably accurate estimate can be obtained if the diffraction-limited beam profile for the collection aperture can be computed. In general, a parameter having the form

$$\frac{Z(x, y) - Z_b(x, y)}{\sum_x \sum_y [Z(x, y) - Z_b(x, y)]}$$

will be generated at some point in the process, which eliminates the  $\gamma$  term. This energy

normalization is less straightforward than it appears, owing to the difficulty of simultaneously achieving high spatial resolution across the beam while obtaining an accurate measure of the total flux. Separate narrow and wide field-of-view detectors can be used for this purpose, but care must be taken to establish an accurate mutual calibration of the two sensors.

#### D-1 BASELINE CORRECTION

Failure to properly subtract the fixed-pattern background noise is the greatest potential source of error in the Strehl calculation, since a baseline offset on the order of 0.1% of the peak pixel intensity can translate into a 10% error in the estimate of the total beam energy. An offset error will occur when the ambient lighting changes between the data and background frames or when the camera is exposed to signal light scattered from optical elements within its field of view.

Recall that the  $Z - Z_b$  operation is intended to produce a data field that is free from fixed-pattern errors. Assuming that the focused beam subtends only a small fraction of the total detector array area, a histogram of  $Z - Z_b$  should display a Gaussian peak centered at zero. Any displacement of this peak from the null position, as illustrated in Figure D-1, is evidence of a baseline offset that should be corrected.

Baseline compensation entails the formation of the quantity

$$I(x,y) \equiv Z(x,y) - Z_b(x,y) - Z_o ,$$

where  $Z_o$  is the computed mean of the baseline peak of the  $Z - Z_b$  irradiance histogram. While the absolute value of  $Z_o$  is typically small, the Strehl measurement error is proportional to the product of  $Z_o$ , and the number of pixels in the detector array. The implementation of this simple procedure has significantly improved the frame-to-frame uniformity of the Strehl computations performed on the SWAT laboratory data.

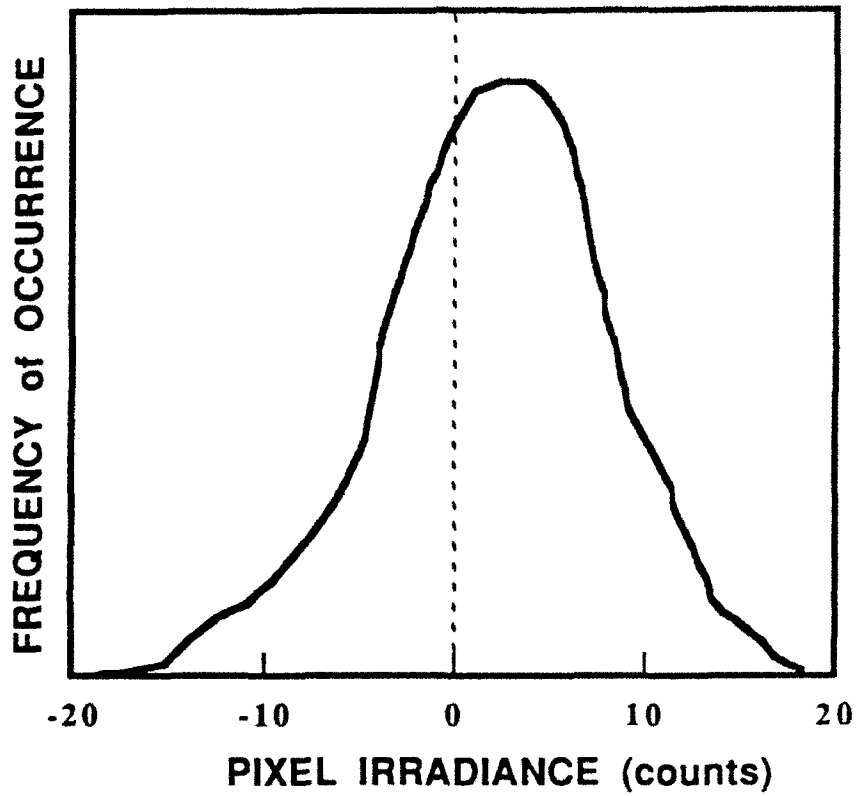


*Figure D-1. Typical histogram plot of uncorrected irradiance at null.*

## D-2 PEAK IRRADIANCE ESTIMATION

For a uniformly illuminated circular aperture, the diffraction-limited beam profile is specified by the airy irradiance function

$$E_{\text{Airy}}(r) = Q \left( \frac{(kD/2f)^2}{4\pi} \right) \left[ 2 \frac{J_1(kDr/2f)}{kDr/2f} \right]^2, \quad (\text{D-3})$$

where  $D$  is the aperture diameter,  $f$  is the focal length of the telescope, and  $Q$  is the pulse energy. It will be convenient to approximate this function by the Gaussian

$$E_{\text{Gauss}}(r) \approx Q \left( \frac{(kD/2f)^2}{4\pi} \right) \exp \left[ -\frac{1}{2} \left( \frac{(kD/2f)^2}{2} \right) r^2 \right] = \frac{Q}{2\pi\sigma_o^2} \exp \left[ -\frac{1}{2} \left( \frac{r^2}{\sigma_o^2} \right) \right], \quad (\text{D-4})$$

where  $\sigma_o^2 = 2 \left( \frac{2f}{kD} \right)^2$  defines the Gaussian beam width.

The beam profile of an aberrated beam might be modeled in the following way

$$E(r) = \frac{QS}{2\pi\sigma_o^2} \exp \left[ -\frac{1}{2} \left( \frac{r^2}{\sigma^2} \right) \right], \quad (\text{D-5})$$

where  $S$  is the peak irradiance (the usual definition of Strehl) and  $\sigma$  is the beam diameter (which will usually be larger than  $\sigma_o$ ). The irradiance can be treated as a probability density from which a distribution function can be formed

$$F(r) = 2\pi \int_0^r E(r)r dr \approx QS \left( \frac{\sigma^2}{\sigma_o^2} \right) \left\{ 1 - \exp \left[ -\frac{1}{2} \left( \frac{r^2}{\sigma^2} \right) \right] \right\} \quad (\text{D-6})$$

and

$$F(E) \approx QS \left( \frac{\sigma^2}{\sigma_o^2} \right) - 2\pi\sigma^2 E \quad (\text{D-7})$$

The function  $F(E)$  represents the total focal plane energy attributed to those pixels exceeding the irradiance threshold  $E$ .  $F(E)$  is seen to be a linear function of the irradiance, with a slope that is proportional to the beam radius  $\sigma$ . The x-axis intercept  $E_p \equiv QS/2\pi\sigma_o^2$  provides a means to measure of the peak irradiance, while the y-axis intercept gives the total energy included in the Gaussian core. Therefore, a linear fit to the upper portion of the irradiance distribution function will generate estimates of both the Strehl and the effective beam diameter. The general appearance of the  $F(E)$  curves for diffraction limited and aberrated beams are illustrated in Figure D-2. The

knee of the curve will generally occur well below the  $E_p/2$  point, so it is usually safe to include all data points above this value in the linear regression operation.

The preceding derivation provides a working definition of the Strehl ratio that includes the following analysis steps:

1. the formation of the corrected camera-data histogram  $h(I)$ ,
2. the creation of the camera distribution function  $F(I) = \sum_{i \geq I} i h(i)$ ,
3. the development of a linear fit to the upper half of the  $F(I)$  curve to obtain  $F'(I)$ , and
4. the determination of the x-axis intercept  $I_p$  for which  $F'(I_p) = 0$ .

The Strehl ratio is now defined to be

$$S = \frac{2\pi\sigma_o^2 I_p}{\sum_x \sum_y I(x,y)} \quad (D-8)$$

As usual, the determination of Strehl requires an accurate measurement of the total pulse energy and knowledge of the camera's magnification. Observe that

$$2\pi\sigma_o^2 = \frac{4}{\pi} \left( \frac{\lambda f}{Dd} \right)^2 = \frac{4}{\pi} \left( \frac{\Delta}{n} \right)^2, \quad (D-9)$$

where  $d$  is the pixel dimension,  $n$  is the number of phase sensor subapertures, and  $\Delta$  is a magnification factor given in units of beam motion (pixels) per wave of tilt per subaperture. Since the Strehl is proportional to  $\Delta^2$ , it is important that this magnification factor is remeasured following each change to the optical arrangement.

TOTAL ENERGY ABOVE IRRADIANCE THRESHOLD

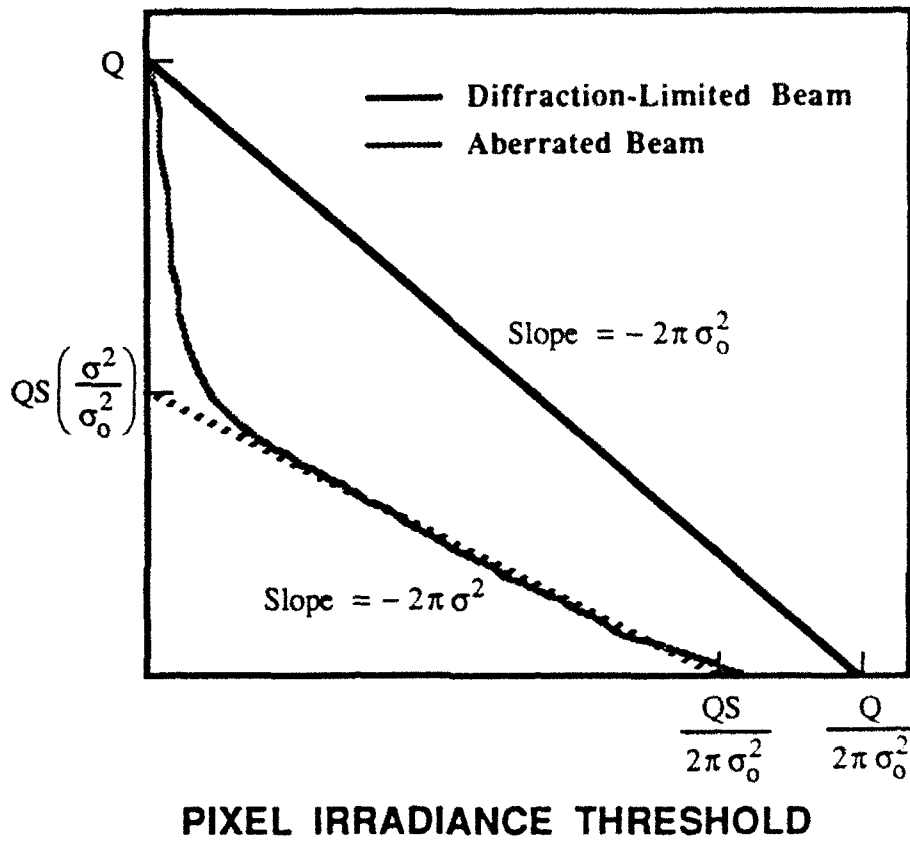


Figure D-2. Energy distribution functions for diffraction-limited and aberrated beams.

## APPENDIX E TURBULENCE MODEL PROFILES

The Hufnagel-Valley<sup>9,10</sup> and SLC-Day turbulence profiles are used in the performance studies described in this report as a means of indicating a range of potential results. The Hufnagel-Valley profile actually refers to a family of models that have the following general form

$$C_n^2(H) = 5.94 \times 10^{-53} (w/27)^2 H^{10} \exp(-H/1000) + 2.7 \times 10^{-16} \exp(-H/1500) + A \exp(-H/100) \quad (E-1)$$

where  $H$  is measured in meters above sea level and  $w$  is the rms wind speed averaged over the 5 to 20 km interval. The coherence diameter is affected principally by the low-altitude constant  $A$  (which is normally set to  $1.7 \times 10^{-14} \text{ m}^{-2/3}$ ), while the isoplanatic angle is most sensitive to  $w$ . The HV-21 model referenced to in this report uses a value of 21 m/sec for  $w$ ; since this results in a coherence diameter of 5 cm and an isoplanatic angle of 7  $\mu\text{rad}$ , this version of the model is also referred to as HV<sub>57</sub>.

The SLC-Day model is based on the day-time Miller-Zieske profile, which can be approximated by the set of power-law segments given below

$$\begin{aligned} C_n^2(H) &= 4.01 \times 10^{-13} H^{-1.05} & 19 \leq H \leq 230 \\ &= 1.3 \times 10^{-15} & 230 \leq H \leq 850 \\ &= 6.35 \times 10^{-7} H^{-2.97} & 850 \leq H \leq 7000 \\ &= 6.21 \times 10^{-16} H^{-0.62} & 7000 \leq H \leq 20000 \end{aligned} \quad (E-2)$$

This model is also referred to as SLCSAT Day.

REPORT DOCUMENTATION PAGE			Form Approved OMB No. 0704-0188	
<small>Public reporting burden for this collection of information is estimated to average 1 hour per response, including the time for reviewing instructions, searching existing data sources, gathering and maintaining the data needed, and completing and reviewing the collection of information. Send comments regarding this burden estimate or any other aspect of this collection of information, including suggestions for reducing the burden, to Washington Headquarters Services, Directorate for Information Operations and Reports, 1215 Jefferson Davis Highway, Suite 1204, Arlington, VA 22202-4302, and to the Office of Management and Budget, Paperwork Reduction Project (0704-0188), Washington, DC 20503.</small>				
1. AGENCY USE ONLY (Leave blank)	2. REPORT DATE 10 March 1993	3. REPORT TYPE AND DATES COVERED Project Report		
4. TITLE AND SUBTITLE SWAT System Performance Predictions			5. FUNDING NUMBERS  C — F19628-90-C-0002 PE — 63217C, 63221C PR — 33	
6. AUTHOR(S)  Ronald R. Parenti and Richard J. Sasiela				
7. PERFORMING ORGANIZATION NAME(S) AND ADDRESS(ES)  Lincoln Laboratory, MIT P.O. Box 73 Lexington, MA 02173-9108			8. PERFORMING ORGANIZATION REPORT NUMBER  PR-SWP-8, Revision 1	
9. SPONSORING/MONITORING AGENCY NAME(S) AND ADDRESS(ES)  AF Phillips Laboratory Firtland Air Force Base Albuquerque, NM 87177-6008			10. SPONSORING/MONITORING AGENCY REPORT NUMBER  ESC-TR-92-144	
11. SUPPLEMENTARY NOTES  None				
12a. DISTRIBUTION/AVAILABILITY STATEMENT  Approved for public release; distribution is unlimited.			12b. DISTRIBUTION CODE	
13. ABSTRACT (Maximum 200 words)  <p>In the next phase of Lincoln Laboratory's SWAT (Short-Wavelength Adaptive Techniques) program, the performance of a 241-actuator adaptive-optics system will be measured using a variety of synthetic-beacon geometries. As an aid in this experimental investigation, a detailed set of theoretical predictions has also been assembled. The computational tools that have been applied in this study include a numerical approach in which Monte-Carlo ray-trace simulations of accumulated phase error are developed and an analytical analysis of the expected system behavior.</p> <p>This report describes the basis of these two computational techniques and compares their estimates of overall system performance. Although their regions of applicability tend to be complementary rather than redundant, good agreement is usually obtained when both sets of results can be derived for the same engagement scenario.</p>				
14. SUBJECT TERMS adaptive optics                      phase conjugation atmospheric turbulence          synthetic beacon laser guide star			15. NUMBER OF PAGES 112	
			16. PRICE CODE	
17. SECURITY CLASSIFICATION OF REPORT Unclassified	18. SECURITY CLASSIFICATION OF THIS PAGE Unclassified	19. SECURITY CLASSIFICATION OF ABSTRACT Unclassified	20. LIMITATION OF ABSTRACT Same As Report	